Joint Retrieval of Wind- and Total Surface Current Vectors from TanDEM-X Bidirectional Along-Track Interferometric Data

Nina Caldarella

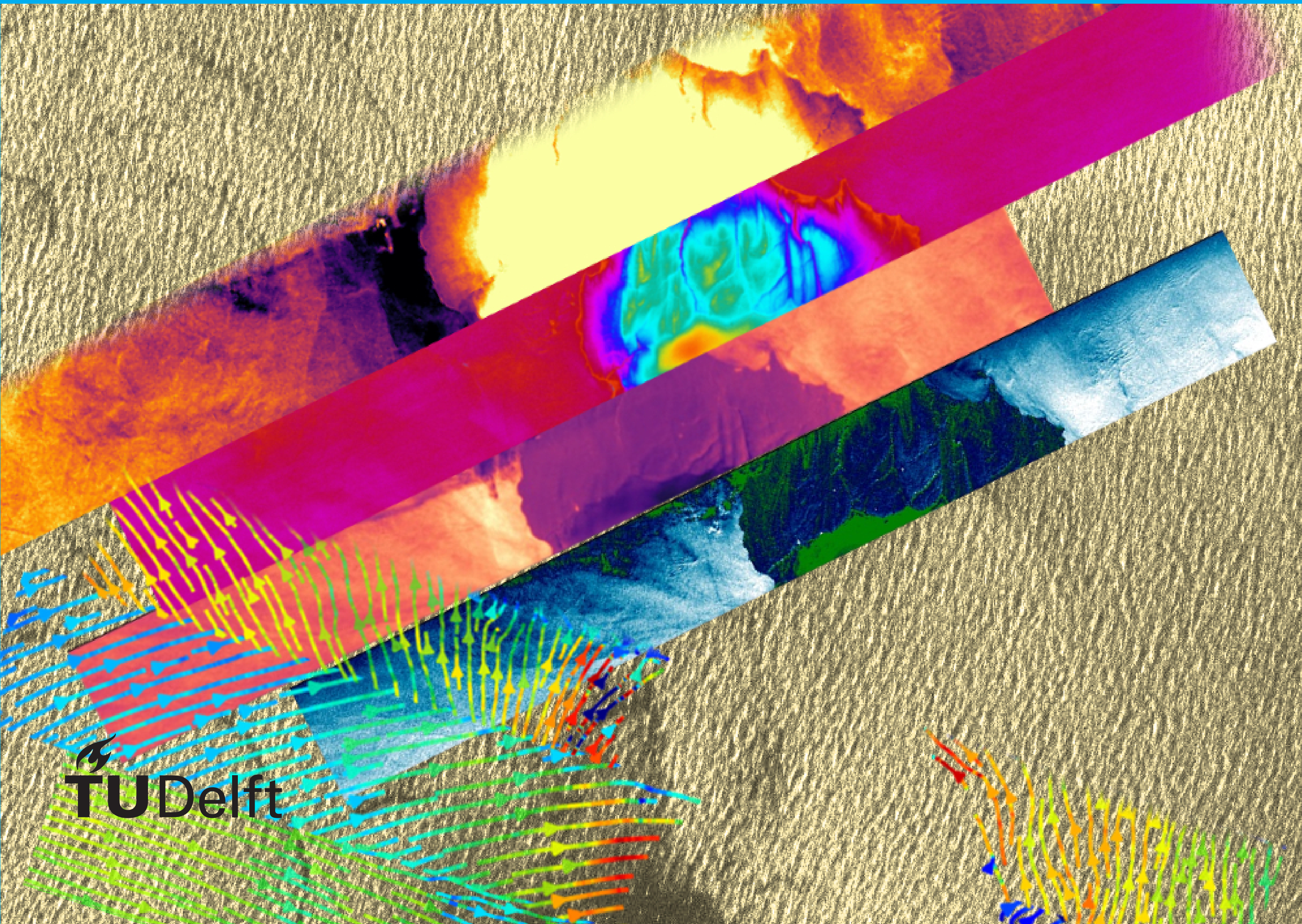

Joint Retrieval of Wind- and Total Surface Current Vectors from TanDEM-X Bidirectional Along-Track Interferometric Data

by

Nina Caldarella

to obtain the degree of Master of Science
at the Delft University of Technology,
to be defended publicly on Thursday the 20th of September, 2018 at 11:00.

Student number:	4134265	
Thesis committee:	Dr. ir. Paco Lopez-Dekker,	TU Delft, daily supervisor
	Prof. dr. ir. Ramon Hanssen,	TU Delft
	Dr. Caroline Katsman,	TU Delft
	Dr. ir. Mariantonietta Zonno	DLR

Abstract

Direct measurement of ocean surface velocity from space with a Synthetic Aperture Radar has shown to be a promising method to observe ocean surface currents[3]. In this thesis report a method for Total Surface Current Vector (TSCV) retrieval using an experimental Bidirectional (BiDi)[24] Along-Track Interferometric (ATI) acquisition mode with TanDEM-X[19] is presented. Errors of retrieval results from simulated data and from real data are studied to assess the quality of the proposed method. The available data consists of a StripMap acquisition at the coast of Tromsø and a data set acquired over Novaya Zemlya.

The measurement concept relies on the ATI phase, which provides an estimate of the first moment of the Doppler spectrum associated to total surface velocity[3]. Observing with two beams squinted as far as 13.2 degree apart in azimuth on ground, allows the Doppler velocity to be observed in line of sight of the beams. Projection to the ocean surface gives a velocity field. This Doppler velocity field consists of a Normalized Radar Cross Section (NRCS) weighted average of velocities of sea-state dependent biases such as short wind generated waves, long swell waves and underlying currents [22][3].

Assuming the surface velocity is dominated by wind generated waves and underlying currents, the method attempts to solve for TSCV simultaneously with the surface wind vector by coupling geophysical model functions (GMF) for returned Doppler Centroid (DC) and NRCS from an ocean surface shaped by wind. For NRCS the empirical GMF XMOD2 [26] for X-band radar is used, based on the same regression algorithm as the widely used CMOD5[12] in scatterometry. For DC a GMF based on statistics of the sea surface and the Kirchhoff Approximation developed by IFREMER is used [25][27].

A cost function of the wind vector is defined as the squared difference between NRCS observations and values of the GMF in both beams. The wind speed magnitude and wind direction for which this cost function is minimal provide an estimate to the local wind vector and evaluating the GMF for DC with the estimated wind vector results in a component of surface motion caused by wind generated waves. Wind wave induced surface velocities and TSCV can then be separated.

Retrieval from simulated data shows that the wind retrieval algorithm gives an ambiguous result for the wind direction. To constrain the solution ECMWF ERA-5 reanalysis wind data is added to the cost function as an additional term with a low weight factor. Error analyses on the propagation of data errors shows success of the method relies on calibration quality that itself depends on local conditions of the acquired data. Comparison of retrieved wind using different GMF's indicates there is a high uncertainty in the models. The average of retrieved wind vector field over the image is highly similar to the lower resolution ECMWF ERA-5 wind vector data. TSCV results appear good for data with small ATI phase errors, but are dependent on the accuracy of used GMF's.

Continuation of the work should focus on the use of other GMF's such as the Weighted Curvature Approximation or OceanSAR to reduce uncertainty. A correction to the radiometric calibration of the experimental SAR processor will provide unbiased NRCS data. The retrieval algorithm can be useful in future missions that use Doppler or ATI phase combined with NRCS at squinted angles for the observation of ocean surface currents.

Preface

Nina Caldarella
Amsterdam, June 2018

During the summer time of 2017 I was searching for a topic worthy to finish my studies in Delft with. Our rapidly changing Earth and technological advances offer an endless amount of interesting Master Thesis topics. It was a difficult step to dive into one small research topic only a dozen of people know about worldwide for almost a year. During the process I have learnt to appreciate the little contributions one makes in this way. I have grown to love my own work and research topic.

Without my daily supervisor dr. ir. Paco Lopez-Dekker I would not have found this direction, nor would I have understood the topic or recognized the quality of my own work. I would like to thank him for his frequent availability, clear explanation on complex matter and help in finding the right path.

Three months of the time I spent on this thesis I spent in DLR, Oberpfaffenhofen, Munich area. I would like to thank dr. Mariantonietta for her great supervision. Last thanks go to dr. Marc Rodriguez-Cassola and dr. Pau Prats for their help with calibration of the data, their explanation and insight.

Contents

1

Introduction

As resolution of oceanographic models becomes smaller, the demand of data at such scales arises. Ocean parameters are challenging to measure for the ocean's inaccessibility, enormous size and rough conditions. Since the wide availability of remote sensing data, our understanding of large-scale ocean circulations has increased[4]. Mesoscale (~100km) geostrophic ocean currents are retrieved from radar altimetry and with scatterometry wind fields can be retrieved. However, a direct approach to measuring ocean surface currents is still unavailable. Current observation methods do not capture small-scale processes, such as filaments, small eddies and their interaction, that show to be responsible for as much vertical transport as large eddies[17]. Apart from this mixing within the ocean, there are the heat fluxes at the air-sea interface and vertical transfer of CO2, becoming a more important topic of study as the Earth warms and CO2 levels rise and requiring more observations. Also phenomenons such as transport of nutrients for phytoplankton may be better understood with more knowledge of the ocean's physics at small scale[23]. Downscaling of our geophysical models includes more smaller scaled processes asking for more parameters to resolve. Synthetic aperture radar offers the possibility to measure parameters associated with surface currents at high resolution[2].

Since its first introduction by Goldstein [9], Along-Track Interferometric Synthetic Aperture Radar (ATI SAR) has been a promising technique to measure ocean surface phenomena such as wave fields [21] and current velocity [9]. These measurements are only taken with a single side looking SAR beam, resolving only a radial component of the Doppler velocity. The idea of a dual beam system, that is capable of measuring the Doppler velocity in radial and azimuthal direction is proposed for airborne systems [29]. [32] elaborates on the idea and [37] gives the first demonstration of the airborne dual beam along track synthetic aperture interferometer. This method has first been applied to spaceborne SAR data and demonstrated in [22], of which this work is a continuation. The additional value of continuous measurements of the ocean (surface) currents at high resolution and high accuracy has many advantages over the airborne dual beam ATI SAR, as the longterm continuous monitoring of currents affected by the changing climate or practical advantages.

ATI data sets of TanDEM-X with a dual beam configuration have come available and preliminary processing was done to show the capability of the method [22]. Location of these acquired experimental data sets are at Arctic latitudes, which is a consequence of a restriction on the baselines. The configuration comprises two satellites following each other in orbit, TerraSAR-X (TSX) and TanDEM-X (TDX), as shown in figure 1.1. Of each satellite the two beams are squinted as far as possible from the direction perpendicular to orbit direction. The dual beam configuration of two satellites in the same track allows us to image the ocean surface quickly after another with a fore- and aft beam. The time between acquisitions is sufficiently small for the ocean surface images not to decorrelate. From the interferogram of the two images the ATI phase difference relates changes on the ground, that can be interpreted as Doppler frequencies. A radial component of surface velocity is obtained from this interpretation. From the two squinted Doppler velocities in line of sight, an along-track and across-track component of surface motion can be derived. The across-track component of velocity gives a very accurate estimate of mean surface motion, whereas the along-track component is a scaled version of the across-track component and gives therefore still a reasonable estimate.

This surface velocity vector contains contributions of the whole sea-state, including wind induced waves, current and swell (figure 1.1), the so called geophysical biases. Wind waves that roughen the surface of the

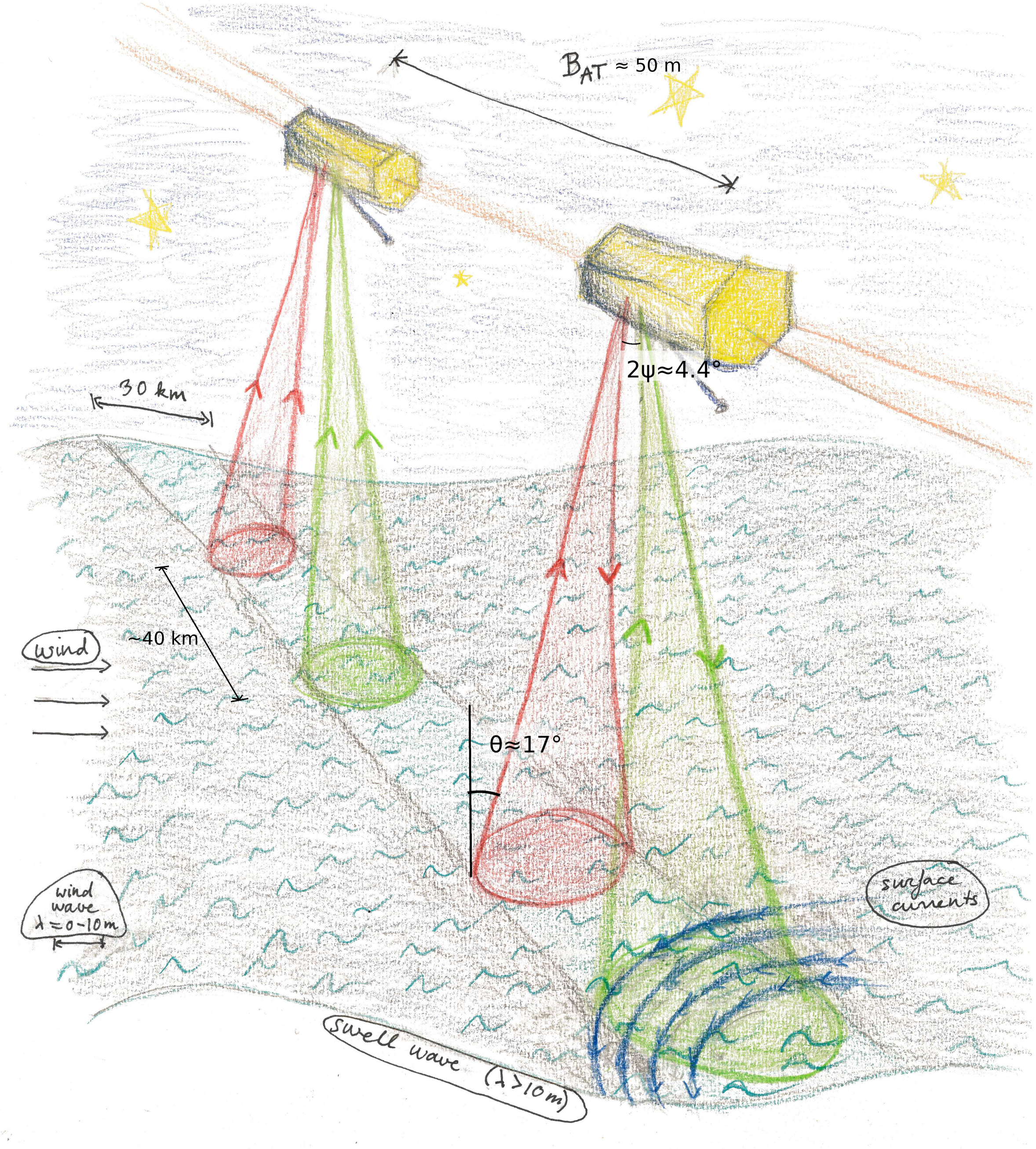

Figure 1.1: Artistic representation of the topic. TanDEM-X and TerraSAR-X in orbit with minimal baselines (B_{AT}). Antenna squinted in two direction for both satellites. TanDEM-X is in bistatic mode, implying that the first satellite in orbit (master) transmits radar waves and receives them and the second satellite only receives. Acquisition mode is StripMap (30 km wide strip in range). The ocean is depicted as a surface with the most important processes acting on it. Small surface waves are wind generated, long waves are associated with swell and currents are seen as displacement of the surface with the wind waves on top of it. Note that B_{AT} is actually much shorter(~50 m) than the separation distance between the beams on the ocean surface (~40 km), which is slightly misleading in this representation.

ocean can be observed in an amplitude image, i.e. the NRCS is correlated to the wave geophysical bias. We can then interpret the Doppler velocity as a NRCS weighted average of the radial surface velocity[3]. The bidirectional Doppler velocity and bidirectional NRCS provide us with four observables. This is sufficient to solve for the wind vector and for a vector corresponding with other ocean surface processes called the Total Surface Current Vector (TSCV). This leads to the main research question:

How do we separate the Total Surface Current Velocity from wave geophysical bias in the dual-beam TanDEM-

X Along-Track Interferometric data?

Waves that are a function of sea-state parameters are captured in the ocean surface wave spectrum [6]. With the sea surface wave spectrum one can estimate the wave bias using geophysical model functions for the radar return from the surface. So far many models for wind retrieval from NRCS have been proposed and demonstrated [21] [20] [34] [26], but not as many for total surface current retrieval [31] [3].

In order to make a meaningful estimate of the wind vector and TSCV, calibration of the data is necessary. Radiometric calibration needs to be implemented to the experimental SAR processor to obtain an accurate NRCS measurement for wind retrieval. Comparing data sets that are processed with the operational processor with those processed with the experimental processor can give an idea of the quality of calibration. The Bidirectional (BiDi) ATI phase has offsets that are mostly a result of errors in coregistration. This phase offset may be corrected for by assuming the phase on land as zero, which is true for the short ATI baselines of this data and when the topography is correctly flattened.

To separate TSCV from wave geophysical bias a joint retrieval algorithm that exploits NRCS and ATI Doppler will be developed. As first the wind vector needs to be estimated, which can be done in fashion similar to scatterometry. The retrieval algorithm uses Geophysical Model Functions for the NRCS and Doppler Centroid as a function of the wind vector. There are different types of models available, as composite Bragg models[20], asymptotic electromagnetic methods [25] and empirical models [26]. After calibration of the observations and when the wind vector is retrieved, a TSCV may be computed by evaluating the GMF for the Doppler Centroid with the wind vector and subtracting the wave geophysical bias from ATI velocity.

Once an estimation for the wind vector and TSCV is obtained, an analysis of the quality of this method needs to be performed. This formulates to the second research question:

How well do we separate the Total Surface Current Velocity from wave geophysical bias in the dual-beam TanDEM-X Along-Track Interferometric data?

In the evaluation of the retrieval process three sources of error are considered:

1. GMF errors
2. data errors
3. retrieval errors

An analysis of the retrieval results is conducted in the following way. A qualitative understanding of GMF errors may be acquired by means of comparison of retrieval results using different models. Data errors are minimized by calibration. Understanding the source of the errors gives us an idea of the accuracy. Retrieval errors are the propagation of model errors, data errors and ambiguities to the wind vector. Retrieval errors may be better understood by simulation. As the angular separation between the beams is significantly smaller than for usual scatterometry, the observations of NRCS may not be sufficiently independent to estimate all of the unknowns. It will then be needed to constrain the solution. With atmospheric model data we can qualitatively assess the estimation results.

In this chapter the need of direct surface current observations from space has been discussed. Along-Track Interferometry has the capability to measure the Doppler velocity of the ocean surface. However, this surface velocity contains a geophysical bias from the wind waves. Rest of this thesis is dedicated to the separation of the wave geophysical bias from the so-called Total Surface Current Velocity. In chapter 2 theoretical background to understand the observation system and geophysical models that are used in the methodology is given. Chapter 3 introduces the data sets used in this study. The proposed methodology is presented in chapter 4, the methodology is tested on simulations (5) and finally results of wind field and TSCV are demonstrated (6), concluded and discussed (7).

2

Theory

This chapter provides a theoretical background on observation of the ocean with Along-Track Interferometry. Understanding is required of the SAR imaging system, interferometry and of the ocean's surface itself. First two sections are technical background on the imaging system.

Last two sections are concerned with physical oceanography. Processes that can be observed in the SAR image are discussed in section 2.3, subdivided in currents and waves. Section 2.4.1 introduces the topic of electromagnetics applied to the ocean surface, that provides us with the models that will be used in the methodology.

2.1. Synthetic Aperture Radar

This subsection is aimed at readers without a SAR background. A brief introduction to the SAR principle is given, some important SAR parameters are defined and the concept of interferometry is discussed. In 2.2 more specific processing of Bidirectional SAR is explained.

2.1.1. SAR principle

The Synthetic Aperture Radar can produce high resolution images of the ocean's and Earth's surface. It comprises of a pulse transmitter, an antenna and a phase-coherent receiver. The SAR illuminates the Earth's surface from space or from an airplane, the beam is oriented in a side-look direction. Figure 2.1 depicts the basic SAR imaging geometry. A patch of images of the illuminated area, parallel to the orbit/flight path is constructed. It is an active sensor, implying that pulses are sent by the antenna and then received from the Earth's surface at the *pulse repetition frequency (PRF)*. The SAR is not limited by the integration time, whereas the Real Aperture Radar is limited by the time of illumination of the surface. The resolution is then limited by the antenna footprint size $R\lambda/L$, where R is the distance in slant range to the ground and L the antenna size both unit length. With the phase-coherent receiver of SAR a Doppler frequency spectrum can be measured. The high frequency components contain high resolution informatiion. Accordingly the image is sharpened in azimuth and the resolution is reduced to approximately half the antenna width L/2. The independence in resolution of range allows for imaging from satellites and airplanes at high resolution.

A high range resolution is acquired in the following way. The range resolution is determined by the duration of the transmitted pulse. Two targets can be recognized if they are separated $\frac{1}{2}c\tau$ in range direction, where τ is the pulse duration time (1/PRF), c the speed of light, the factor 1/2 due to the two-way travel of the signal. By modulating the frequency of the transmitted pulse, the pulse duration is shortened, while transmitting the same amount of power and reducing the resolution (chirping). The received echo's from the pulses are detected, separated and arranged side by side in a 2D raw data matrix with the coordinates and two-way-travel time of the pulses, to relate the images to the satellite position. Coordinates of the azimuth focused product are used for *coregistration* of two SAR images in interferometry (section 2.2.2). The continuous SAR imaging with a swath as depicted in figure 2.1 is called StripMap mode. the TanDEM-X Bidirectional ATI images are acquired in StripMap mode.

Layover is a SAR effect that occurs when there is high topography, buildings or other high rise structures

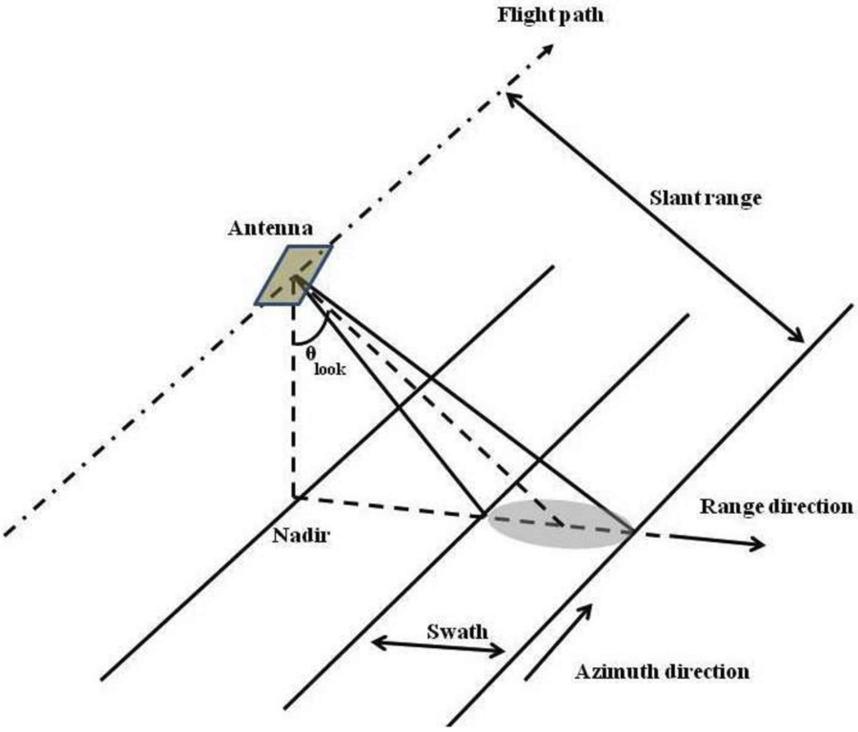

Figure 2.1: This figure shows the geometry of a basic SAR. The azimuth direction is taken positive in orbit direction. The range direction is positive in look direction of the radar. The slant range is the ground range divided by the cosine of the lookangle. The swath width is the length of the radar beam on ground in range direction. Ascending orbits go from southpole to north pole and Descending orbits vice versa. (credits: NASA)

in the image. It is important to detect this effect in the land areas of our images, as these distortions will influence ATI phase calibration. SAR uses measurements in range to locate the scatterer. When a mountain is imaged from the side, the range distance from the radar to the valley and the range distance from the radar to the mountain is the same. This causes the mountain to be imaged at the location of the valley. Behind the mountain there is an area of which no signal returns, this causes a shadow in the radar image. These effects are seen later in the images of a data set over Tromsø in section 6.1

2.1.2. Normalized Radar Cross Section σ_0

NRCS is a key SAR parameter for the study of winds. In case of an ocean a high intensity often corresponds with high wind speed, due to the rougher surface formed by the wind. NRCS is a measure for the intensity of illumination of a surface. Radar Cross section is defined as the equivalent area of perfectly reflecting surface that isotropically scatters the same flux back to the antenna. The NRCS is the Radar Cross Section (σ) devided by the area of the resolution cell of the imaging SAR. It is often expressed in decibels and the unit is m^2/m^2. In equation form the NRCS is written as

$$\sigma_0 = 10log_0(\sigma/A). \tag{2.1}$$

The *Noise Equivalent Sigma Zero (NESZ)* is the NRCS for which the Signal to Noise Ratio (SNR) is equal to zero decibels. It reflects the amount of noise contained in the signal:

$$SNR = NRCS - NESZ. \tag{2.2}$$

2.1.3. Doppler Centroid

The Doppler Centroid parameter relates to the velocity of the scatterer, in our case the ocean surface. It is another method for measuring sea surface motion exploiting the Doppler Centroid Anomaly. It's worth mentioning this method, since in this thesis the ATI phase is interpreted as a Doppler velocity. The antenna beam width causes the scatterer to be imaged within the beam for a number of pulses. During these pulses the velocity with respect to the scatterer changes, causing a Doppler-like effect. The difference between measured Doppler frequency and geometric Doppler frequency provides the Doppler Centroid Anomaly. The geometric Doppler centroid for an approaching target is described with the following expression ([10]):

$$f_D = \frac{2v_{orb}}{\lambda} sin(\phi_s) sin(\theta), \tag{2.3}$$

where v_{orb} is the platform velocity in orbit direction, ϕ_s the scatterer angle w.r.t. to nominal radar look, positive in flight direction and θ the radar incidence angle.

2.1.4. Interferometry

Synthetic Aperture Radar Interferometry can be done in many geometries and configurations. Across-track interferometry is an often used method for deformation monitoring. In this thesis we are looking at ATI, which is a method often used for the observation of oceans for its small baselines.

Interferometry subtracts the phase of two coregistered SAR images, with range R_1 and R_2 to the scattering object and a baseline B, which is the distance between the satellites. This is done by means of a complex multiplication of two images. The phase angle of this product is called the *interferogram*.

Coherence γ is the complex correlation coefficient of two SAR images. It describes how much the alike the two SAR images are. As coherence combines the properties of the amplitude image with the phase image of ATI, this data may be valuable for the interpretation of geophysical processes on the ocean. However, in this study coherence is merely used as a weighting factor for calibration. Coherence exists from the product of some dominant contributions [2]

$$\gamma = \gamma_{SNR} \gamma_H \gamma_T$$

where γ_{SNR} is the influence of finite signal to noise ratio, γ_H the decorrelation caused by the fact that two SAR signals have passed different filters and γ_T the temporal scene coherence, which relates to the changes in the scene between the two images.

Low SNR leads to a low coherence. This property of coherence is exploited in the phase calibration procedure of BiDi. Temporal scene coherence relates to movements of the ocean surface during period between the two satellite passes.

Interferometric phase is very sensitive to the baseline. The *height sensitivity* k_z can be expressed as [2]

$$k_z = \frac{4\pi}{\lambda} \frac{B_\perp}{R_s sin(\theta)}, \tag{2.4}$$

where k_z is the height sensitivity (fringe frequency in height in cycles/meter), λ the radar wavelength in meters, R_s the slant range in meters, $B_\perp$ the perpendicular baseline in meters and θ the angle of incidence in radians.

Height of ambiguity is defined as the height change in meters over a 2π cycle, and is therefore inversely proportional to the height sensitivity. Height sensitivity is minimal in our case, due to the small baselines. With the low height sensitivity we are able to neglegt wave topography. However for purposes of phase calibration topography on land is still considered.

2.2. TanDEM-X Bidirectional Along-Track Interferometry

This subsection gives information on the more specific processing of Bidirectional SAR data. 2.2.2 continues with a detailed explanation on Bidirectional Along-Track Interferometry and equations that are later used for post-processing of the ATI phase are presented.

2.2.1. Bidirectional imaging mode

In subsection 2.1.1 and figure 2.1 an explanation on processing of nominal SAR images have been given. However, in this thesis we are concerned with a Bidirectional imaging mode. Understanding the bidirectional imaging process is important to understand error sources.

Bidirectional imaging mode with the TerraSAR-X and TanDEM-X synthetic aperture radar simultaneously images in two directions with one antenna. In this way two beams are formed, squinted apart as far as possible. In figure 1.1 the squinted angles are pictured.

The bidirectional imaging concept is based on an azimuth pattern with two major lobes pointing into different directions. The resulting Doppler azimuth spectrum has a large bandwidth. Figure 2.2 shows the Doppler azimuth spectrum for the beams separatedly as simulated by Mittermayer et al.. By choosing a good value of high PRF approximately between 5700 and 5900 Hz the two components can be separated in the Doppler frequency domain.

Each beam has a non-zero Doppler Centroid, as a consequence errors in coregistration will lead to larger errors in the data than for the nominal radar look. The NESZ of bidirectional imaging mode is affected by the splitting of the beams, as intensity of the antenna pattern of each squinted beam is approximately half the intensity of the antenna pattern for a single beam.

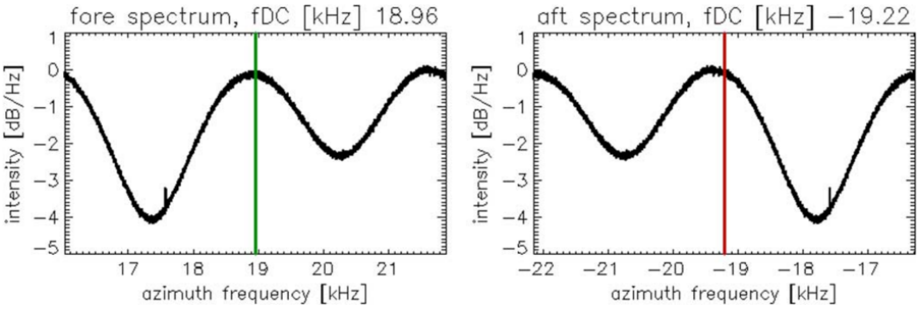

Figure 2.2: This figure shows the BiDi Doppler spectrum as simulated by Mittermayer [24]. On the left the Doppler spectrum for the fore beam and on the right for the aft beam. The observed Doppler spectrum does not have a separated fore- and aft spectrum complicating focusing and requiring a high PRF. Splitting of the antenna beam into two causes the intensity of each antenna pattern to be half the intensity of the antenna pattern for a single beam. The Doppler Centroid of each beam is non-zero, as a result of the squinted look.

2.2.2. Bidirectional Along-Track Interferometry

In section2.1 the interferometry concept has been briefly described and the reader is provided with an explanation on the coherence and height sensitivity. In this section interferometry is specified to our Bidirectional Along-Track Interferometric data. We will be looking at short baselines, that allow us to observe a horizontal motion of the sea surface.

For Along Track Interferometry, upper limit of the baseline is determined by the decorrelation time of images[1]. For too large baselines the temporal correlation would be too large and for too short baselines the impact of noise would be too dominant [38]. In the mission design by Wollstadt et al. the optimal baseline is found to lie between 1000-2000λ. This baseline contributes to a coherent image and therefore low phase noise.

With very small cross-track baselines, minimizing the topographic signal, the interferometric phase can be interpreted as a motion of the sea surface. The amount of measured phase cycles corresponds to a distance over the period of the interferometric time lag

$$\tau = \frac{B_{AT}}{2 \cdot v_{orb}}, \tag{2.5}$$

where B_{AT} is the along-track baseline and v_{orb} is the platform velocity in m/s. Interferometric phase can then be related to a velocity in Line of Sight of the beamdraft

$$\phi_{ATI} = -2\pi \frac{B_{AT}}{\lambda} \frac{v_{LoS}}{v_{orb}}, \tag{2.6}$$

where ϕ_{ATI} is the interferometric phase of the ATI images in cycles, λ is the radar wavelength ($\tilde{0}$.0032 meters for X-band radar), v_{LoS} is the phase velocity in radar Line of Sight in m/s. For each squinted beam an average of the sea surface motion (v_{LoS}) is projected on the line of sight of the sensor. The phase velocity provides an estimate of the first moment of the Doppler spectrum. In our data product, the baseline itself is not directly given, but the interferometric time lag may be used to compute v_{LoS}. With equation 2.6 and 2.5 we can compute the velocity in beam line of sight

$$v_{LoS} = \frac{\phi_{ATI}}{2\pi} \frac{\lambda}{\tau}. \tag{2.7}$$

By using a dual beam configuration, with beams in different directions an along-track and a cross-track component of the Doppler velocity measured in beam Line of Sight can be found using the following geometric relations:

$$v_{at} = \frac{v_{fore} - v_{aft}}{2sin(\psi_s)}, \tag{2.8}$$

$$v_{xt} = \frac{v_{fore} + v_{aft}}{2cos(\psi_s)}, \tag{2.9}$$

where v_{at} and v_{xt} are the components of Doppler velocity in along-track and across-track direction respectively. ψ_s is the radar squint angle. This is basically a scaling of the line of sight velocities for the along-track component, and an average of the line of sight velocities for the across-track component. A scaling of the along-track velocity with $2sin(\psi)$ leads to a scaling of the errors with $sin(\psi)$

$$\epsilon_{at} = \frac{\epsilon_{fore} + \epsilon_{aft}}{2sin(\psi)} = \frac{\epsilon_v}{sin(\psi)}, \tag{2.10}$$

whereas the across-track velocity errors have a scaling with $cos(\psi)$

$$\epsilon_{xt} = \frac{\epsilon_{fore} + \epsilon_{aft}}{2cos(\psi)} = \frac{\epsilon_v}{cos(\psi)}. \tag{2.11}$$

For a squint angle as small as 4.4° this leads to a 13 times larger uncertainty on the estimated along-track component than on the across-track component.

2.3. Physical processes at the ocean surface

In this study we are concerned with a combination of topics. In previous sections of this chapter the topic of SAR processing and interferometry has been adressed, but to understand our data it is important to have an idea of the physical processes playing a role on the ocean surface.

Physical processes of the ocean are subdivided in two categories: currents and waves. Currents are the process we aim to observe. Wind waves dominate the SAR image and are therefore considered the most important disturbance to the observations. The reader is provided with a basic understanding of current components that may be observed and the wind wave spectrum.

2.3.1. Ocean currents

Since we are interested in observing the TSCV, the expectation of ocean currents needs to be considered. The currents are subdivided in large-scale currents and sub meso-scale currents. In the past ocean currents have been observed mostly at large scales. At these large scales we have acquired much understanding on processes acting on the ocean surface. Sub-mesoscale processes lack observations and understanding. This is the scale this research aims at. In this section the reader is provided with a basic understanding of the ocean currents at both scales and its implications to the results from our data.

Large-scale processes

The strongest current playing a role in the regions considered in this thesis is the North Atlantic Current. This current is part of the Atlantic Meridional Overturning Circulation, a system of currents that circulate between the Gulf of Mexico and the Arctic, responsible for transport of large amounts of heat. Warm waters from the Gulf of Mexico are transported to the latitudes of Newfoundland along the east coast of North America by winds as the Gulf Stream. When the current arrives at the Mid-Atlantic ridge, 60% turns to the north to form the North Atlantic Current and rest goes to the south east[18]. The North Atlantic Current splits into several branches, to the Denmark Strait, Fram Strait and the branch towards Norway.

The North Atlantic Current extends to the Norwegian current along the coast of Norway, where it mixes with outflow of surface waters. This current has velocities varying between 15 and 40 cm/s [33]. In figure 2.3 the Norwegian coastal current is partly depicted along the coast of northern Norway. At Spitzbergen the Norwegian current splits into a stream to the Greenland sea and Barents sea. In the Barents sea the warm Norwegian current further cools, mixes with water from the Arctic sea and weakens.

For the data take in Tromsø (small black rectangle in figure 2.3) the strong North Atlantic current expectedly lies outside of the measured area. For the data take in Novaya Zemlya (large black rectangle in figure 2.3) a weaker northward current is seen.

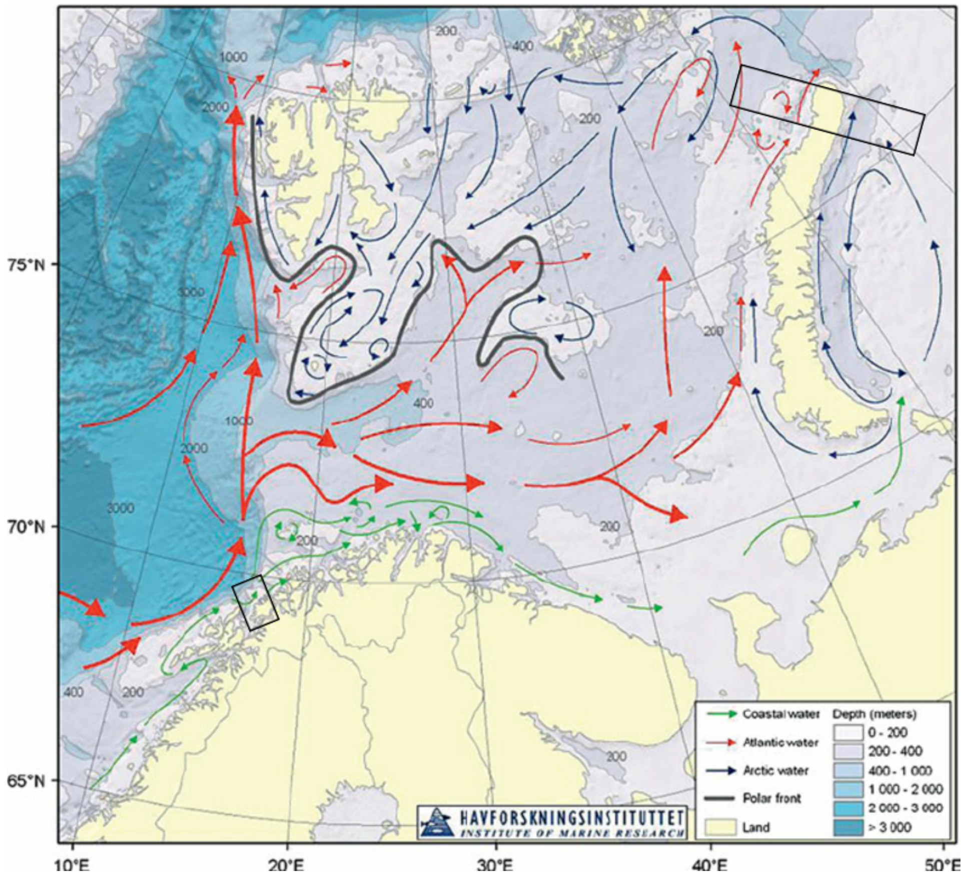

Figure 2.3: Map of ocean currents at the Barents sea (source:[15]). Note that currents are predominantly Northwards due to the Northern Atlantic Current. The black rectangles indicate the acquisition areas of data sets used in this study.

(Sub)Mesoscale processes

At the scales of a SAR image, ocean circulation is dominated by turbulent eddies, fronts and filaments (submesoscale <10 km). Smaller mesoscale eddies are assosciated with horizontal transport in the upper ocean and are therefore of relevance for this study. Submesoscale processes in the form of filaments and fronts are most effective in vertical mixing [7].

Sub meso-scale eddies in the area's of Tromsø and Novaya Zemlya are currently not well defined by observations or model simulations. Currents in the Barents sea and the cold waters of the Kara sea [11] are weak and therefore it is less likely to see many sub meso-scale eddies in the data set of Novaya Zemlya. In Tromsø the Norwegian Current has a higher temperature and is faster increasing the chance on the occurence of eddies in the TSCV results. Also more topographic and bathymetric features give rise to a higher chance on small eddies.

Tidal currents

The Ocean's tides periodically move large masses of water. This can lead to current velocities at the surface up to 5 m/s in extreme cases, specifically in coastal regions. Therefore special attention should be paid for our case to the possible presence of a tidal component in the measured Doppler velocity.

Ocean tides arise from variations in the gravity field due to motion of the Moon and Sun relative to the Earth. If one assumes the Earth's surface fully covered with water, the problem is simple. There are two mechanisms that then shape the ocean:

1. The Moon and Earth rotate about the center of mass of both planets. A centripital acceleration on the Earth drives the water away from the center of mass and to the side away from the Moon.

2. Mutual gravitational attraction between the two bodies causes water to be attracted towards the moon.

The rotation of the planets determines the periodicity of the tides. Apart from the rotation of the Earth and Moon about the center of mass, the Earth also rotates about its axis. Neither is the distance between Moon and Earth constant, but a periodically varying distance. These movemements make up for more tidal components. In the same way as the Moon, the Sun also excerts forces on the Earth. Taking the Sun into account, one obtains an ocean tide with lunar cycles and solar cycles. For both Sun and Moon there are three distinct groups of tidal frequencies: twice-daily, daily and longer periods. These form a set of 'principal tidal constituents' given in table 2.1, with the amplitude and period calculated for an Earth fully covered with water.

Naturally the Earth has varying bathymetry and land. These factors influence the tides. Amplitude and phase of tides at the coast can be calculated using measurements from tide gauges over a long period of time. An accuracy of the amplitude of 10^{-3} is acquired using 39 tidal constituents[35].

Table 2.1: Principal tidal constituents [35]

Tidal species	Name	Equilibrium amplitude(m)	Period (hr)
Semidiurnal			
Principal lunar	M_2	0.242334	12.4206
Principal solar	S_2	0.112841	12.0000
Lunar elliptic	N_2	0.030704	11.9673
Diurnal			
Lunisolar	K_1	0.141565	23.9344
Principal lunar	O_1	0.100514	25.8194
Principal solar	P_1	0.046843	24.0659
Elliptic lunar	Q_1	0.01956	26.8684
Long period			
Fortnighty	Mf	0.041742	327.85
Monthly	Mm	0.022026	661.31
Semiannual	Ssa	0.019446	4383.05

The largest constituent in table 2.1 is the M_2 constituent. This constituent and some other constituents were modeled [8] for the Barents sea and the map of amplitude and phase of the M_2 tide at the Barents sea is given in figure 2.4. In figure 2.4 amplitude of tides in Norway is significantly higher than in Novaya Zemlya. This is the case not only for the M_2 tide, but also for all other modeled constituents. Therefore, the tidal currents are expected to be higher in Norway than in Novaya Zemlya.

Expectation of current patterns in the data

How will the current patterns in the area affect the results of the TSCV retrieved from the Doppler field? What surface current will dominate the results? To these questions there is no definite answer, but they can be answered relatively and qualitatively.

In Tromsø there is a strong northward flow coming from the Norwegian current, but it will not reach into most of the observed area. Between the fjords currents are weak. The topographical features may cause more turbulent eddies. Tidal currents are expected to be dominant due to the high tidal amplitudes in this location.

Novaya Zemlya has weak warm nortward current in the Barents sea, that is the extension of the same Norwegian current. In the Kara sea the water moves slower. It is therefore expected that not many eddies are seen in the images. Tidal amplitudes are low in the area and tidal currents are expected to be small.

2.3.2. Ocean waves

In the introduction in figure 1.1 two types of waves have been illustrated with their difference in wavelength and the short waves that are superposed on longer waves. Short waves have a different origin than long waves. The distinction between types of waves and their origin is important to understand their interaction with radar waves.

The sea can be pictured as an endless succession of moving irregular humps. The ocean surface is rarely calm and flat, even then there is motion of swell waves that have arisen from winds further away. Storms can produce a sea with fast moving chaotic waves. While tsunami waves are known to travel very far at even larger velocities of 150 m/s [16]. Water particle speed in a wave relates to the propagation velocity of the wave

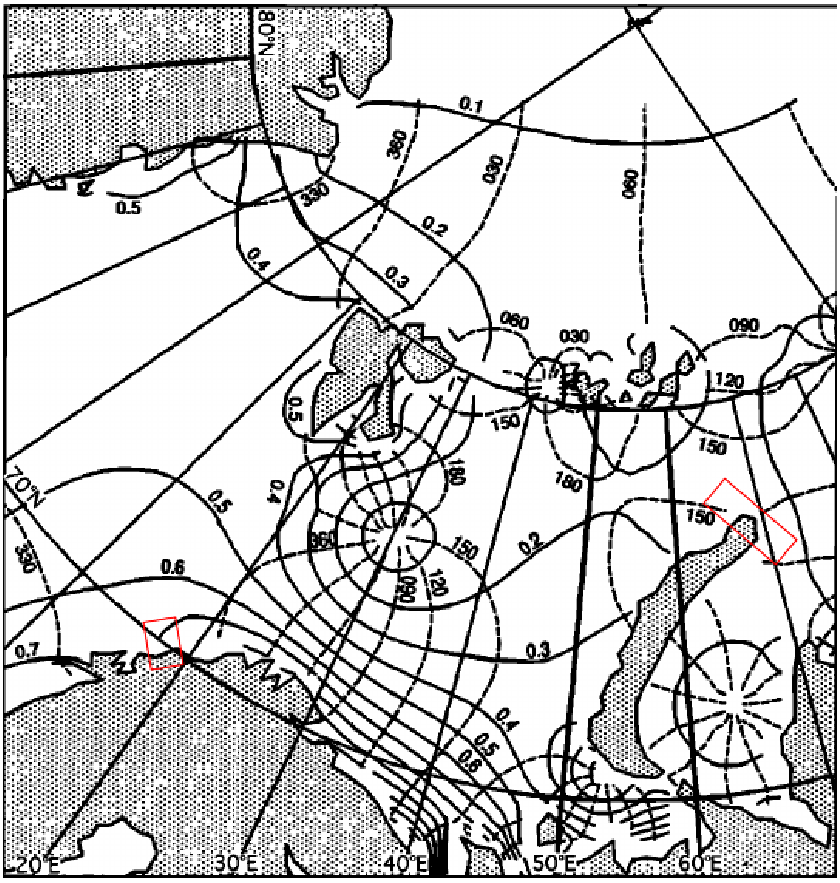

Figure 2.4: Modeled M_2 tidal chart. Equidistance 0.1 m for amplitude and 30° for phase[8]. Red rectangles indicate the areas of data takes. It can be seen that the amplitude of tides in Norway is significantly higher than in Novaya Zemlya. This is the case not only for the M_2 tide, but also for all other modeled constituents.

as $c_p/c_w = \pi H/L$. Wave heights H are smaller than wavelengths L and therefore particle speed is lower than propagation speed. Still one can understand that the orbital velocity introduces a very significant component to the Doppler field we measure.

Wind waves are often refered to as gravity waves. Waves are the result of forces acting on the ocean and balancing forces. When wind blows on a patch of ocean and the stress generates a hump, gravity will force the hump down again. Very large waves as tidal waves and tsunamis are resisted by the coriolis force and very small waves by surface tension and capillary forces. Kinsman classified waves according to their resisting force, which is depicted in figure 2.5 in a fashion similar to the well known spectral bands of light.

Fetch is the length of the patch of ocean over which the wind blows to generate a wave. Wind waves become longer and higher with increasing fetch and wind strength. If the wind blows for a long enough period and long enough fetch and then stops, a *swell wave* is born, that can travel very far without dissipating much energy. Particles in swell waves display a rotational motion decreasing with depth. The average motion of a fluid particle in a swell wave is called stokes drift. Stokes drift may also be observed in the ATI phase.

Wave breaking occurs when energy of the wave becomes too high. The excessive energy of the wave dissipates to a turbulent motion causing white caps on the sea surface. The tendency is that high wind velocity leads to more breaking and consequently white caps. Phillips derived an expression for the whitecap coverage of breaking waves based on statistical properties of gravity waves spectrum in the equilibrium range [28]. However, the models used in this study do not include this type of waves. Therefore, one should pay attention when looking at radar images of seas with high wind speeds.

Ocean wave spectrum

At a point in time and space these waves can all individually be described by a sinusoidal function

$$\eta(\mathbf{x}, t) = B(\kappa, \sigma)\cos(\kappa - \sigma t) \tag{2.12}$$

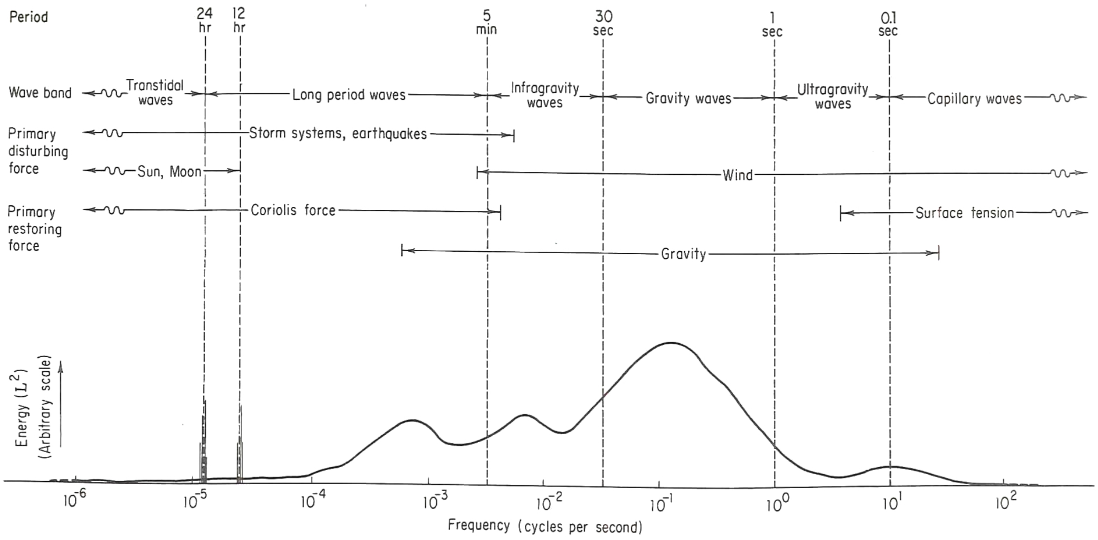

Figure 2.5: Schematic representation of the energy contained in surface waves of the oceans. The curve is in fact a guess by Kinsman of an average power spectrum of sea surface waves. Waves are the result of a disturbing force on the ocean and a resisting force. Wind induces small waves and primary gravity resists the wind force. Tides and earthquakes induce very large waves that are resisted by coriolis forces. Wind induced waves are the reason for by far most particle motion in the radar images. Kinsman distinguishes *sea* - and *swell waves*, both are wind induced, but sea waves are still being worked on by the wind. Swell waves are a bias in the the wind vector retrieval from radar data. A rough rule of thumb separates sea waves from swell waves at a wave period of 10 s.

where η is the sea surface height, $\mathbf{x}$ is a two-dimensional position vector, κ is the two-dimensional wavenumber, σ is the frequency and $B(\kappa,\sigma)$ is the amplitude. The sea surface including all individual waves is then represented by the sum of a finite number of Fourier components in three dimensions. In complex notation and integral form this gives

$$\eta(\mathbf{x},t)=\int_{\kappa}\int_{\sigma}B_3(\kappa,\sigma)\epsilon^{i(\kappa\cdot\mathbf{x}-\sigma t)}d\kappa d\sigma, \tag{2.13}$$

where $B_3(\kappa,\sigma)$ is the three-dimensional generalized Fourier transform. Since η is a real function, taking the complex conjungate of B_3 will make no difference and since the integration is over all wavenumber and frequency space a shift of $\mathbf{r}$ in $\mathbf{x}$ and τ in t neither will.

$$\eta(\mathbf{x},t)=\int_{\kappa"}\int_{\sigma"}B_3*(\kappa",\sigma")\epsilon^{i(\kappa"\cdot(\mathbf{x}+\mathbf{r})-\sigma(t+\tau))}d\kappa"d\sigma". \tag{2.14}$$

Multiplication and taking the mean of 2.13 and 2.14 gives the covariance function of the sea surface

$$H(\mathbf{x},\mathbf{r};t,\tau)=\overline{\eta(\mathbf{x},t)\eta(\mathbf{x}+\mathbf{r},t+\tau)}=$$

$$\int_{\kappa"}\int_{\kappa}\int_{\sigma"}\int_{\sigma}\overline{B_3B_3^*}\epsilon^{i(\kappa"\cdot(\mathbf{x}+\mathbf{r})-\sigma(t+\tau))}$$

$$\epsilon^{i(\kappa\cdot\mathbf{x}-\sigma t)}d\kappa d\sigma d\kappa"d\sigma". \tag{2.15}$$

Equation 2.15 can be simplified by defining $\kappa'\equiv\kappa"-\kappa$ and $\sigma'\equiv\sigma"-\sigma$

$$H(\mathbf{x},\mathbf{r};t,\tau)=\int_{\kappa"}\int_{\kappa'}\int_{\sigma"}\int_{\sigma'}\overline{B_3B_3^*}e^{i(\kappa'\cdot\mathbf{x}-\sigma' t)}e^{i(\mathbf{k}"\cdot\mathbf{r}-\sigma"\tau)}d\kappa"d\sigma"d\kappa'd\sigma'. \tag{2.16}$$

If we define $\Psi(\kappa",\sigma";\mathbf{x},t)$ as the generalized Fourier transform of the mean product $\overline{B_3B_3^*}$, we obtain

$$\Psi(\kappa",\sigma";\mathbf{x},t)=\int_{\kappa'}\int_{\sigma'}\overline{B_3^*(\kappa",\sigma")B_3(\kappa"-\kappa,\sigma"-\sigma)}e^{i(\kappa'\cdot\mathbf{x}-\sigma' t)}. \tag{2.17}$$

The covariance function 2.15 can now be written as

$$H(\mathbf{x},\mathbf{r};t,\tau)=\int_{\kappa"}\int_{\sigma"}\Psi(\kappa",\sigma";\mathbf{x},t)e^{i(\mathbf{k}"\cdot\mathbf{r}-\sigma"\tau)}d\kappa"d\sigma". \tag{2.18}$$

Taking the inverse of this function gives

$$\Psi(\kappa", \sigma"; \mathbf{x}, t) = (2/\pi)^{-3} \int_{\mathbf{r}} \int_{\tau} H(\mathbf{x}, \mathbf{r}; t, \tau) d\mathbf{r} d\tau. \tag{2.19}$$

Ψ is the general three-dimensional power spectrum of the sea surface displacement. The sea surface spectrum is the Fourier transform of the sea surface correlation function. It is a function of the wavenumber and position vectors and frequency and time scalars. Considering a Gaussian stationary process, the time variable can be suppressed. Assuming linearity, frequency $\sigma"$ can be defined according to the dispersion relationship

$$\sigma" = \sqrt{\frac{g}{\kappa"} \tanh(\kappa" h)} \tag{2.20}$$

where g is the gravitational acceleration and h is the waterdepth. This reduces the wave spectrum to a two-dimensional spectrum in the wavenumber space. Very short time lags are considered for the evolution of the sea surface spectrum.

The sea surface spectrum is used in electromagnetic models for the radar return from the ocean to model the shape of the surface. Elfouhaily et al. [6] derive a wave spectrum model that is able to describe diverse fetch conditions for wind and that provides agreement with in-situ observations. The Elfouhaily spectrum is used in the numerical models in this study. Short comings of the model are that the in-situ data it is tuned to is limited. The JONSWAP formulation, that is used to describe the long wave regime of the model, is based on North Sea data, whereas our data is in different locations.

2.4. Geophysical Model Functions for interaction between radar waves and ocean waves

2.4.1. Overview

In this section interaction between radar waves and ocean waves is addressed. Physical processes of the ocean itself have been discussed in section 2.3. The ocean wave spectrum defines the shape and movements that determine the wind/wave contribution to the returned radar signal. Electromagnetic models of the ocean are forward models, that give an estimate for SAR parameters given a wave spectrum. The wave spectrum itself is the output of a forward model of the wind vector. In this thesis forward models for the NRCS and Doppler Centroid are considered.

There is a sharp distinction between numerical/analytical models and empirical models. Empirical models do not rely on the before mentioned wave spectrum model, whereas numerical/analytical models do rely on a wave spectrum model. Wave spectrum model and numerical/analytical electromagnetic model are coupled and considered together the GMF. Empirical and numerical/analytical geophysical model functions are all a function of the wind vector and the radar angle of incidence. In this study only VV polarization is considered.

Numerical/analytical models can too be separated in two groups: two-scale Bragg scattering models and analytical asymptotic electromagnetic models. Note that the analytical asymptotic electromagnetic methods are not fully analytical, as the wave spectrum is based on statistics. Table 2.2 gives an overview of the available models. GMF's are categorised in empirical, asymptotic electromagnetic and numerical on the vertical and the SAR parameter they approximate on the horizontal.

In this study XMOD2 empirical GMF and the analytical electromagnetic model using a Kirchhoff Approximation (KA) are applied. More information on these models follows in this chapter. Two-scale models remain unused in this study, but are briefly discussed in this chapter.

The reason to use XMOD2 is the advantage of a fast computation time of the algorithm. The Kirchhoff Approximation has shown to be effective for steep incidence angles and to be insensitive to polarization [27] and since our data is acquired at incidence angles of 17°and a single VV polarization, this model was chosen as a model for the wave induced Doppler Centroid. For angles of incidence below 18° this model is also used for NRCS instead of XMOD2, because XMOD2 is only valid for the range of incidence angles between 18°- 40°.

XMOD2 is based on the same algorithm as CMOD5, which is widely used in scatterometry with C-Band radar. The algorithm can be found in Nirichio and Vanafra's paper[26]. The regression algorithm was applied

Table 2.2: Overview of ocean radar forward models for X-band radar. Underlined are the models used in this thesis. More information selected models follows in this chapter. All geophysical model functions are a function of the wind vector and radar angle of incidence and are for VV polarization. Numerical/analytical GMF's consist of a coupled wave model and an electromagnetic model. Empirical GMF's are dependent on coefficients obtained through regression on data.

model type	**Backscatter (σ_0)**	**Doppler (f_D or v_D)**
empirical	XMOD2	-
asymptotic electromagnetic[27] [25]	Kirchhoff Approximation Weighted Curvature Approximation	Kirchhoff Approximation Weighted Curvature Approximation
two-scale	Composite model [30] Semiemperical model [20] OceanSAR	OceanSAR

to 300 CosmoSkymed images.

Analytical electromagnetic methods methods were implemented in a software package developed by the Ifremer group. From the analytical electromagnetic methods the one using a Kirchhoff Approximation was used for this study. This method models the ocean surface as small surfaces that are tangent to the waves. It is also refered to as the *tangent plane method* [5].

For this approximation the sea surface wave spectrum is assumed to be a linear Gaussian variable, then time-dependent asymptotic solutions for the normalized radar cross section can be obtained [25]

$$\sigma_0(\theta,\Phi,t) = \left|\frac{N_0(\mathbf{k},\mathbf{k_0})}{Q_z}\right|^2 e^{-Q_z^2\tilde{\rho}(0,0)} \int_{\mathbf{r}} \left[e^{-Q_z^2\tilde{\rho}(\mathbf{r},t)} - 1\right] e^{-iQ_H\mathbf{r}} d\mathbf{r}, \tag{2.21}$$

where θ is the angle of incidence, Φ is a modified sea surface height function, which is a zero-mean, ergodic, stationary Gaussian variable. t is the time parameter. This time lag is considered very small, since the PRF is high. $\mathbf{r}$ is the horizontal component of the position vector. $\mathbf{k_0}$ and $\mathbf{k}$ are the horizontal components of the wave vector for the incident wave and scattered wave respectively. q_0 and q_k are the vertical components of the incident and scattered wave vector. $Q_H = \mathbf{k} - \mathbf{k_0}$ and $Q_z = q_0 + q_k$. N_0 is a zeroth order kernel that depends on the Kirchhoff solution. $\tilde{\rho}$ is the correlation function of the filtered sea surface spectrum.

Equation 2.21 has an imaginary term. This term can be rewritten as a phase term and from this the Doppler frequency shift is derived.

$$f_{Dc} = \frac{1}{2\pi t}\left[\frac{Im(\sigma_0(\theta,\Phi,t))}{Re(\sigma_0(\theta,\Phi,t))}\right] \tag{2.22}$$

The Weighted Curvature Approximation(WCA) writes a correction to the used Kirchhoff solution in the form of a Kirchhoff integral involving second-order spatial derivatives of the surface. Curves instead of tangent planes are a more accurate representation of wind induced ocean waves. It also supresses sidelobes w.r.t. the discontinuous tangent plane method.

The WCA is more sensitive to polarization than the KA and the WCA is more robust for larger incidence angles [27]. Therefore it may be a useful model to use in the retrieval algorithm for acquisitions with less steep incidence angles and in future it may be used for dual polarized ATI acquisitions.

Two-scale models for radar scattering from the ocean surface remain unused in this study and are classified 'two-scale' in table 2.2. It is worth mentioning these models, as in future they can be used in the retrieval algorithm developed in this study as well as the other models to find the most suitable ocean radar GMF.

The composite ocean surface model presented by Romeiser and Alpers[30] is based on a two-dimensional resonant *Bragg scattering theory* from wind waves superposed on longer tilting waves. Resonant Bragg scattering is the dominant scattering mechanism on the ocean for X-band radar, as wind waves are of a similar wavelength as the radar waves. This model is implemented to the OceanSAR package, with the addition of a specular scattering mechanism. The semiempirical model introduced by Kudryavtsev[20] adds the non-Bragg components of specular scattering and wave breaking statistics (hence semiempirical) to the composite model.

2.4.2. Geophysical model function for Doppler centroid: the Kirchhoff Approximation

The Doppler Centroid model used in this study is expressed as a Doppler frequency. Frequency parameter is converted to velocity using the following expression[38]:

$$f_{Dc} = \frac{2v_r}{\lambda}, \tag{2.23}$$

where f_{Dc} is the Doppler Centroid Frequency (Hz), v_r the velocity line of sight and λ the radar wavelength.

The sea surface in the Kirchhoff approximation can be expressed as a function of the wind speed magnitude and wind direction, therefore the resulting values for Doppler Centroid velocity can be simplified as

$$v_{Dc}(\bar{U}_{10}, \phi, \theta), \tag{2.24}$$

where $\bar{U}_{10}$ is the wind speed magnitude in m/s, ϕ the wind direction in degree and θ the angle of incidence. Figure 2.6 and 2.7 show the KA model evaluated for a fixed incidence angle. Figure 2.7 shows the model as a function of wind speed magnitude and figure 2.6 the model as a function of wind direction. Figure 2.8 shows the model evaluated with varying incidence angle, but fixed wind direction and magnitude. It can be seen that variations as a function of incidence angle are small compared to the variations with the wind speed magnitude and direction.

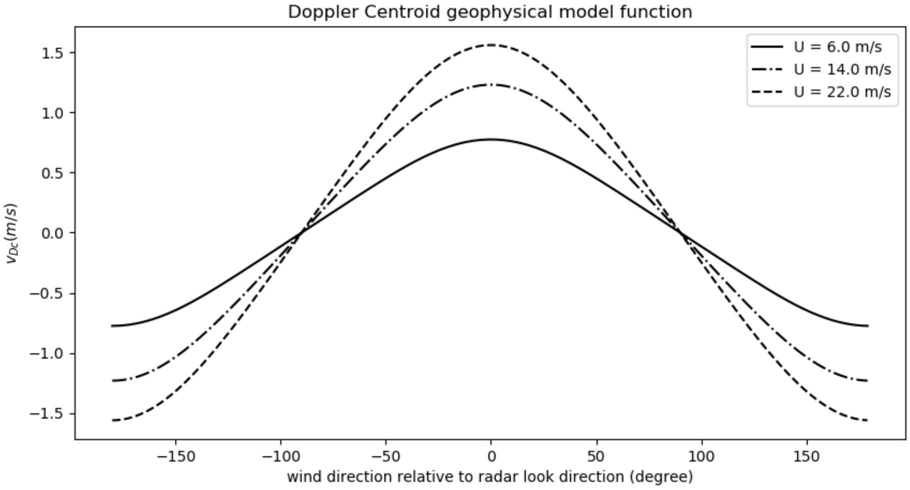

Figure 2.6: Geophysical model function for Doppler centroid expressed as a velocity. The function is computed for an incidence angle of 17 degrees and it is a function of wind speed and wind direction relative to radar look direction. The function (eq. 2.24) evaluated for wind speed 6, 14 and 22 m/s and plotted as a function of wind direction. Extremes occur in up-wind and down-wind direction and perpendicular to radar line of sight there is no sensible motion in line of sight of the radar, therefore, the function is 0 at 90 degrees.

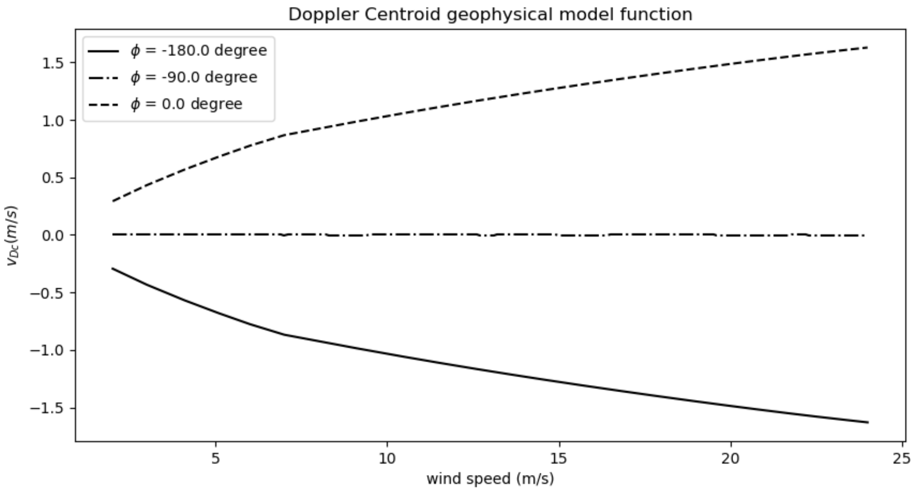

Figure 2.7: Geophysical model function for Doppler centroid expressed as a velocity plotted as a function of wind speed for wind direction angles -180, 90 and 0 degrees (up-wind, perpendicular wind and down-wind). Doppler Velocity of the ocean surface associated with wind increases with higher wind speed, except if the wind direction is nominal to radar look when no component of Doppler velocity is measured in radar line of sight.

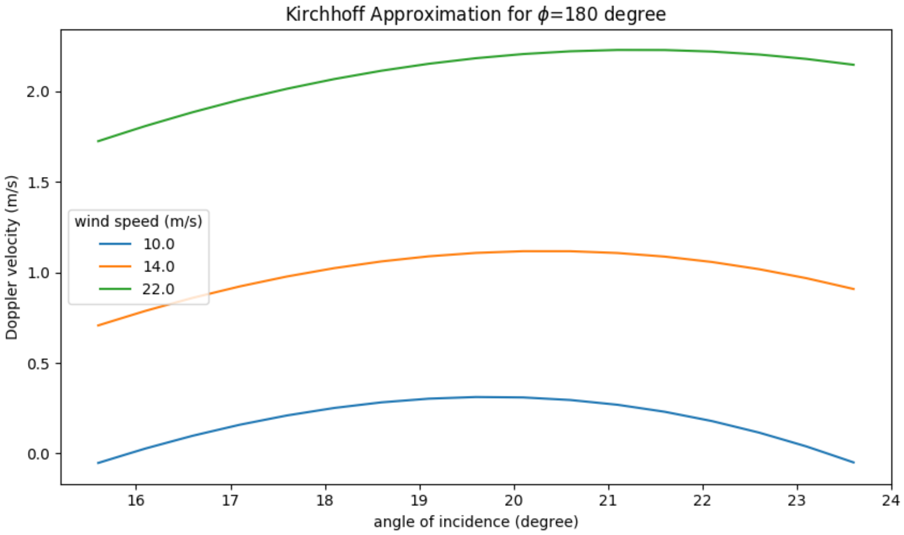

Figure 2.8: Geophysical model function for Doppler centroid expressed as a velocity plotted as a function of angle of incidence. Incidence angle dependence of the Doppler centroid is non-linear, but small compared to wind speed and wind direction dependence.

2.4.3. Geophysical model function for normalized radar cross section: XMOD2 and the Kirchhoff Approximation

There are two GMF's that are used to retrieve the wind vector from the NRCS observations: empirical GMF XMOD2 and the same model as for the Doppler Centroid. In this section both GMF's are presented and compared.

The two GMF's that are used in this study are displayed in figure 2.9, both evaluated at an angle of incidence of 22°. The Kirchhoff approximation estimates NRCS to be higher than XMOD2 as can be seen in figure 2.9. The true NRCS as a consequence of wind is complicated to validate. It is a good idea to interpret results as if the truth lies somewhere in between of the models.

Backscatter as a function of relative wind direction is a symmetric oscillating function. Highest backscattered power occurs when radar look angle is in the same or opposite direction of the wind. Lowest backscatter occurs when the radar look is perpendicular to the wind. An expression of the forward backscatter model is given by

$$\sigma_{0,model}(\bar{U}_{10}, \phi, \theta), \tag{2.25}$$

where $\bar{U}_{10}$ is the magnitude of wind speed 10 m above the sea surface, θ the radar angle of incidence and

$$\phi = \alpha - \psi, \tag{2.26}$$

where α is the azimuth angle of the wind (wind direction), ψ the radar azimuth angle (approximately 7.5 °squint on the ground between beam and across-track direction).

As a function of wind speed the function increases as shown in figure 2.10. In a StripMap SAR image, the incidence angle varies over range. Change of the GMF as a function of angle of incidence can be seen in figure 2.11.

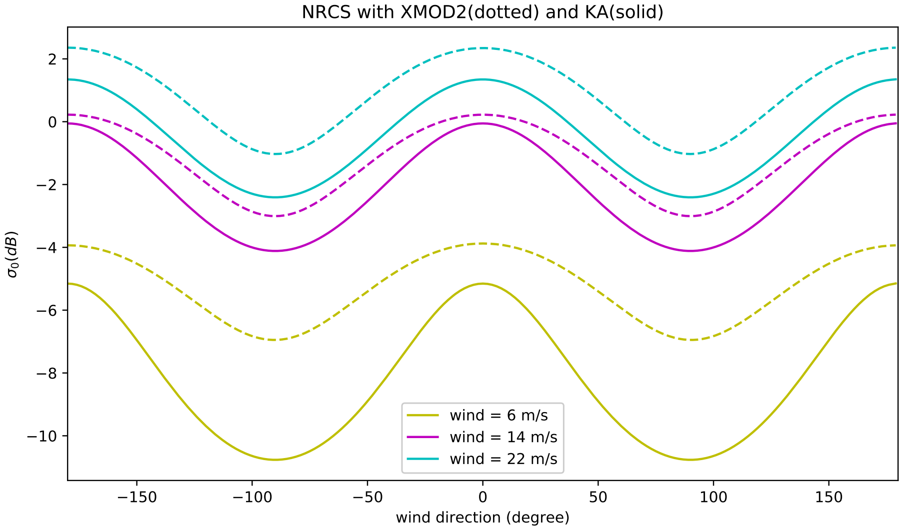

Figure 2.9: Geophysical model function for backscattered amplitude expressed as a Normalized Radar Cross Section. The function is computed for an incidence angle of 22 degrees and it is a function of wind speed and wind direction relative to radar look direction, which is refered to as wind direction. Overall XMOD2 gives a higher estimate for σ_0 than the Kirchhoff Approximation.

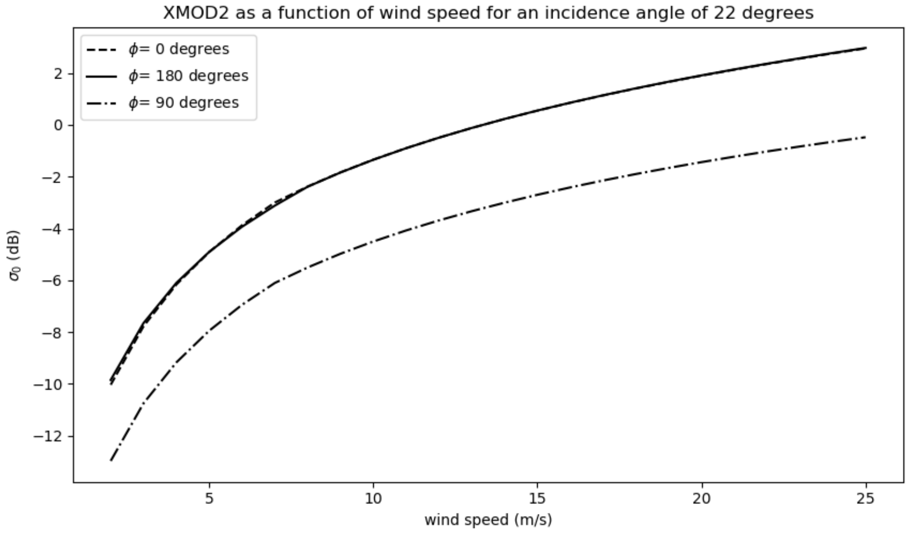

Figure 2.10: Geophysical model function for backscattered amplitude expressed as a Normalized Radar Cross Section plotted as a function of wind speed for wind direction angles -180, 90 and 0 degrees (up-wind, perpendicular wind and down-wind). Upwind and downwind show the same wind speed dependence. Wind angles display the same curve with approximately the subtraction of a constant.

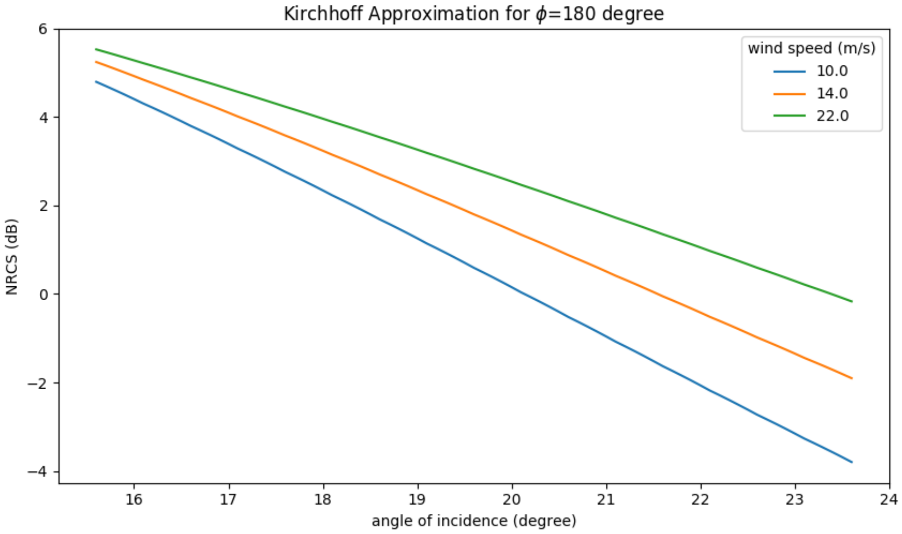

Figure 2.11: Geophysical model function for Normalized Radar Cross Section plotted as a function of angle of incidence. NRCS variations are large as the incidence angle changes.

Summary

In this chapter theoretical background was provided on SAR imaging, imaging with experimental TanDEM-X BiDi ATI and about physical processes on the ocean to finally provide models for radar return from the ocean surface.

The SAR principle relies on an imaging system, with a transmitter, antenna and receiver. It sends pulses from the satellite to the ground and records the echo of these pulses. By applying SAR processing techniques to the received echo's, very high spatial resolution is achieved. Most important SAR parameter for this study is the Normalized Radar Cross Section. The Noise Equivalent Sigma Naught (NESZ) is the NRCS for which SNR equals zero. The Doppler Centroid is an important parameter for interpretation of the ATI phase.

Along-track interferometric phase is the other most important SAR parameter in this study. Interferometry allows us to observe a phase signal, by subtracting the phase of two coherent SAR images. The phase signal relates to motion of the sea surface with Along-Track Interferometry. TanDEM-X Bidirectional imaging mode splits the antenna pattern into two lobes seperated as far as possible in azimuth direction. With the constellation of TanDEM-X and Along-Track Interferometry it is possible to observe the horizontal components of motion of the ocean surface.

In the retrieved vector field we expect to predominantly see currents and waves. Wind induced waves are the dominant contributor to the ATI phase. Wind waves are expressed as a wave spectrum. Observation of currents at submesoscale may reveal processes not often observed. Large-scale currents show a northward stream along Norway upto the north of Novaya Zemlya. Tidal currents may dominate the retrieved TSCV image. Large-scale as well as tidal currents are expected to be stronger in Tromsø than in Novaya Zemlya.

The wave spectrum is used to model the ocean surface and predict NRCS and Doppler Centroid. Two models are selected for the retrieval algorithm: XMOD2 and the Kirchhoff Approximation. XMOD2 is an empirical geophysical model function for NRCS and the Kirchhoff Approximation is a numerical geophysical model function for both NRCS and Doppler Centroid. These GMF's for the NRCS and Doppler Centroid are used in the wind retrieval and TSCV retrieval algorithm respectively, which will be presented in the methodology.

In the next chapter the data is introduced and pre-processing steps are presented.

3

Data and pre-processing

In this chapter a description of TanDEM-X BiDi ATI data is given as well as the locations of the data sets used in this study. Calibration steps that need to be performed on the data before wind and TSCV retrieval are explained in section 3.3.1. Equations for radiometric calibration are presented and quality of radiometric calibration is analyzed after the calibration was implemented. The phase calibration process is described in detail. In the last section selected data after implementation of radiometric calibration is presented and analyzed and further calibration is applied to these data sets.

3.1. TanDEM-X Bidirectional Along-Track Interferometric data

TanDEM-X Bidirectional data is experimental and it requires alternative SAR processing software, other than the software used for StripMap acquisitions with nominal looks. The processing software used for SAR processing of TanDEM-X BiDi data is referred to as TAXI. It was also developed for the more well known TOPS SAR mode of Sentinel-1.

3.1.1. TanDEM-X data products

TAXI works with SAR product levels, just as most SAR processing software. Table 3.1 gives a compact overview of the SAR levels and what kind of data they contain and a description of the data.

In this study mostly L-2 products are used. L-0 products were unavailable due to data policies, but L-1 products were. Level-0 products have been focused (section 2.1.1) and radiometrically calibrated (section 3.3.2) by TAXI to generate L-1 products. L-1 products are given as a *Single Look Complex*(SLC). This implies that the resolution cell is the smallest cell possible (5 m x 5 m for TanDEM-X), that was acquired through SAR processing. TanDEM-X Bidirectional ATI data consists of the following Level-1 products:

- SLC fore TDX
- SLC aft TDX
- SLC fore TSX
- SLC aft TSX

The Level-1 products were used to validate the quality of calibration. For rest of the study Level-2 products were more suitable. L-1 products are coregistered to produce an interferogram out of two images.

Multilooking is applied to the L-1 products to reduce noise and as a consequence spatial resolution. Multilooking is an operation that takes the average of a block of cells and subsequently downsamples the image to one cell per block. The amplitude, phase and coherence L-2 product data is smaller in size than that of the L-1 products. The TanDEM-X Bidirectional ATI Level-2 product consists of the following data:

- Amplitude fore
- Amplitude aft

- Coherence fore
- Coherence aft
- Interferometric phase fore
- Interferometric phase aft

With the L-2 products, further post-processing of the interferometric phases of BiDi ATI images leads to a Doppler velocity field as shown in figure 3.4. Section 2.2.2 gives equations and a description of the involved processing steps.

Table 3.1: TerraSAR-X product levels

level	data product	description
0	Raw	Raw data matrix
1	Single Look Complex	Radiometrically calibrated and focused
2	Post-processed	Interferograms and multilooked

3.1.2. Data selection and data locations

Data used in this study comes from the BiDi experimental phase of TanDEM-X in the years 2013 and 2014. This experimental phase produced ATI data sets with high height of ambiguity (1000>), implying that the perpendicular baseline is small. Data selection is based on the requirement of small baselines and the requirement of sea area with no ice. Table 3.2 gives details on the data sets used in this study. Preliminary data was used for the development of the algorithm.

Table 3.2: Details on the TanDEM-X Bidirectional ATI data acquisitions used in this study. Preliminary data was used for the development of the algorithm.

Location	UTC date and time	height of ambiguity average (m)
Novaya Zemlya (preliminary)	13.09.13 11:40:26	?
Novaya Zemlya	22.08.13 11:39:49	3423
Tromsø	04.09.13 15:47:58	8812

Data sets that meet the requirements are located in Tromsø(Norway) and Novaya Zemlya (Russia). These acquisitions both have an ascending orbit. Figure 3.1 displays the location of the Novaya Zemlya data set. This acquisition lies over the Kara Sea and the Barents sea. The seas are ice free in August when data was acquired. This is the location of preliminary data and of the data used in the results. Figure 3.2 shows the location of the acquisition over Tromsø. This acquisition is shorter than the acquisition over Novaya Zemlya and it contains more complex topography.

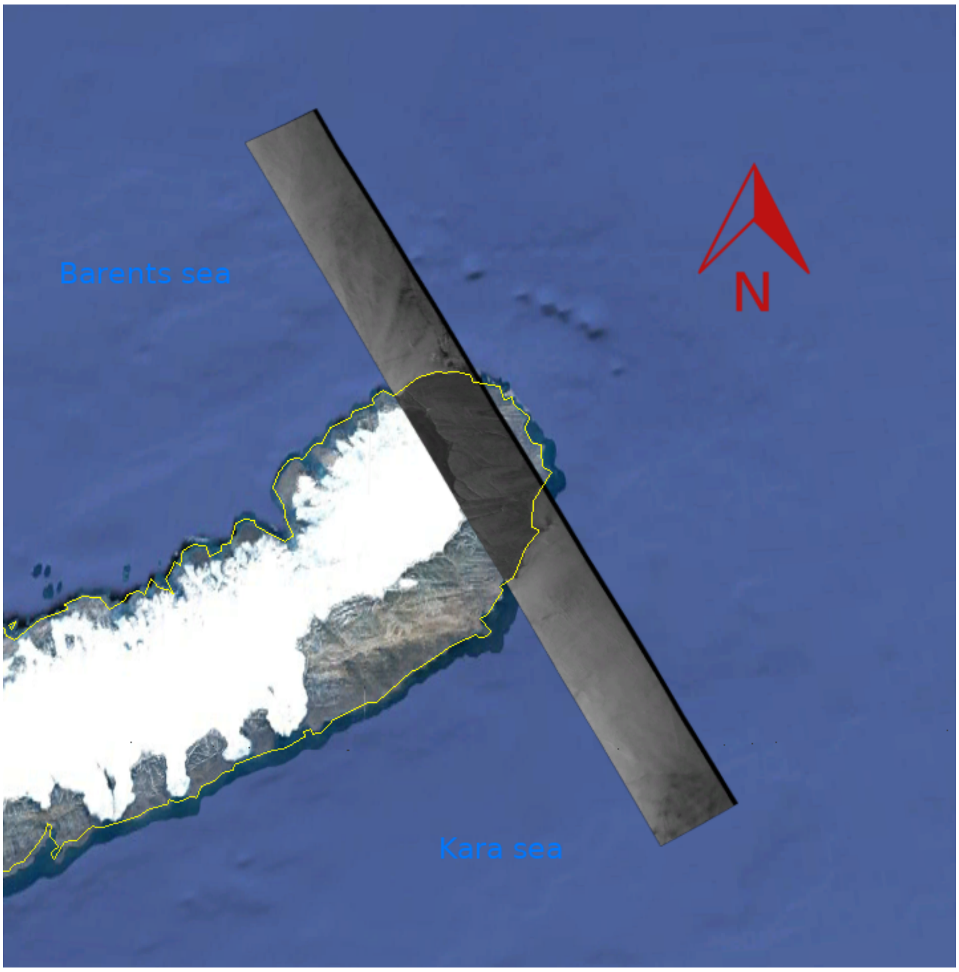

Figure 3.1: Bidirectional ATI acquisition over the Barents sea and Kara sea, with the tip of Novaya Zemlya. The latitudes of the image vary between 75.5 and 78.2 degrees North and the longitudes of the image between 63.5 and 70.9 degrees East. North is up in the image. More details on the acquisition can be found in table 3.2.

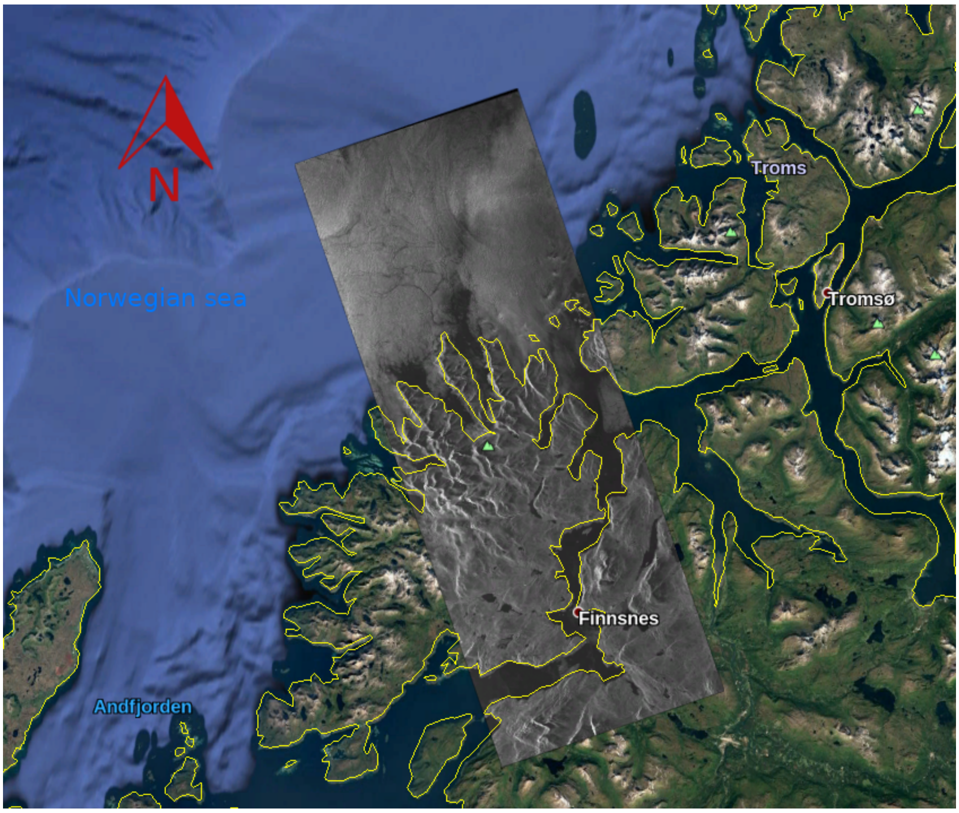

Figure 3.2: Bidirectional ATI acquisition at the coast near Tromsø . The latitudes of the image vary between 68.9 and 70.3 degrees North and the longitudes of the image between 17.7 and 18.6 degrees East. North is up in the image. More details on the acquisition can be found in table 3.2.

3.1.3. Preliminary data

Preliminary data presented in this section is used for development of the wind- and total surface current vector retrieval algorithm. Figure 3.3 shows the fore- and aft L-2 products of TanDEM-X BiDi ATI data. These L-2 products contain the intensity, coherence and phase of both beams. The intensity and phase are uncalibrated and the fore- and aft image differ slightly due to the squinted look. The image shows a land area, which displays green for the phase image (zero), and shows features as an icecap in the bottom part of the land area. Features in the intensity image on land can be associated with topography. Left of the land area there is a signature at sea that can be recognized in all images. This signature is connected to a storm event.

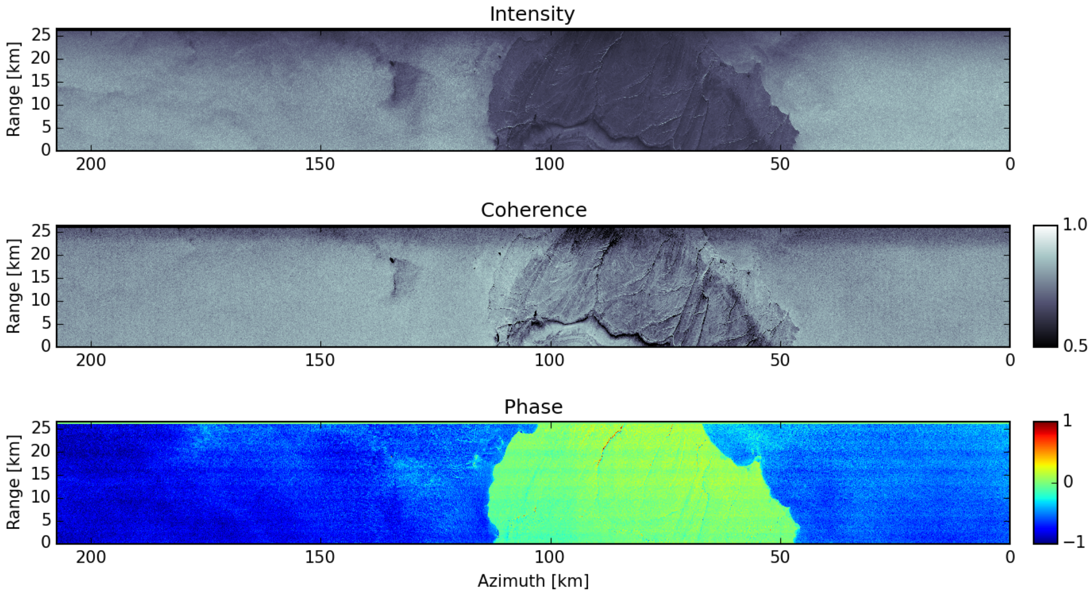

(a) Fore

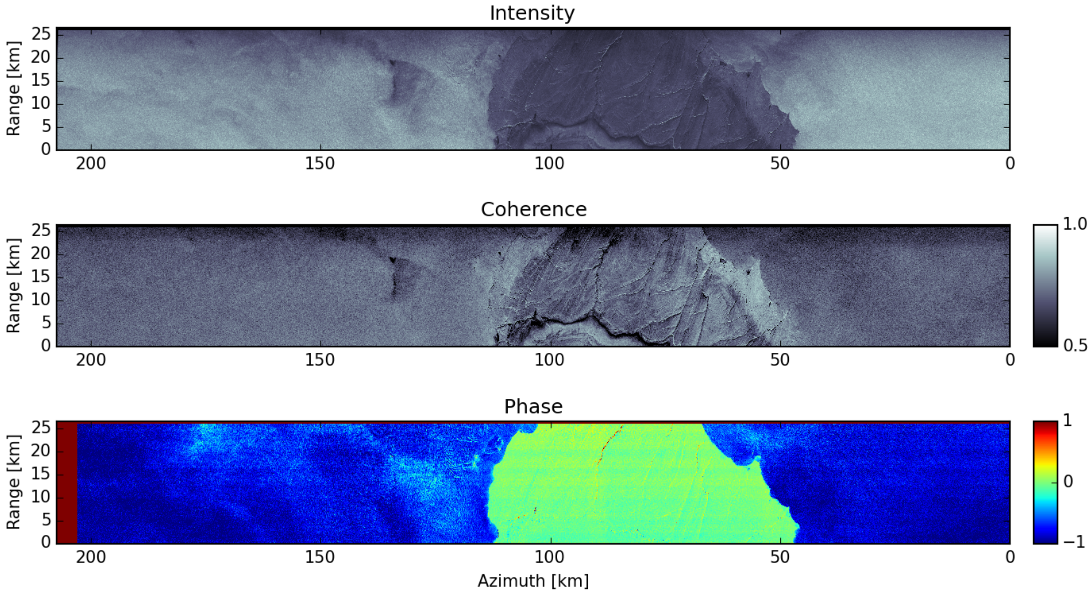

(b) Aft

Figure 3.3: TanDEM-X BiDi L-2 products consisting of two intensity images, two coherence images and two phase images. Polarization is VV. From the ATI phase ATI Doppler vectors were derived as displayed in figure 3.4. Intensity is uncalibrated and the signature left of the land area is a storm event.

Figure 3.4 shows the preliminary Doppler field that was retrieved from the ATI phase of figure 3.3 [22]. The Doppler velocity is zero on land as the ATI phase. This Doppler field contains a wave bias, as can be seen on the right of the image, where the stream lines go straight at the coast.

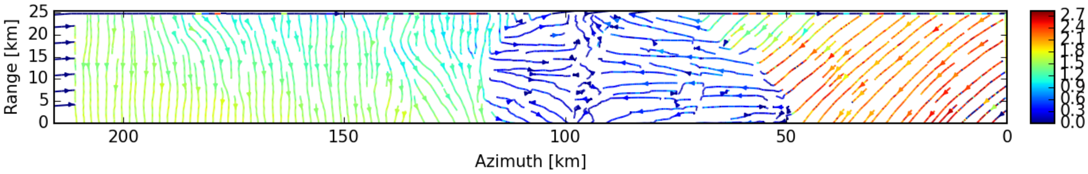

Figure 3.4: Doppler field as derived from the L-2 products in figure 3.3. Land area is blue and the direction of the vectors on the right pointing straight at the coast indicates that there is a large wind geophysical bias to the ATI phase.

3.2. External data sources

For validation and as a constraint on the solution for wind direction, reference wind data is needed. Due to the lack of ocean buoys in areas of the available data sets, the data that is most suitable comes from atmospheric reanalysis models. These models have been assimilated with various atmospheric data to come to a reasonable estimate for the wind field at the time of acquisition.

Reanalysis model ECMWF ERA-5 has highest spatial resolution of all ECMWF models and is therefore most suitable. However, the 30 km resolution is not nearly as high as SAR resolutions up to 5 m. Interpolation of the data is needed to get an estimate for the wind vector in the SAR grid points. For validation the interpolated wind vectors need to be compared with an average of the SAR retrieved winds, as small scale structures will not display in the interpolation. Figure 3.5 displays a map that illustrates the interpolation technique.

ECMWF ERA-5 gives an estimate for the wind velocity component U and V at 10 meters above the sea surface. The V components is positive in the North and the U component is positive to the East. U-V axes need to be rotated to the local SAR grid.

ECMWF ERA-5 has a temporal resolution of three hours. The time sample of ECMWF ERA-5 closest to acquisition time is chosen as a reference data set. Table 3.2 gives the acquisition times of Tromsø and Novaya Zemlya, which are 15:47 and 11:39 respectively. Corresponding ECMWF ERA-5 time samples are 15:00 and 12:00.

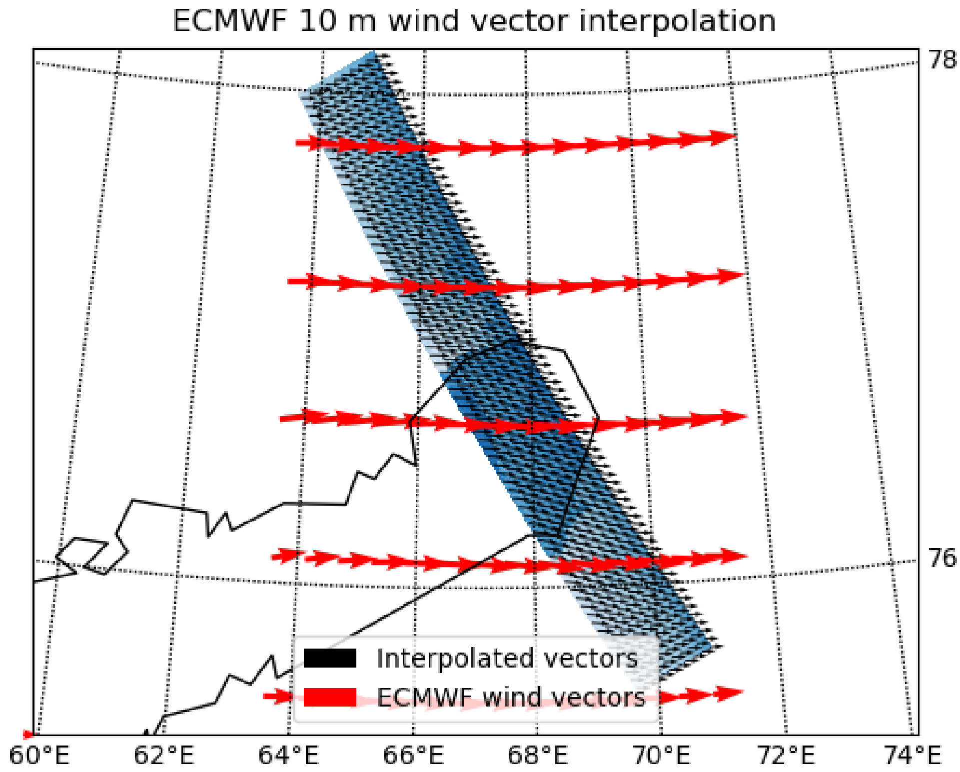

Figure 3.5: Interpolation of the ECMWF ERA-5 Reanalysis model data to the SAR grid. ECMWF ERA-5 data is from August 22th 2013 12:00. Using the corners in geodetic coordinates of the SAR image, an algorithm is developed to acquire approximate geodetic coordiantes of the SAR grid points. ECMWF wind data is interpolated to the defined grid using a linear interpolator. This result of ECMWF interpolation is the black arrow, whereas the original vector is depicted with a red arrow. ECMWF coordinates are rotated to the SAR grid, where orbit path is the x-axis and nominal radar look the y-axis.

3.3. Calibration

In this section necessary calibration steps that need to be performed on TanDEM-X BiDi data in order to perform wind and TSCV retrieval are presented. Implementation of radiometric calibration to the experimental SAR processor TAXI and a conversion of the L-1/L-2 amplitude data are needed to finally obtain a NRCS. Subsequently a quality check on the radiometric calibration is performed. The phases of the beams have an offset with respect to each other, that leads to errors in the TSCV. This offset needs to be corrected for. This step is refered to as phase calibration.

3.3.1. Radiometric calibration

In this subsection radiometric calibration and conversion of L-1 and L-2 amplitudes are given.

A radiometric conversion is implemented to the TAXI processor. In the operational processing chain of TerraSAR-X the beta naught coefficient is defined as follows [14]:

$$\beta_0 = k_s \cdot |DN|^2, \tag{3.1}$$

where DN are digital numbers and k_s is the calibration factor. DN is the amplitude of the complex number from the raw data and β_0 is the pixel intensity. k_s can be found in the TerraSAR-X data delivery package.

The experimental SAR processor TAXI expresses intensity as Beta Naught (β_0), whereas geophysical model functions use NRCS. The L-1 and L-2 products that come from the processing chain therefore need a conversion to NRCS (NRCS). Fortunately this conversion is fairly simple, as NRCS is simply the projection of Beta Naught to ground range. The conversion is defined as follows:

$$\sigma_0 = (\beta_0 - NEBN) sin(\theta_{loc}), \tag{3.2}$$

where NEBN is the Noise Equivalent Beta Naught. Multiplied with the sine of the local incidence angle θ_{loc} this becomes the Noise Equivalent Sigma Zero (NESZ).

Signal to noise ratio of bidirectional TanDEM-X is 3.7 dB lower than the SNR of nominal StripMap images [24], therefore NESZ is 3.7 higher than for nominal TanDEM-X. Nominal TanDEM-X typically has a NESZ of around -20 dB [14]. NESZ for Bidirectional TanDEM-X then follows from equation 2.2 and this gives us a value of -17 dB. Higher SNR is the result of splitting the antenna into two beams.

3.3.2. Calibration quality analysis

Calibration in TAXI is similar to that of the operational TanDEM-X processor (PGS). The operational processor operates on acquisitions with nominal looks. Therefore, if the calibration is implemented correctly, both TAXI and PGS should process acquisitions with nominal looks correctly.

To check the calibration for TAXI, a comparison of Stripmap acquisitions of rainforest is made. The acquisitions are at different angles of incidence, to check the lookangle dependence. The reflective properties of rainforest are homogeneous and therefore these acquisitions are often used for calibration. The goal of this analysis is to check for trends in range and azimuth direction. Note that this check neglects the BiDi mode, as PGS is unable to process TanDEM-X data for squinted angles the check cannot be performed for BiDi mode specifically.

The acquisitions processed with the operational processor (PGS) were coregistered with the acquisitions processed by TAXI. The coregistered grids are divided in blocks and for each block a mean intensity is computed. The ratio of mean intensity PGS/TAXI gives an indication of the relation. If there is a trend in this quantity in range or azimuth direction it indicates errors in the calibration. Figure 3.6 shows the amplitude ratio's for all StripMap rainforest acquisitions. No trends in range direction are seen for look angles between 20°and 55°.

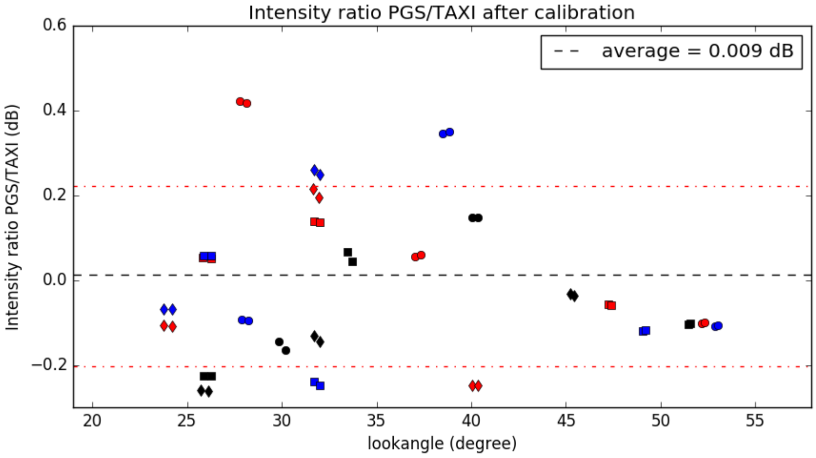

Figure 3.6: Mean ratio PGS/TAXI amplitude of nominal TDX StripMap acquisitions over rainforest area as a function of the look angle. Each different color/shape represents another acquisition. Over the lookangle no trend is seen, only a variability in amplitude ratio depending on the acquisition.

To compare the phase following from PGS with the phase following from TAXI, the complex interferogram of the data set processed with PGS and TAXI is taken (equation 3.3). The phase angle following from this complex multiplication gives the difference in phase from PGS and TAXI processing $\phi_{PGS} - \phi_{TAXI}$. First the SLC's are multilooked and then the following operation is applied:

$$S = S_{PGS} \cdot S_{TAXI}* \tag{3.3}$$

For the same cells, also the ratio of amplitudes is computed. The phase angle difference and the amplitude ratio are plotted as a function of range/lookangle in figure 3.7 and as a function of azimuth in figure 3.8. For this the sum respectively over azimuth and the sum over range are taken and divided by the number of azimuth and range cells.

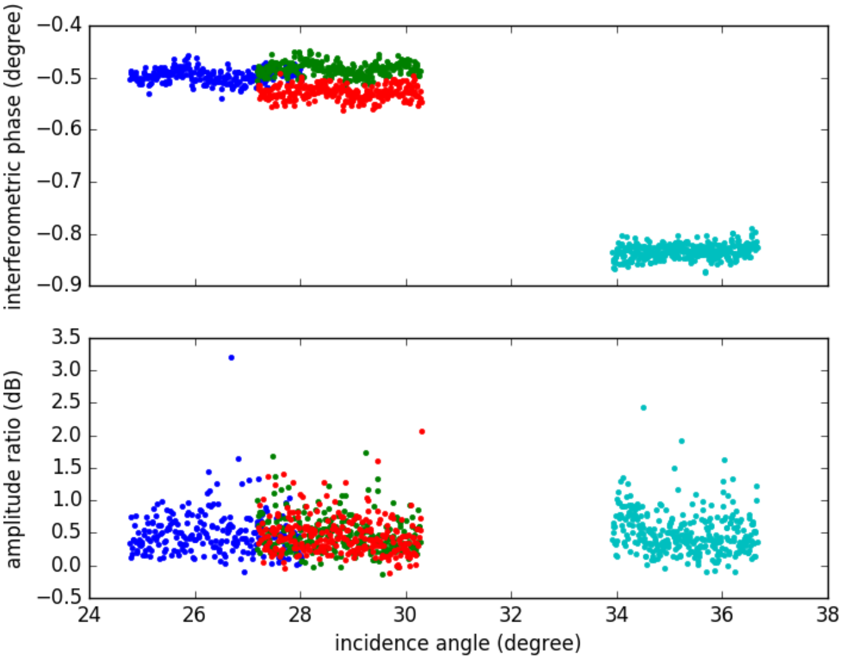

Figure 3.7: Top plot represents the phase angle difference PGS-TAXI as a function of incidence angle and the bottom plot represents the amplitude ratio PGS/TAXI. The colors distinguish the acquisitions. Trends are seen for phase nor amplitude, but the spread of the amplitude ratio's is very large. It was reasoned that this could be due to the very small amplitudes, but the same result is achieved by making a summation before division or by subtracting the amplitude. The phase angles are close to zero, which is to be expected for the interferogram of the same data set.

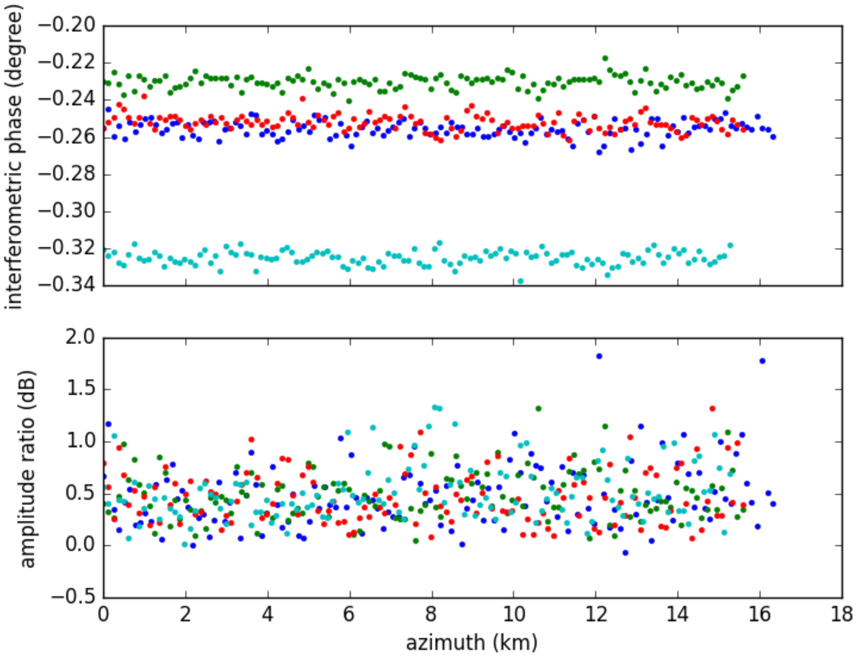

Figure 3.8: Top plot represents the phase angle difference PGS-TAXI as a function of azimuth and the bottom plot represents the amplitude ratio PGS/TAXI. Again no trends are detected, but a large spread of amplitude ratio's. A trend in the azimuth direction would indicate instrument drift.

3.3.3. Phase calibration

Phase errors in TanDEM-X BiDi ATI data have a certain origin. To grasp the origin of phase errors, interferometric phase is decomposed in the following elements:

$$\phi = \phi_{ATI} + k_z \Delta h + \phi_{radar} + \Delta az 2\pi f_D \Delta t_{az}, \tag{3.4}$$

where $k_z = \frac{2\pi}{h_{amb}}$ is the fringe frequency in units (m^{-1}), Δh, the residual topography (m), ϕ_{radar} the phase noise from the radar itself $(cycles)$, Δ_{az} the coregistration error $(cycles)$, f_D the Doppler frequency (Hz) and $\Delta t_{az} = \frac{pixelspacing}{v_{s/c,ground}}$ the integration time (s).

Based on this phase model, there will be errors in the phase from residual topography, radar noise and from coregistration errors. There may also be errors due to phase ambiguities at the sea-land margins. Topography is flattened in the L-2 products.

Assuming these errors account for a constant offset between the beams, a methodology is adopted to correct for a phase offset. Taken that the ATI phase should be zero on land, the correction is conducted by means of estimating the offset from 0 on land for each beam weighting each point with the coherence to avoid including areas of noisy phase to the estimation

$$i_{offset,b} = \sum_{j=1}^{M} W_j \cdot i_{land,b,j}, \tag{3.5}$$

where b is the beam number (1 for fore, 2 for aft), $i_{offset,b}$ the phase offset in the fore- or aft beam, W_j a weight given to each pixel, $i_{land,b,j}$ the interferometric phase of points on land in complex notation.

The weights are defined by the inverse of the phase variance and digital elevation model (DEM) variance

$$W_j = \frac{1}{\sigma_{phase,b} + \sigma_{dem,b}}. \tag{3.6}$$

Phase noise is defined as a function of coherence(γ) and number of looks of the resolution cell (N_{looks})

$$\sigma^2_{phase,b} = \frac{1 - \gamma^2_{land,b}}{2 \cdot N_{looks} \cdot \gamma_{land,b}}. \tag{3.7}$$

Standard deviation of the DEM is assumed to be 2 m in this approximation and the variance of the DEM then follows from

$$\sigma^2_{dem,b} = k_{z,b} \cdot \sigma^2_{dem}, \tag{3.8}$$

where $k_{z,b}$ the fringe frequency for the beam.
Subtracting the phase offset gives an ATI phase that is zero on the average on land

$$i_{b,c} = i_b - i_{offset,b}. \tag{3.9}$$

3.4. L-2 products and calibration of selected TanDEM-X data

TanDEM-X L-2 product data of Tromsø and Novaya Zemlya (figure 3.9 and 3.13) presented in this section were processed after implementation of radiometric calibration to the TAXI processor. First the data of Tromsø is analyzed and where necessary further calibrated, then we continue with the data of Novaya Zemlya.

Land areas of Tromsø suffer from layover (see also chapter theory 2.1.1) due to high topography of the coast. Also shadowed areas are seen in the image, corresponding with low intensity and low coherence areas. The NRCS average over the land area is -16.59 dB, while the NRCS over sea is -15.78 dB. Backscatter difference between land and sea is therefore only 0.81 dB. The small difference between signal on land and at sea indicates that chances of phase ambiguities on the land areas are high and therefore troubling the calibration. In the phase correction the layover and shadows need to be excluded from the calibration area. To avoid these areas, a mask is created manually to restrict area for calibration to the northern part of the land. This mask is displayed in figure 3.12. Shadow areas are excluded by weighting with coherence.

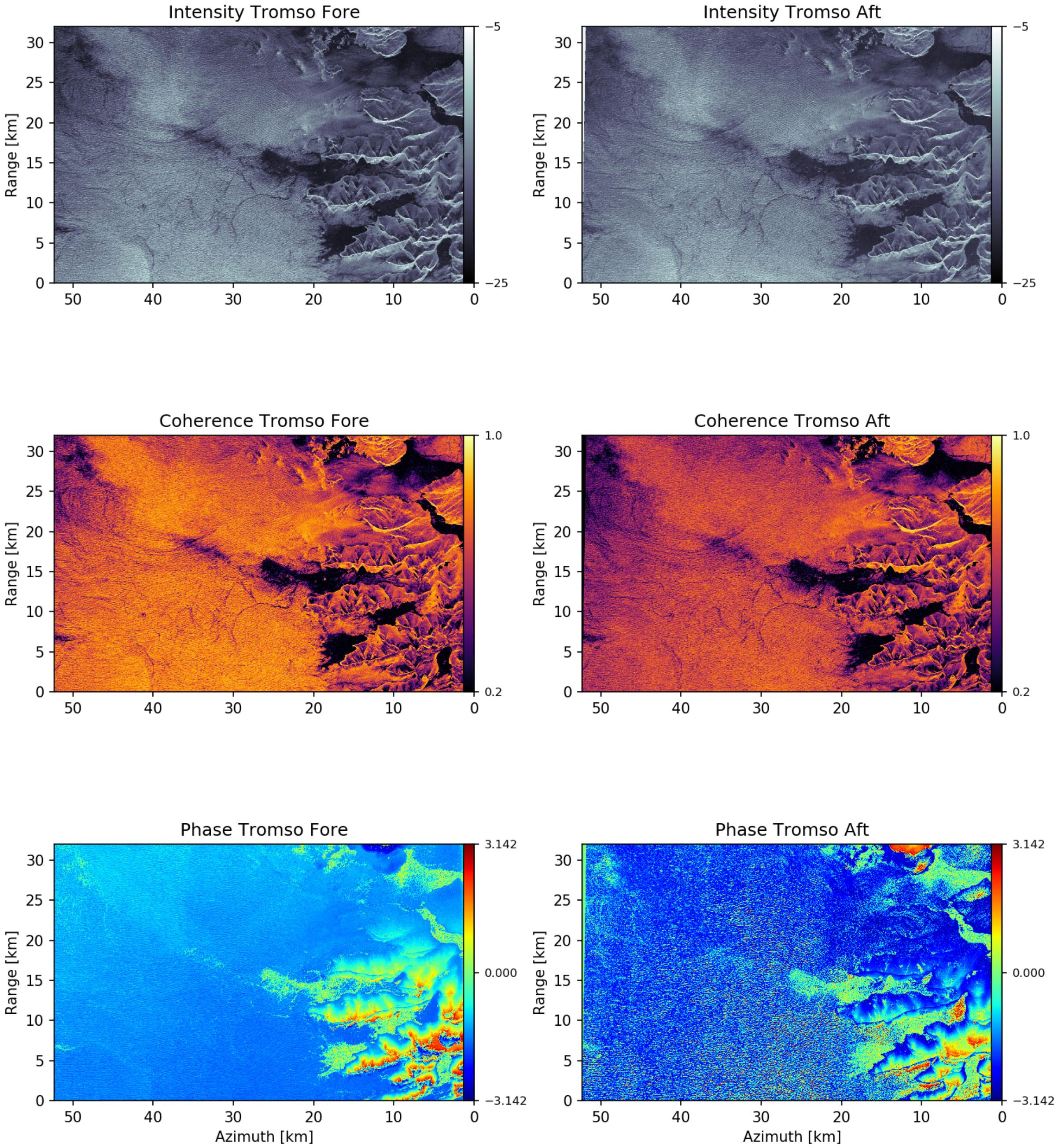

Figure 3.9: Uncorrected L-2 products. The intensity is expressed in NRCS in dB (m^2/m^2). Layover effects are seen on the land areas, giving rise to unordinary phase values in the bottom right of the phase image. NRCS difference between land and sea is 0.81 dB, therefore ambiguities may be present in calibration areas. Incoherent diagonal line marks an undefined geophysical signal.

It is noticed that the values of σ_0 in figure 3.9 are far off the values predicted using ECMWF wind vectors (figure 6.4) as input for XMOD2. The histograms below show the range of values of σ_0 (subfigure 3.10a) and the difference with the prediction of XMOD2 (subfigure 3.10b). The mean difference between modeled values of σ_0 and observed value lies between 6 and 7 dB.

This offset between model values and observations presumably arises from an inconsistency with corrections in the TAXI processing chain. It is therefore decided to correct σ_0 with an addition of 7 dB, to guarantee the inversion of a wind vector. However, the retrieved wind vectors need more caution with interpretation, as the results may be biased.

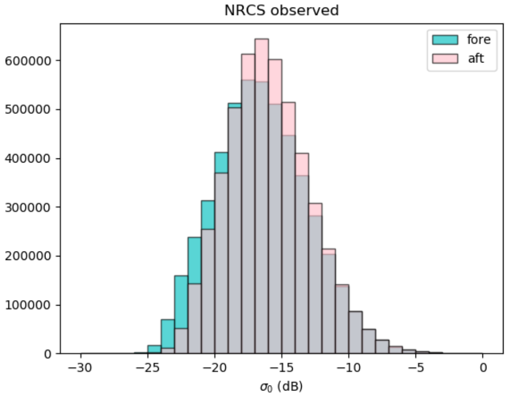

(a) Difference between modeled values of σ_0 and observed value lies between 6 and 7 dB. This suggests a systematic bias in the NRCS observations. σ_0 was modeled by evaluating XMOD2 with interpolated wind vectors of ECMWF.

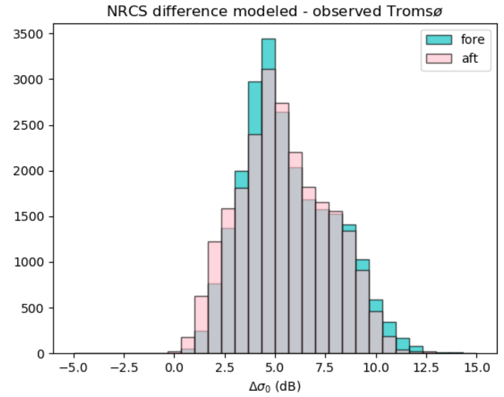

(b) Measured σ_0 values as from the intensity image in figure 3.9. σ_0 appears to have low values w.r.t. the model. This suggests an error in radiometric calibration.

To get a better understanding of the calibration error, the average NRCS on land of the squinted beams are compared with a quicklook of the NRCS from a TanDEM-X acquisition with nominal radar look and similar angle of incidence (figure 3.11). In the histogram in figure 3.11 it can be seen that the mean NRCS on land is approximately -9 dB for the calibrated nominal TDX acquisition, while for BiDi the mean NRCS on land is -15.2 dB. This again suggests an error in the radiometric calibration of slightly above 6 dB NRCS.

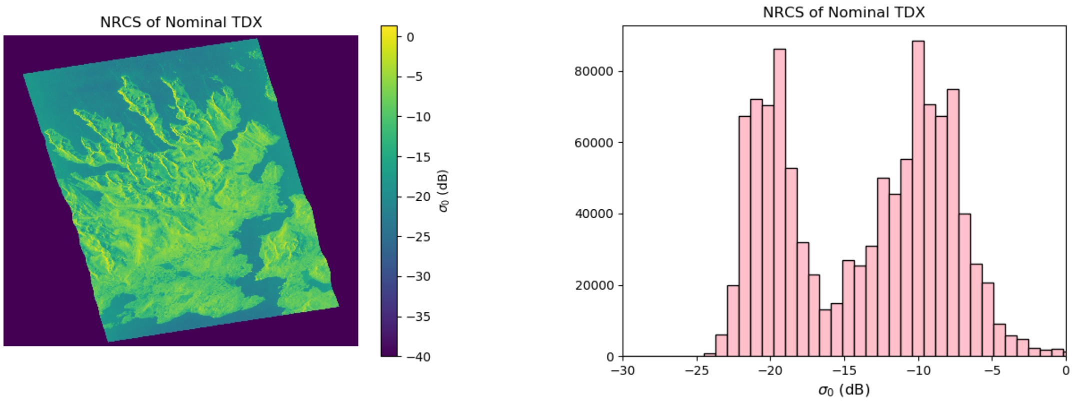

Figure 3.11: On the left the image shows a quicklook of calibrated NRCS with a nominal incidence angle of 23.4°at the Tromsø coast. The right image shows the histogram of NRCS of this area, where the peak on the left of -20 dB is at sea and the peak on the right of -9 dB is on land area. NRCS on land for TDX BiDi is -15.2 dB. Again suggesting a bias between 6 and 7 dB.

A phase offset is calculated by computing a coherence weighted phase average over the land areas selected with the mask. The offsets are listed in table 3.3. The mean phase offset in the aft beam differs 9 degrees with the modal phase offset. This indicates a non Gaussian distribution of phase offsets over the land area. Therefore, correction of the aft beam phase is of less quality introducing phase errors.

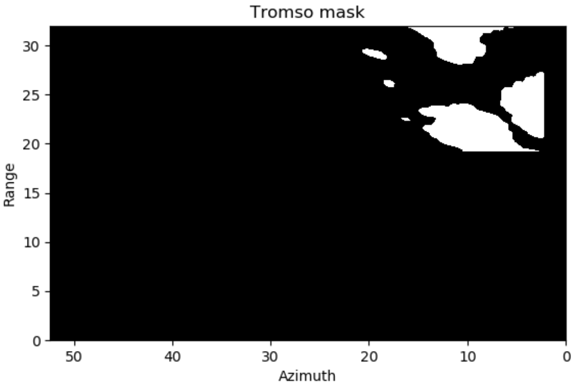

Figure 3.12: Selected land area for phase calibration in Tromsø to avoid layover.

Assume the phase error equals the difference between mean phase offset and the mode of the phase offset. By subtracting these phase offset values from table 3.3 the phase error becomes $\epsilon_{i,fore}$=3.89° for the fore beam and $\epsilon_{i,aft}$=8.89° for the aft beam. The phase error propagates to the radial Doppler velocity with a scaling

$$\epsilon_v = \frac{\lambda \epsilon_i}{\pi \tau}, \tag{3.10}$$

where ϵ_v is the error in the radial Doppler velocity in m/s, ϵ_i the error in estimated phase offset in cycles, λ the radar wavelength in meters and τ the temporal baseline in seconds. The mean error in the radial Doppler velocities then become $\bar{\epsilon}_{v,fore}$ = 0.26 m/s and $\bar{\epsilon}_{v,aft}$ = 0.55 m/s. In along-track and across-track direction the error follows from a scaling with twice the sine of the squint angle and twice the cosine of the squint angle respectively. Resulting error bars due to erroneous phase calibration are then $\epsilon_{\bar{v},at}$ = 10.61 m/s in the along-track direction and $\epsilon_{\bar{v},xt}$ = 0.41 m/s in across-track. The along-track velocity error bar is of an exaggerated proportion. This could explain the large along-track components of the Doppler field seen in figure 6.2 and 6.3.

Table 3.3: Phase offset for Tromsø

Mean phase offsets (fore, aft):	(-83.38, -166.39)
Estimated phase standard deviation (fore, aft):	(0.014, 0.014)
Mean phase offset difference:	83.00
Modal phase offsets (fore, aft):	(-79.49, -157.50)
Modal phase offset difference:	78.01

For Novaya Zemlya L-2 products are shown in figure 3.13. As for Tromsø the NRCS displayed in the intensity images lies again well below the values as expected from the XMOD2 and Kirchhoff approximation models. Values lie between -20 and -5 dB, whereas the model range is from -4 to 6 dB approximately. Histogram plots similar to figure 3.10a and 3.10b can be found in the appendix. Again an offset of 6 to 7 dB with respect to the model values was seen. Therefore, a constant value of 7 dB is added to the NRCS before retrieval.

Mean NRCS on land is -12.77 dB, whereas mean NRCS at sea is -8.97 dB. A difference of 3.74 dB indicates that there is not much phase ambiguity of the sea on land. Phase is not properly flattened. The DEM is not accurate in this region, as ice caps cover the land part of the year. Note also the incoherent area at the bottom part of the land area. This is a point of high elevation and therefore the incoherent area coincides with an icecap.

An attempt to flatten phase over land is made, which decreased the difference between modal and mean phase offset significantly. Phase flattening is conducted by correcting for the DEM height multiplied with the height sensitivity (k_z). Possibly additional errors are introduced with this correction. The difference between modal- and mean phase offsets (tabel 3.4) decreases significantly if residual topographic phase is flattened, improving the phase calibration. A height range between 30 m and 200 m is chosen to define the calibration

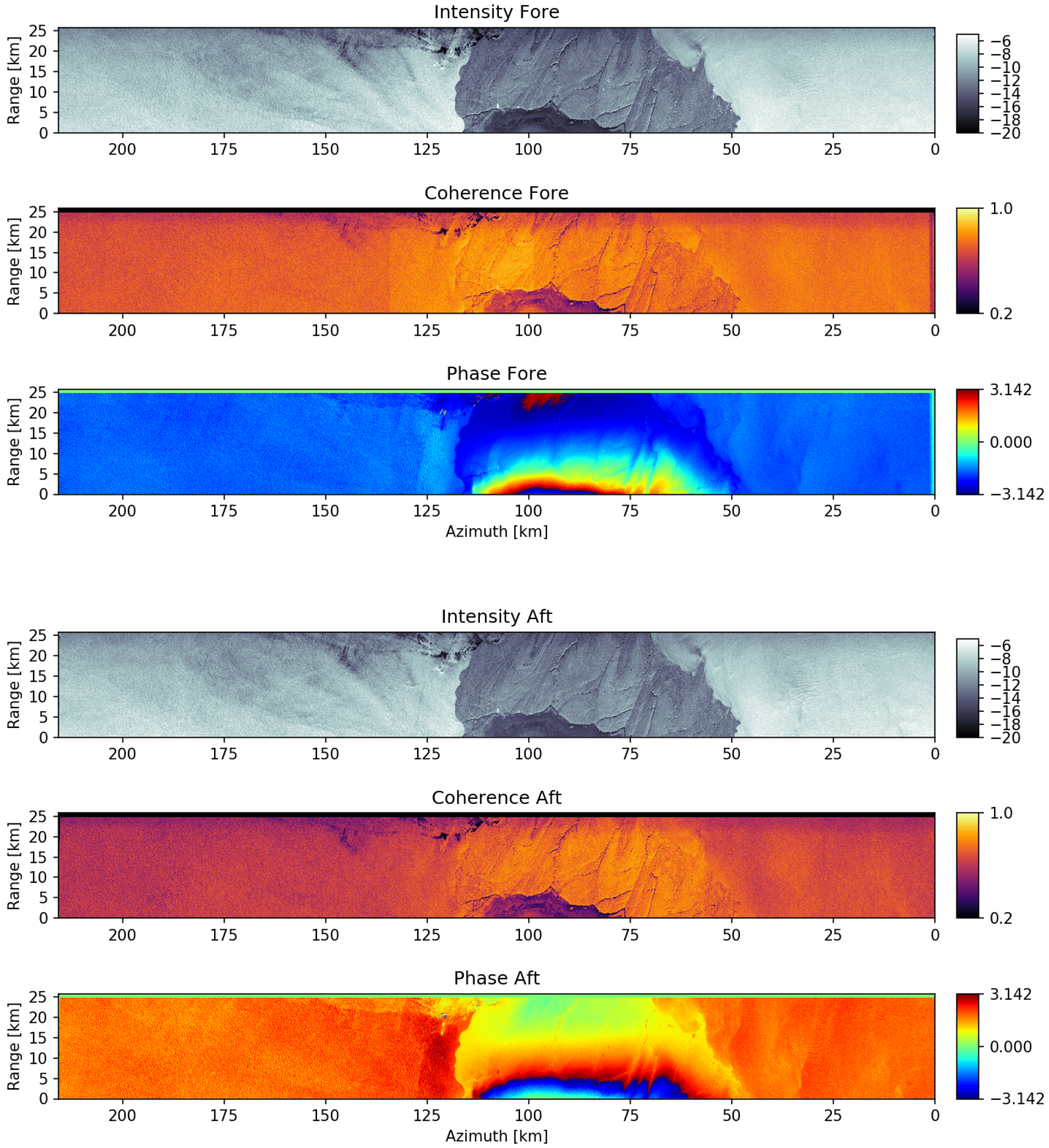

Figure 3.13: Uncorrected L-2 products. The intensity is expressed in NRCS in dB (m^2/m^2). Intensity values are between -12 and -6 dB, which is again much lower than the model range of approximately -4 to 6 dB for an angle of incidence of 17°. Both fore- and aft phase images go through a full phase cycle on land, by attempting additional flattening with the DEM this ramp is removed.

area, far enough from the coast to avoid ambiguities and low elevations to avoid DEM errors due to ice.

Table 3.4: Phase offset for Novaya Zemlya

Mean phase offsets (fore, aft):	(-144.01, 50.76)
Estimated phase standard deviation (fore, aft):	(0.005, 0.006)
Mean phase offset difference:	-194.77
Modal phase offsets (fore, aft):	(-144.50, 50.53)
Modal phase offset difference:	-195.02

Now the data has been calibrated, a calibration procedure has been presented and it is well understood what the origin of data errors could be. The best external data source for reference data for the two locations is found to be the ECMWF ERA-5 atmospheric model and a workflow for comparing these data with the vector field as derived from TanDEM-X data has been presented in this chapter. In the next chapter the theoretical background and understanding of TanDEM-X ATI data are used for the methodology for the retrieval of winds- and TSCV.

4

Methodology

In this chapter the proposed methodology is presented. An overview is given of the retrieval scheme. Equations for the algorithm are presented and necessary constraints are given.

4.1. Overview

Figure 4.1 illustrates the retrieval process in a flow chart. Steps inside the striped line are part of the retrieval process, rest are inputs and outputs. The process can be separated in pre-processing steps, look-up tables, wind retrieval and total surface current retrieval.

Inputs

Retrieval of the wind vector and the TSCV relies on the use of two observables (amplitude and phase) in two directions. These are contained in the L-2 products that are the output of the experimental SAR processor (TAXI). These L-2 products are the start input of scheme that leads to a TSCV. An external data source is required to constrain the solution of wind direction, therefore requiring an additional input.

Look-up table

The Doppler GMF and NRCS GMF are given as a *look-up table* to the retrieval algorithm. The look-up table is generated by evaluating the Kirchhoff Approximation and XMOD2 geophysical model function presented in chapter 2.4.1 on a grid as a function of wind speed magnitude in axis 0 and wind direction in axis 1 and angle of incidence in axis 2. A look-up table resolution of $dU_{10} = 0.1$ m/s, $d\phi = 1°$ and $d\theta = 0.1°$ was used. The choice of these values is based on the approximate accuracy of reference data. Wind vectors are usually not better estimated than 0.1 m/s for magnitude and 1° for direction is even optimistic [36]. Figure 4.3 shows the look-up tables for an angle of incidence of 20° for the NRCS- and Doppler GMF.

Pre-processing steps

There are some steps concerned with preparing the data for retrieval:

- multilook;
- NRCS calibration;
- phase calibration;
- retrieve Doppler vectors.

A discription of the calibration steps is given in section 3.3.1. Multilooking is described in section 3.1.1. Section 2.2.2 gives the derivation of along-track and across-track Doppler velocity components for the BiDi geometry from the interferometric phase.

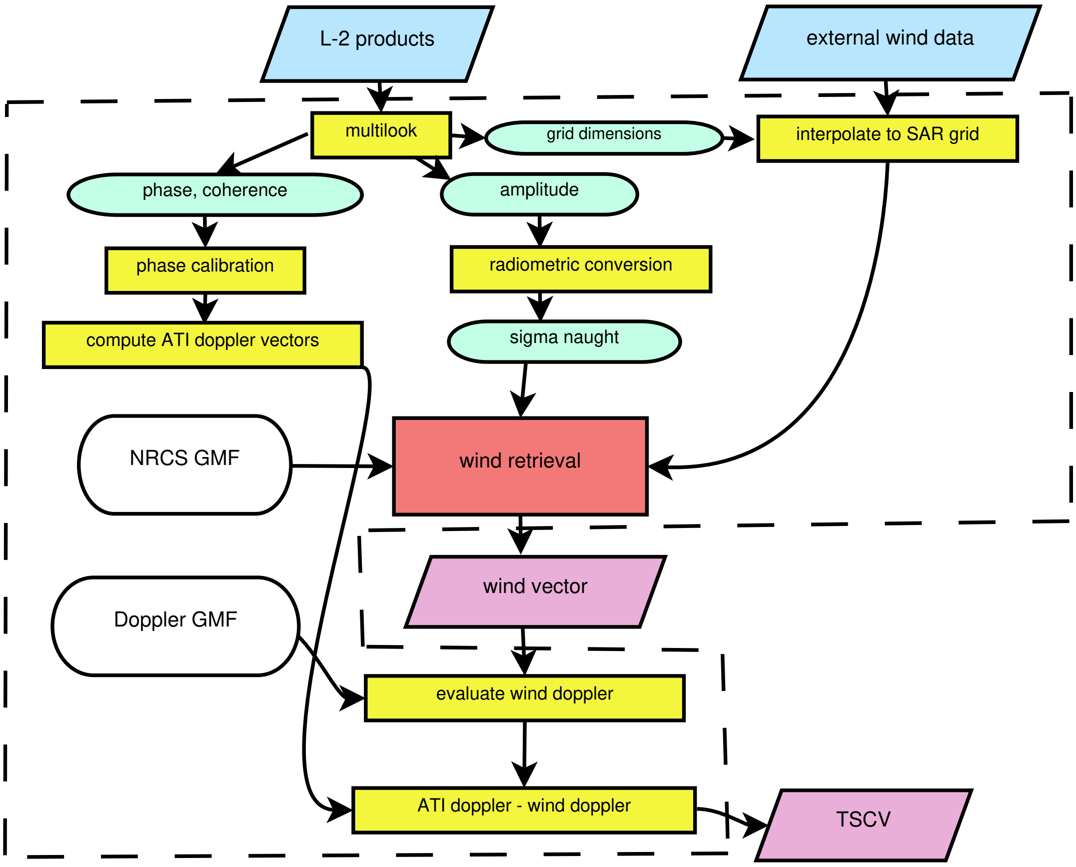

Figure 4.1: Flow chart of pre-processing and wind- and Total Surface Current Vector algorithm. Blue indicates inputs, purple outputs, white look-up tables, green intermediate data products, yellow operations and red is a regression. Inputs to the retrieval algorithm are BiDi ATI L-2 amplitude and phase data. These data need some operations before they can be used in the retrieval algorithm. After these operations, wind vectors are retrieved. Wind vectors are used to retrieve TSCV with the ATI Doppler field and the GMF for Doppler Centroid.

Retrieval

Wind retrieval is based on the minimization of a cost function. The cost function is a function of two NRCS observables, a look-up table of the GMF and external wind data. Output of the wind retrieval algorithm is a solution for the wind vector field. Sign convention of the ATI Doppler vector and wind vector can be found in figure 4.2. With an estimation of the wind vector, the Doppler GMF will be evaluated to estimate a Doppler wind component. As last, subtraction of the Doppler wind component from the ATI Doppler vectors gives an estimation for TSCV.

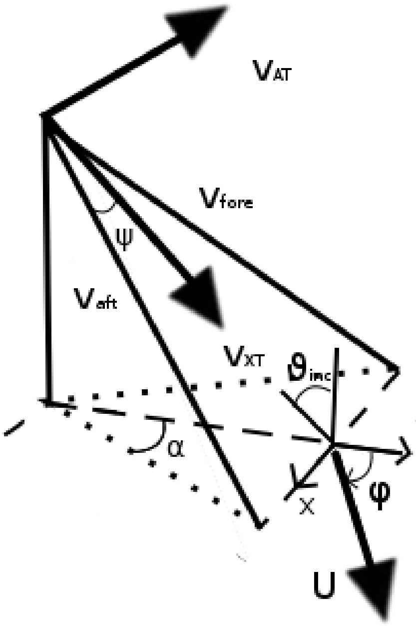

Figure 4.2: Geometry and sign convention of the ATI Doppler vectors and wind vector used in this methodology. v_{fore} is the ATI Doppler velocity in LoS of the fore beam. v_{aft} is the ATI Doppler velocity of the aft beam. The across-track Doppler (v_{XT}) is in nominal Line of Sight, whereas the along-track Doppler (v_{AT}) is in the orbit direction. Wind vector is expressed in polar coordinates (U and ϕ) with the origin in the observation point. Direction of ϕ is taken positive clock-wise, similar to the direction of the external wind data. ψ is the antenna squint angle. α is the projection of the antenna squint on ground. θ_{inc} is the angle of incidence.

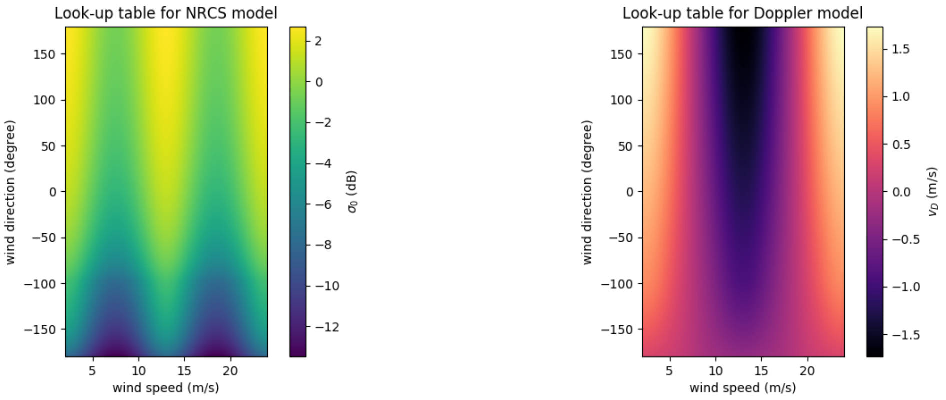

Figure 4.3: Interpolated look-up table grids for the Kirchhoff Approximation. On the left a look-up table for the NRCS model and on the right a look-up table for the Doppler model. Angle of incidence is 20°. The look-up tables were interpolated to spacing $dU_{10}, d\phi, d\theta$.

4.2. Wind retrieval algorithm

In this section equations are provided for the wind retrieval algorithm. The wind retrieval method minimizes the squared difference between an observation and values given in the look-up table. This regression method allows us to use multiple models for retrieval, such as retrieval of the wind vector from Doppler data and the use of different GMF's.

4.2.1. Cost function for NRCS observations

A cost function is defined, which is the squared difference between a SAR observation and the model values. The cost function for wind retrieval can be written as

$$J_{\sigma_0}(U_{10},\phi) = \frac{(\sigma_{0,fore} - \bar{X}(U_{10},\phi - \Delta\phi))^2}{Var(\sigma_{0,fore})} + \frac{(\sigma_{0,aft} - \bar{X}(U_{10},\phi + \Delta\phi))^2}{Var(\sigma_{0,aft})} + \frac{(\phi_{ext} - \bar{D})^2}{W_{ext}}, \tag{4.1}$$

where U_{10} is the wind speed parameter in m/s, ϕ the wind direction parameter relative to across-track look, σ_0 the normalized radar cross section observation, $\bar{X}$ the look-up table of a GMF for NRCS (see section 2.4.3), $\Delta\phi$ the squint angle of the beams on ground, ϕ_{ext} the wind direction observation from external data source, $\bar{D}$ a matrix of the dimensions of the look-up table filled with wind directions corresponding to those in the model and W_{ext} is a tuned weight for this term.

Weight of the external data term is tuned by trial and error. Weights are tuned such that

$$k_w \cdot \theta_{nom} \ll \frac{mean(\sigma_0)}{Var(\sigma_0)}, \tag{4.2}$$

where k_w is a weight tuning factor, θ_{nom} the nominal angle of incidence σ_0 are all NRCS observations of tuning data set. Nominal angle of incidence is chosen as a factor in weight tuning, because of the incidence angle dependency of σ_0. k_w results to 50000 with these data. For this value no ambiguities in wind direction are seen in images (see also appendix figure A.8b). This makes $k_w \cdot \theta_{nom}$ 4 orders of magnitude smaller than $\frac{mean(\sigma_0)}{Var(\sigma_0)}$, therefore giving very little weight to the external data source and merely using it as a constraint.

4.2.2. Cost function for Doppler velocity observations

Wind retrieval from ATI Doppler observations is not done for the purpose of actual wind retrieval, but as a test for the models. This method is used in the simulations study (chapter 5) and as a sanity check on the model (figure 6.13). This function does not use external data and the cost function is defined as follows:

$$J_{v_{ati}}(U_{10},\phi) = \frac{(v_{ati,fore,i} - \bar{V}(U_{10},\phi + \Delta\phi))^2}{Var(v_{ati,fore})} + \frac{(v_{ati,aft,i} - \bar{V}(U_{10},\phi - \Delta\phi))^2}{Var(v_{ati,aft})}, \tag{4.3}$$

where $v_{ati,i}$ is the doppler ATI velocity in pixel i and $\bar{V}$ the look-up table of a GMF for Doppler Centroid velocity (see section 2.4.2).

When the cost functions are minimized, one obtains an estimation of wind speed magnitude U_{10} and wind direction ϕ. Figure 4.4 illustrates how the minimum is found in 3D of $\bar{J}_{v_r}(U_{10},\phi)$ (equation 4.3). Note that this is a surface plot with the shape of figure 2.6 and 2.7. For the cost function for backscatter (eq.4.1) a shape similar to 2.9 and 2.10 would be seen.

Output of this process is the wind vector:

$$\begin{bmatrix} \hat{U}_{10} \\ \hat{\phi} \end{bmatrix}.$$

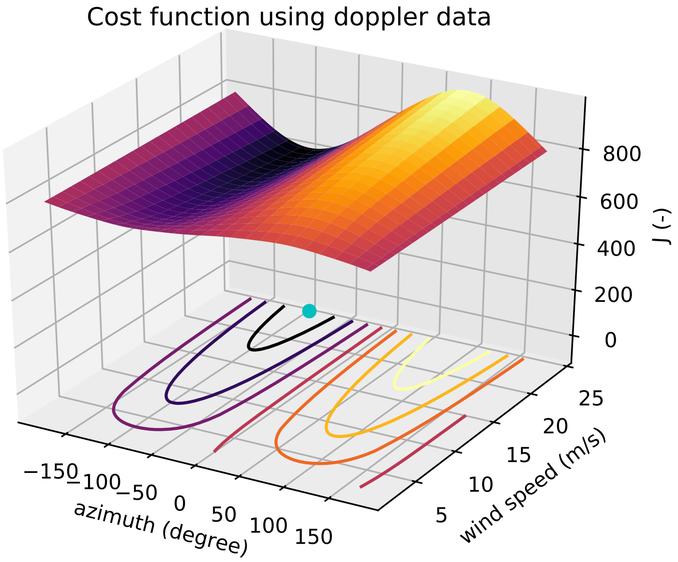

Figure 4.4: This figure shows a 3d illustration of the cost function that was calculated for a pixel. The blue dot shows the location of the minimum of the cost function in 2D. Coordinates of this point (wind speed and azimuth) give the values of wind speed and wind direction.

4.3. Retrieval of Total Surface Current Vector

After inversion of the wind vector, wave geophysical bias is then obtained by evaluating same GMF for Doppler Centroid. The along-track and across-track components are obtained using equations 2.8 and 2.9. For the wave bias the along-track and across-track components become

$$v_{w,AT} = \frac{\bar{V}(\hat{U}_{10}, \hat{\phi} - \Delta\phi) - \bar{V}(\hat{U}_{10}, \hat{\phi} + \Delta\phi)}{2sin(\psi)} \tag{4.4}$$

and

$$v_{w,XT} = \frac{\bar{V}(\hat{U}_{10}, \hat{\phi} - \Delta\phi) + \bar{V}(\hat{U}_{10}, \hat{\phi} + \Delta\phi)}{2cos(\psi)}, \tag{4.5}$$

where $v_{w,AT}$ is the wave geophysical bias in along-track direction, $v_{w,XT}$ the wave geophysical bias in nominal radar Line of Sight direction, ψ the radar squint angle (degrees) and $\Delta\phi$ is the squint angle on ground (degrees).

Note that for an across-track component of TSCV similarly to the wind vector (see also figure 4.2), one needs to multiply $TSCV_{XT}$ with the sine of the incidence angle. The Total Surface Current Vector then simply follows from the subtraction of wave geophysical bias from ATI Doppler vector (as computed with the equations in section 2.2.2)

$$TSCV_{AT} = v_{at} - v_{w,AT}, \tag{4.6}$$

$$TSCV_{XT} = v_{xt} - v_{w,XT}, \tag{4.7}$$

where $TSCV_{AT}$ is the along-track component of TSCV, $TSCV_{XT}$ the across-track component, v_{at} the along-track Doppler velocity, v_{xt} the across-track Doppler velocity, $v_{w,AT}$ the along-track wave geophysical bias and $v_{w,XT}$ the across-track wave geophysical bias. Units of all velocity components are meters per second.

Retrieval of the TSCV is the last step of all in this study. With the method presented in this chapter a wind field can be retrieved from calibrated BiDi intensity images and with an estimation of the local winds, the wave bias to the Doppler field is estimated. As last the TSCV is retrieved by a subtraction of the wave bias from the Doppler vectors. The next chapter applies the wind retrieval algorithm to simulated data to test the algorithm and study its sensitivity.

5

Simulations

The wind retrieval algorithm was tested on simulated data before it could be used on real data. In this chapter first the used simulation scheme is presented, the simulated data is then graphically presented and finally the simulation results lead to conclusions on the wind retrieval algorithm.

5.1. Simulation scheme

A simulator is developed to test the inversion algorithm. The simulation process is shown in figure 5.1. The inversion algorithm is first tested on the deterministic simulated data as a model check, then a sensitivity study is conducted by means of adding simulated noise to the deterministic signal. There are three parameters one can experiment with in these simulations, the generated wind speed and direction and the noise. Errors are seen to be highly dependent on all input parameters(see also figure 5.6,5.6b, 5.6a, 5.5a and 5.5b). Wind vector estimation errors do not exceed the grid cell size of the look-up tables, 0.1 m/s for wind speed and 1° for wind direction. Implying that the proposed inversion algorithm solves exactly, upto the resolution of the look-uptable.

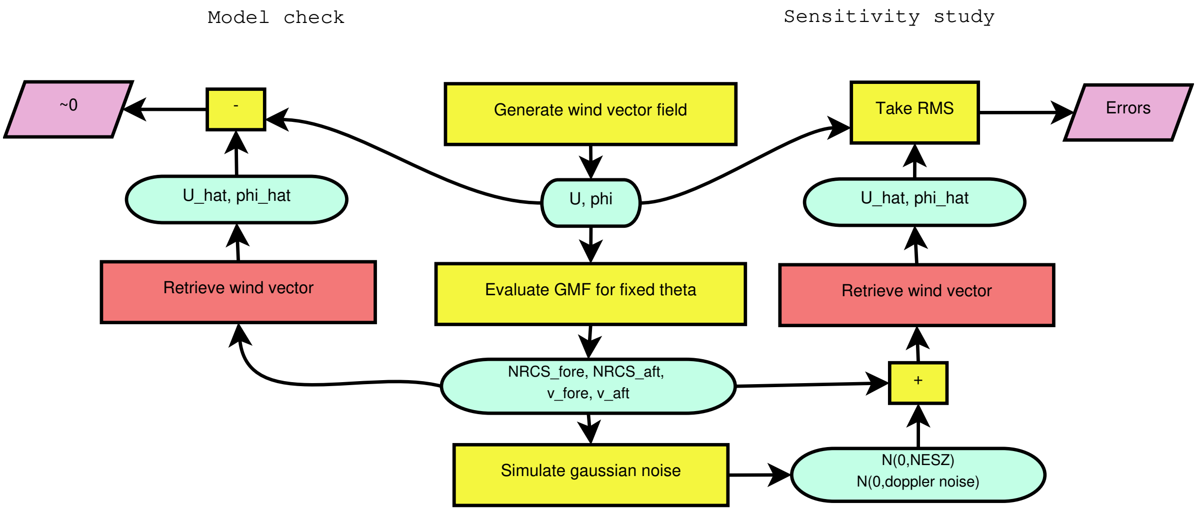

Figure 5.1: Scheme of the simulations conducted to check the retrieval algorithm and to test its sensitivity. For the model check deterministic data is generated, whereas for the sensitivity study noise is added to the deterministic data. Blue indicates inputs and outputs, green (intermediate) data products, yellow operations and red is a regression.

Figure 5.3 shows the deterministic plus stochastic simulated signal for backscatter for the fore- and aft beam. Figure 5.4 shows the deterministic plus stochastic simulated signal for Doppler in the fore- and aft beam.

5.2. Simulated data

In this section some examples of a simulated data scene are presented. Figure 5.2 shows a wind field that is varied over a range of directions and magnitudes. Figure 5.3 shows the XMOD2 forward modeled σ_0 with a noise component added. One observes the slight difference in σ_0 between fore- and aft beam. In figure 5.4 the Doppler velocity as a consequence of wind is modeled by means of giving the wind field as an input to the Kirchhoff approximation with a noise component added. The added noise component is arbitrarily defined, but the images illustrate the ambiguous behaviour of the solution for the wind vector well.

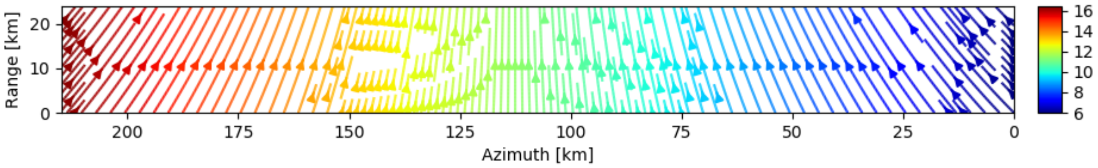

Figure 5.2: Simulated wind field as a vector plot. The wind direction varies from 45°to -45°and the wind speed varies from 6 to 16.5 m/s. This wind field was used to test the retrieval algorithm and to check noise sensitivity by adding a noise component to the forward modeled NRCS with this wind field as an input.

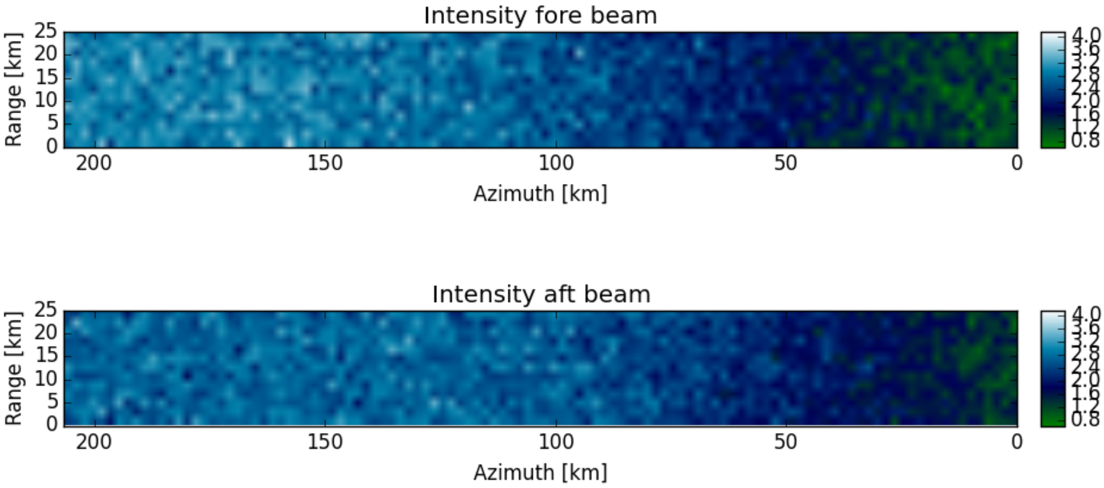

Figure 5.3: σ_0 for the simulated wind field with normally distributed random noise, using $\sigma_{\sigma_0} = 0.2$ with wind vectors 5.2 as input for the deterministic signal. The angle of incidence is 17°. The unit is area/area.

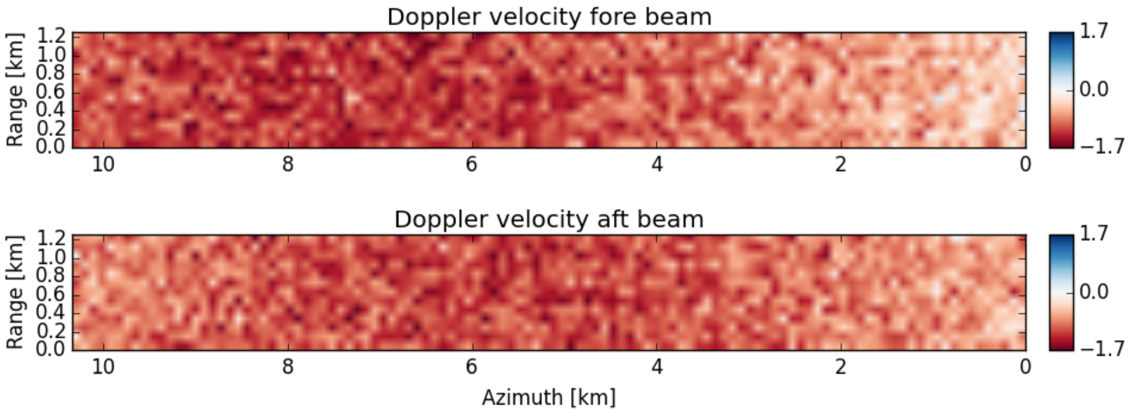

Figure 5.4: v_D for the simulated wind field with normally distributed random noise, using $\sigma_{v_D} = 0.2$. with wind vectors 5.2 as input for the deterministic signal. The angle of incidence is 17°. The unit is m/s.

5.3. Simulation results and error analysis

Running the inversion algorithm on noisy simulations, certain weaknesses appear. The simulations presented in figures 5.2 till 5.4 are used to invert wind speed and wind direction to produce the histograms in figures 5.5a and 5.5b. These histograms contain estimation errors from the whole range of wind speeds 6 to 16 m/s and wind directions varying from cross-wind to down-wind.

Figure 5.5a represents a histogram of the estimation error of wind speed magnitude. The purple histogram displats errors when wind speed is retrieved from doppler data using the cost function defined in eq. 4.3. The green histogram represents estimation errors when wind speed is retrieved from backscatter data using the cost function defined in eq. 4.1. It can be observed from the retrieval statistics in figure 5.5a that the backscatter appears to be more robust for estimation of the wind speed mangitude. However, this may be a consequence of lower SNR of the Doppler simulations w.r.t. NRCS simulations. SNR of NRCS simulations is approximately 9 dB, while the SNR of the Doppler simulations lies around 4 dB.

Wind direction error distribution demonstrates in figure 5.5b that the wind direction is better estimated using Doppler data, eventhough SNR is lower on the Doppler data. This is a consequence of the Doppler GMF, that has two solutions for each value of a Doppler observation (see figure 2.6), whereas the backscatter GMF (figure 2.9) there are four wind direction solutions for each value of σ_0.

It's likely that in many cases of wind retrieval from backscatter observations, one of the incorrect 3 solutions is estimated. If one of the incorrect solutions is taken from the GMF, chances are high also an incorrect estimation of wind speed magnitude is retrieved.

The retrieval function needs a diversity of observation values that is large enough to invert to the correct solution for wind direction. This implies that the following statement needs to be satisfied:

$$\sigma_{0,fore} - \sigma_{0,aft} > GMF(U,\phi-\psi) - GMF(U,\phi+\psi)$$

For a wind speed of 13 m/s and a wind direction of -50 degrees, the difference between XMOD2 evaluated for the fore beam and the aft beam is only -17 dB. Errors may not exceed this value.

$$(\sigma_{0,fore} \pm \epsilon_{\sigma_0}) - (\sigma_{0,aft} \pm \epsilon_{\sigma_0}) < GMF(U,\phi-\psi) - GMF(U,\phi+\psi)$$

$$\epsilon_{\sigma_0} < \frac{GMF(U,\phi-\psi) - GMF(U,\phi+\psi)}{2}$$

For the difference of -17 dB at a wind speed of 13 m/s and 50 degrees wind direction angle the following holds:

$$\frac{GMF(U,\phi-\psi) - GMF(U,\phi+\psi)}{2} = -19$$

The NESZ of Bidirectional SAR lies around -17 dB. Noise will always be larger than the required accuracy for estimation of the wind direction. Therefore it can be concluded that diversity between BiDi NRCS observations will not be enough to find a solution for wind direction.

For other values of wind speed and wind direction, the required accuracy will even be larger. This can be seen in figure 2.9. For low wind speeds and around up-wind and down-wind direction, the function is less steep. A squint angle of approximately 8° will then result in a smaller diversity of fore- and aft beam NRCS.

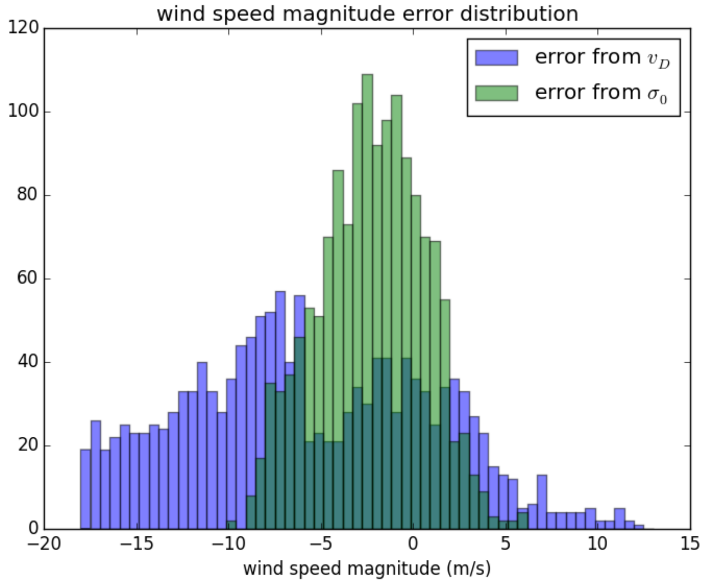

(a) Histogram of the estimation errors of wind speed magnitude

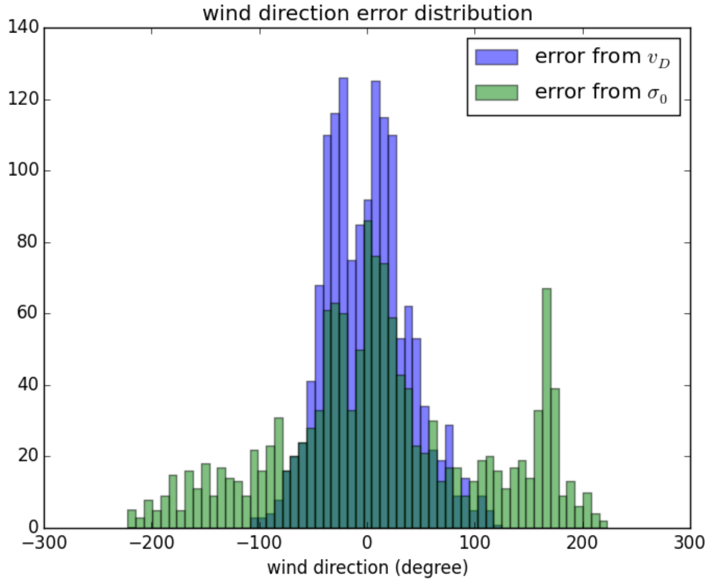

(b) Histogram of the estimation errors of wind direction

Figure 5.5: Biased wind retrieval statistics from simulated Doppler data (figure 5.4) in purple and from simulated NRCS data (figure 5.3) in green. The simulated data contains random normally distributed noise, with a standard deviation of 0.2. SNR of NRCS simulations lies around 9 dB, SNR of Doppler simulations is approximately 4 dB. Even with lower SNR wind direction retrieval is less ambiguous when using Doppler data than NRCS data.

Same simulation scheme with a constrain on the solution for wind direction is applied to 100 samples for different noise levels. Noise is varied from -17 dB (≈ NESZ) up to the value of the deterministic signal (where SNR=0). This noise component is added to the signal as a normally distributed random variable with $N(0, \sigma_{NRCS})$. The signal is computed with the XMOD2 forward model for a given wind strength and wind direction and angle of incidence 22°. RMS is then calculated as:

$$RMS_U = \sqrt{\frac{\sum_{i=1}^{100} \hat{U}_i - U}{100}}$$

Figure 5.6 depicts the Root Mean Square Error ratio with wind strength retrieved at different wind speeds. With the constraint on wind direction, wind direction RMS is around 0.

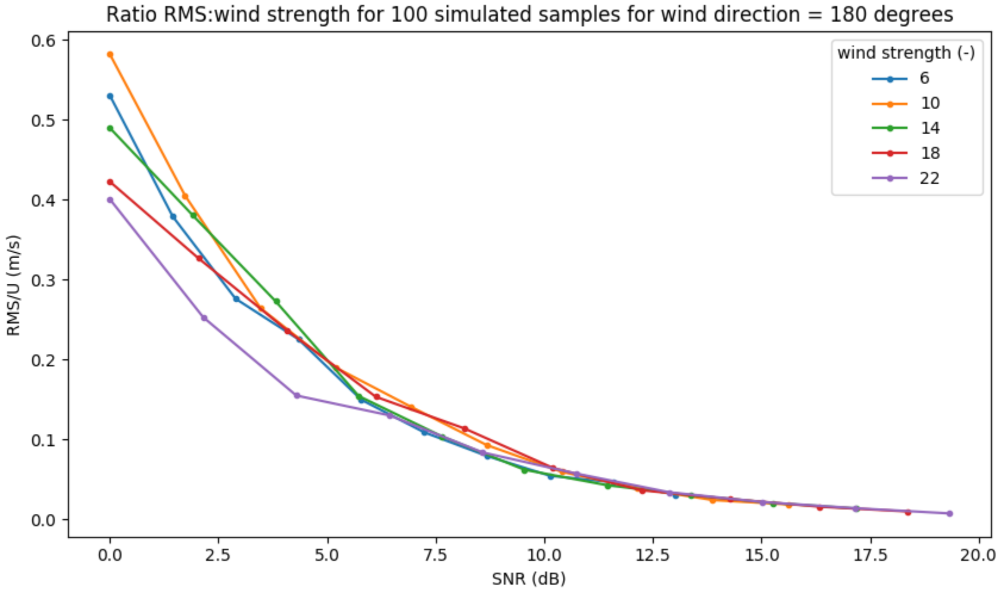

(a) Up-wind

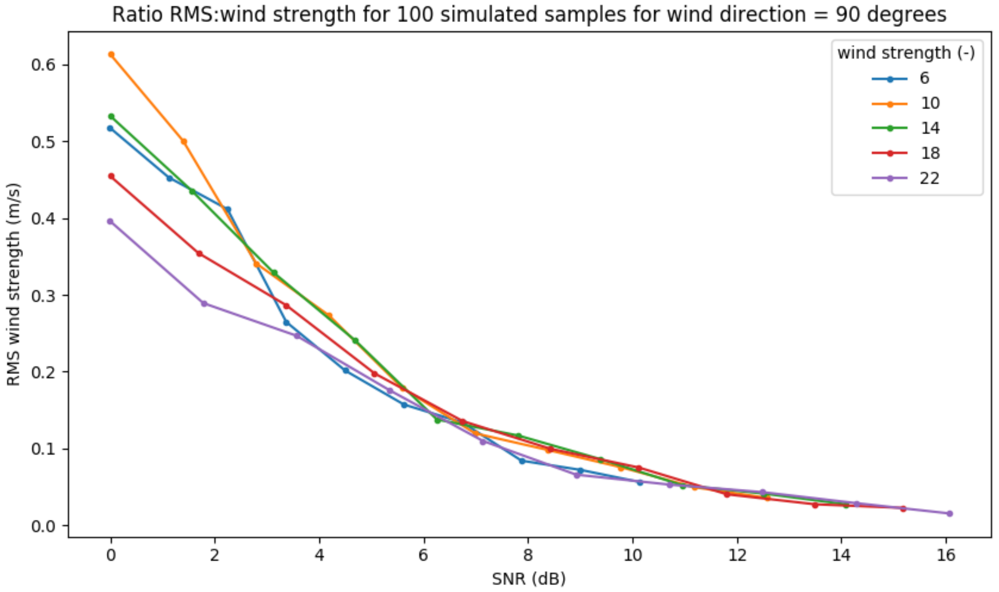

(b) Cross-wind

Figure 5.6: Root Mean Square Error of 100 simulated samples ratio with input wind speed for different values of wind strength as a function of Signal to Noise Ratio. Higher wind speeds have a lower ratio RMS:wind strength. This proves that wind retrieval is less error prone for higher wind speed values.

From the simulations we have learnt that wind direction is not easily estimated using Bidirectional SAR.

Squints are too small to guarantee sufficient diversity of observations. Incorrectly estimated wind direction, will lead to errors in estimation of the wind speed magnitude. By simulating a varying amount of noise and computing the RMS of 100 simulated samples we see that root mean square error of wind speed magnitude decreases as a function of SNR. High wind speed has lower RMS than weak winds. The addition of a constraint on wind direction has succesfully reduced wind direction errors to nearly zero. In the next chapter the algorithm is applied to real TanDEM-X data, the data presented in chapter 3.

6

Results

In this chapter Doppler field, wind field and TSCV are retrieved from the L-2 products that were corrected and presented in section 3.4. The Doppler velocity field is computed and presented with error calculations. Wind field as follows from ECMWF ERA-5 and wind retrieval results are presented and compared. Lastly a TSCV field is shown and its quality is analyzed.

6.1. Retrieval results of Tromsø

Results of pre-processing of Tromsø (section 3.4) are the calibrated amplitude and phase in figure 6.1. To obtain these images a correction of 6 dB had to be applied to the intensity and the phase has been corrected with a calculated offset. NRCS lies within the range of GMF values and average phase is around zero on areas used for calibration. The phase image shows some layover areas on land on the right of the image. The intensity image has only a mean difference of 0.81 dB between values on land and at sea, which is an indicator of phase ambiguities on the land. Low wind speeds coincide with the black areas in the intensity image.

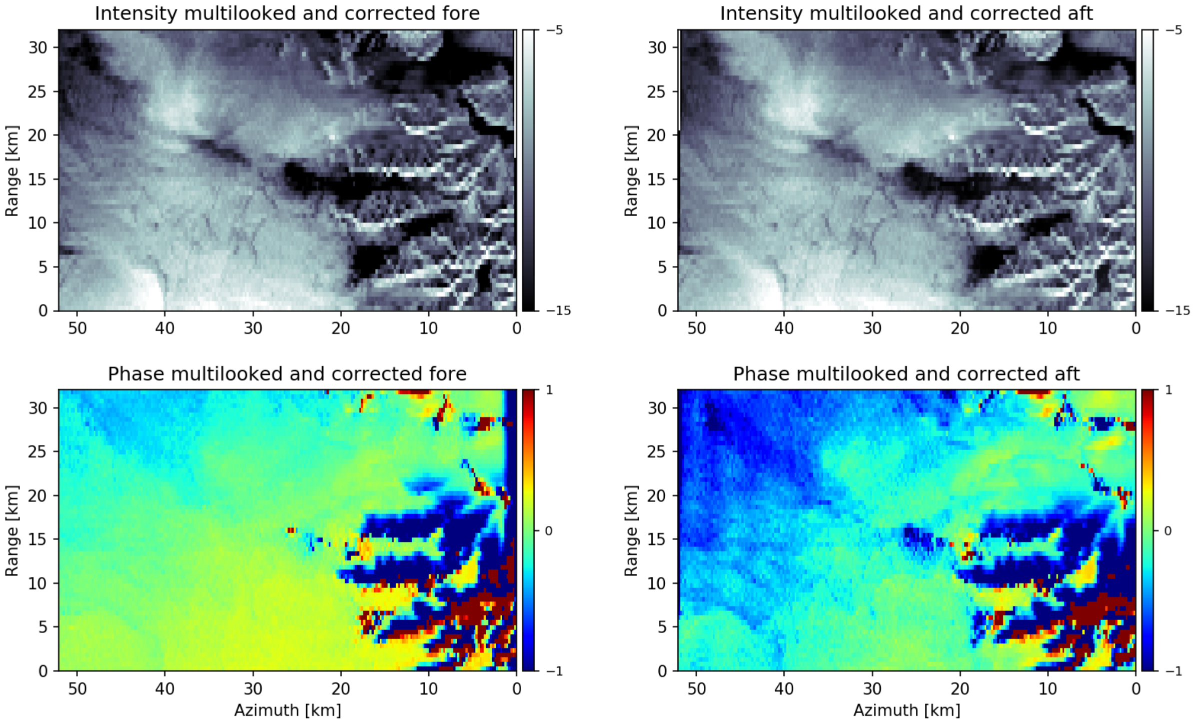

Figure 6.1: Corrected and multilooked NRCS and phase. The intensity is expressed in NRCS in dB (m^2/m^2). Resolution is 233.6 x 204.6 m. The NRCS values now lie within the range of the geophysical model function. Phase is around zero on the areas used for calibration, which can be found in figure 3.12. The dark blue and red areas on land in the phase image correspond with layover effects. The black areas in the intensity image coincide with low wind speed areas.

6.1.1. Doppler velocity

The corrected phases in figure 6.1 are projected to the ocean's surface and the Doppler velocity is computed (figure 6.2). Tis is the total velocity of the ocean surface, including the wind waves, swell waves and currents. The Dopper along-track component displays modulation with a wavelength of approximately 4 km in horizontal direction. These modulations can be assosciated with very large swell waves and do therefore not correctly represent current or wind induced motion of the surface. To obtain a current, these modulations need to be filtered by means of smoothing with a window as long as the modulation. The along-track Dopper component is of an order of magnitude stronger than the across-track component. This strong along-track component is the result of phase calibration issues. When the Doppler field will be used to compute TSCV the erroneous along-track component can dominate the result.

A diagonal front in the along-track Doppler component is an unknown geophysical signature, that could possibly be of atmospheric origin. There are also large variations in intensity here, which also suggests an atmospheric signal. However, in the ECMWF model no such thing is seen, due to lack of spatial resolution. Figure 6.3 shows the Doppler field with a resolution of 4 km. By using multilooking as a filter, the swell waves have disappeared in this image. A strong along-track component is seen that may be a consequence of calibration errors. In the magnitude of the vector field again the same diagonal front is seen.

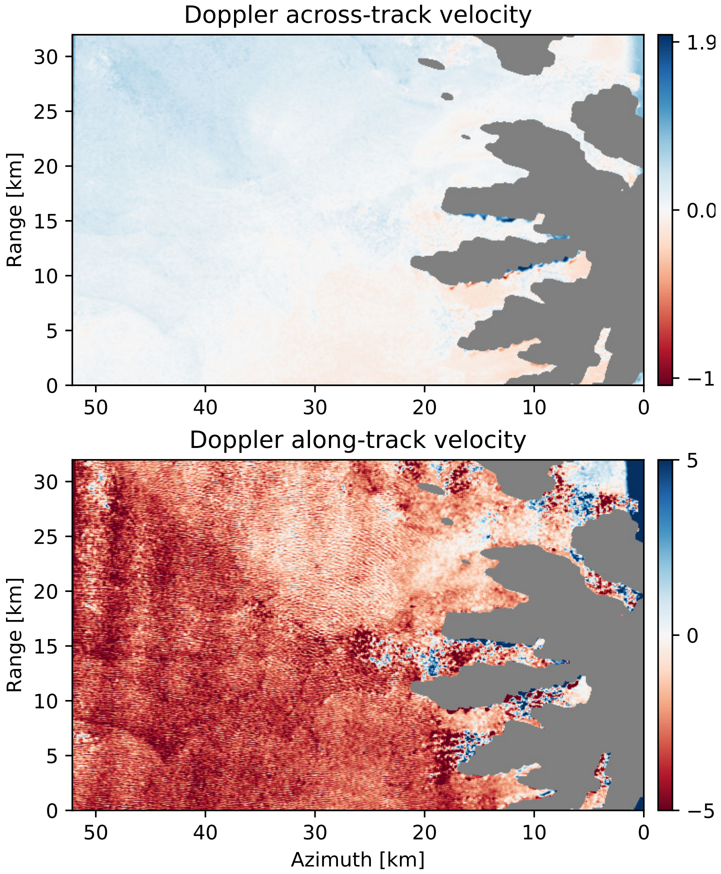

Figure 6.2: Doppler velocity vector components. The Doppler vectors have an along-track component of an order of magnitude stronger than the across-track component, which will later dominate the result for TSCV. Vertical modulations in the along-track component are most likely very long waves. Diagonal signature in along-track component is of undefined geophysical origin.

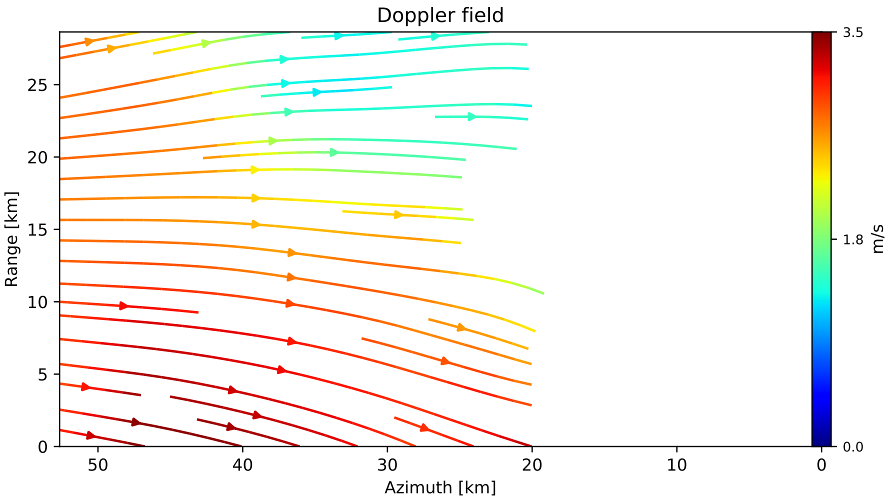

Figure 6.3: Doppler field of figure 6.2 after multilooking with a window of 4 km. There are no more swell waves. Currents below the diagonal are of very high magnitude which is the same signature as seen in 6.2.

6.1.2. Wind

In this section results of wind retrieval are presented and the ECMWF ERA-5 interpolated wind field is shown. To validate the results, the two are compared. The wind direction from ECMWF in figure 6.4 is used to constrain the solution for the wind vector.

NRCS calibration offset correction could introduce a bias between 0 and 1 dB in σ_0 as derived from figure 3.10b. By retrieving the wind vector for the average backscatter plus the bias and minus the bias $\bar{\sigma_0} + \sigma_{bias}/2$ and $\bar{\sigma_0} + \sigma_{bias}/2$. Difference between the solutions for these values of σ_0 will give an estimate for the propagation of NRCS calibration bias to wind Doppler. We obtain an average error for the wind Doppler radial velocity of 0.1 m/s, wind speed magnitude 0.7 m/s and wind direction 2°. This uncertainty on the correction causes an error bar in the wind geophysical bias along-track component of 2.9 m/s and an error bar for the across-track component of 0.1 m/s.

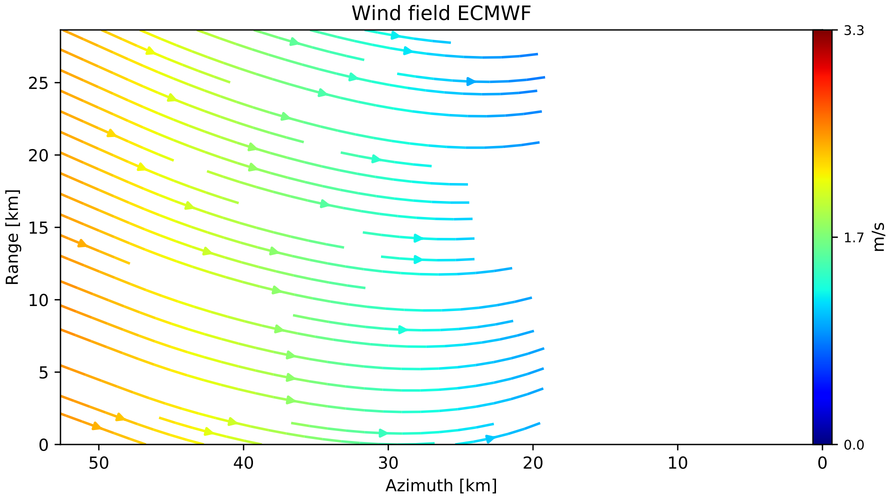

Figure 6.4: This plot shows the wind vector field over the coast near Tromsø from the ECMWF ERA-5 Reanalysis model, interpolated as described in the Data chapter, for the same acquisition time as the BiDi data take of September 4th. This data has an ensemble standard deviation of approximately 0.4 m/s for wind speed magnitude and 33° for wind direction. Mean wind speed is 2.1 m/s, mean wind direction is 89°. One can clearly see in the image that it is a linear interpolation spatially sparse data points.

It is seen that with a sufficiently low weight on the external data term, the solution for wind direction becomes unbiased and only follows the wind direction of ECMWF in a global sense. This is clearly seen by comparing figure 6.4 to figure 6.5. The wind fields have similar values for wind speed, stronger winds are further away from the coast and weaker winds at the coast. The wind stream lines curl up for both figures.

ECMWF does not capture local instantaenous events well, as it is an average spatially (low resolution) and temporally (ensemble mean). The retrieved wind in figure 6.5 displays a dark red patch of high winds that are an instantaneous event of high wind speeds. These make the average of the retrieved wind higher. Considering this in addition to the model uncertainty of ECMWF of 0.4 m/s and the errors in the retrieval results originating from the data of 0.7 m/s, the value of 2.9 m/s of retrieved winds and 2.1 m/s of ECMWF are not far off. The direction of the wind is slightly more upward for the retrieved winds, but the difference of 11° between ECMWF- and retrieved direction is less than the accuracy of ECMWF itself (33°).

The uncertainty of the GMF is assessed by using the Kirchhoff Approximation to estimate the wind field. Figure 6.6 shows the vector field of retrieved winds for Tromsø using the Kirchhoff Approximation model instead of XMOD2 in the retrieval algorithm. The mean estimated wind speed magnitude is 4.7 m/s and the mean estimated wind direction is 66°. It was already shown in chapter 2.4.1 that the Kirchhoff approximation estimates the NRCS higher than XMOD2 does. The disagreement of the models leads to a 2.2 m/s mean difference in estimation of the wind strength with XMOD2 and with the Kirchhoff approximation for Tromsø.

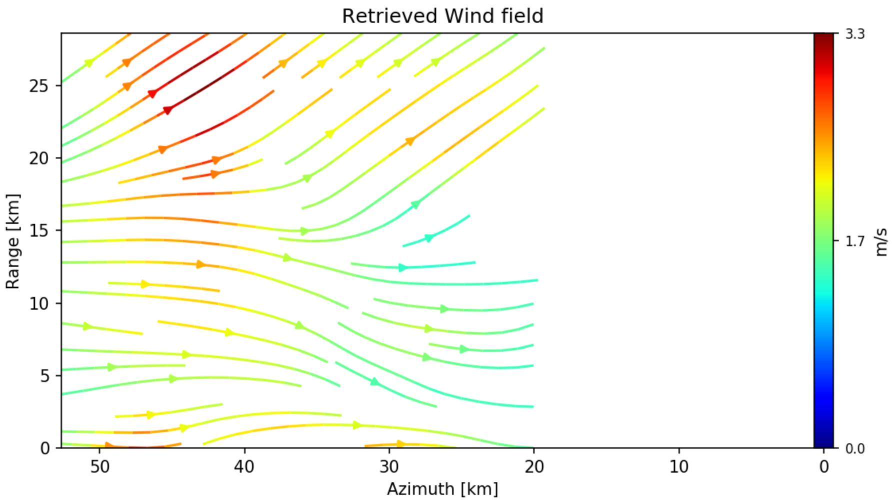

Figure 6.5: Retrieved wind field Tromsø . Mean wind speed is 2.9 m/s, mean wind direction is 78° . The wind speed has an accuracy of 0.7 m/s and wind direction of 2° as a consequence of errors from the data, but there are more unknown errors that originate from the used models.

This also means that the retrieved winds with KA are far off the wind data values of ECMWF.

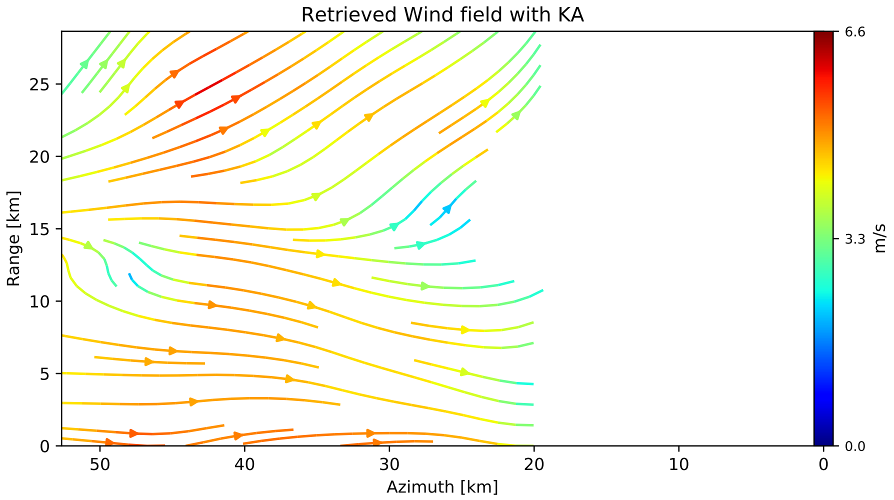

Figure 6.6: This plot shows the retrieved wind field for Tromsø using the Kirchhoff Approximation model. The mean wind speed magnitude is 4.7 m/s and the mean wind direction is 66°. This estimation of the wind vector disagrees with the wind data of ECMWF (figure 6.4).

The Doppler velocity calculated with the retrieved wind and GMF for Doppler Centroid is expected to relate to the wind linearly with

$$V_{D,wind} = k \cdot U, \tag{6.1}$$

where v_D is the Doppler wave bias in m/s, factor k is found to lie around 0.1 and U is the wind speed in m/s. This factor arises from the geophysical model function. How large it should be is still a topic of research. A correlation graph of the relation wave Doppler to wind velocity (figure 6.7) was generated by subtracting the mean from wind data and wave Doppler. The across-track component of the wind Doppler was multiplied with $\sin\theta_{nom}$ to project to the sea surface. The along-track component has a coefficient different to the across-track component. This is a result of estimation errors when the along-track and across-track component are computed and due to errors from the scaling with the nominal incidence angle.

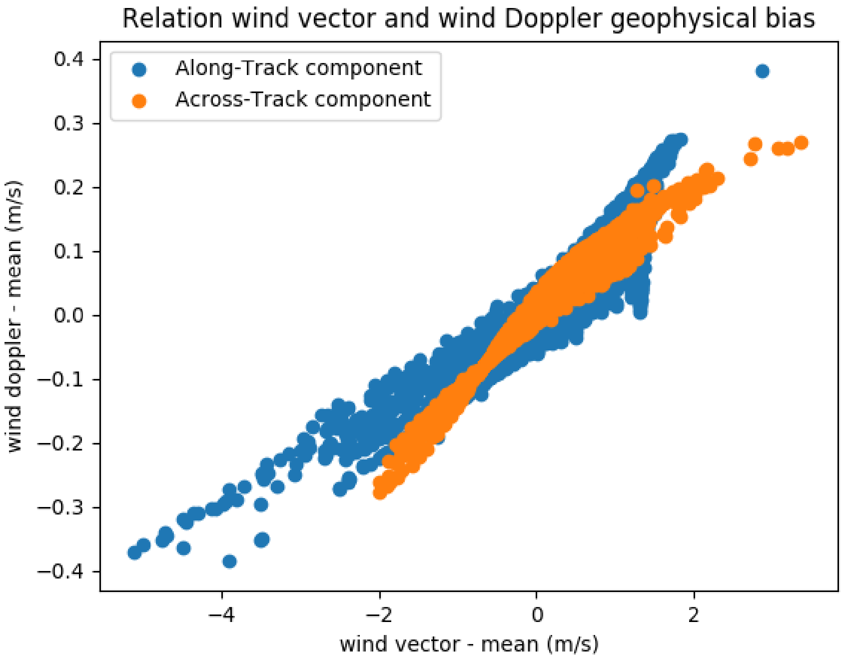

Figure 6.7: Correlation wind vector to wave geophysical bias. The correlation coefficient lies around 0.1. This implies that for the Kirchhoff Approximation the wind vector is scaled with approximately 0.1 to obtain a Doppler Centroid velocity vector. Across-track velocity was scaled with $\sin\theta_{nom}$ to project to the sea surface. Angle of incidence is 20°.

6.1.3. Total Surface Current Vector

The Total Surface Current Velocity vector is computed by means of subtraction of the wind Doppler component from the ATI Doppler velocity. The across-track TSCV is on the average 44.6% of the total ATI Doppler velocity and the along-track component of TSCV is on the average 60.0% of the total observed ATI Doppler. This illustrates that the across-track component has a higher ratio wave geophysical bias to ATI Doppler relative to the along-track component.

With respect to the ATI Doppler field in figure 6.3 the TSCV in figure 6.8 is going in a downward direction in the northern part of the image. The wind is going in upward direction, therefore it may be that the wind is properly corrected for in this part of the image.

The diagonal front seen in figure 6.2 is still causing an upward component of the TSCV. A discontinuity is also seen in the intensity and coherence (figure 3.9) on the same diagonal. The windfield however, does not display a strong gradient in vector magnitude at the discontinuity as the Doppler field does. Therefore, the NRCS may not properly correct for this strong component in along-track direction of the ATI phase.

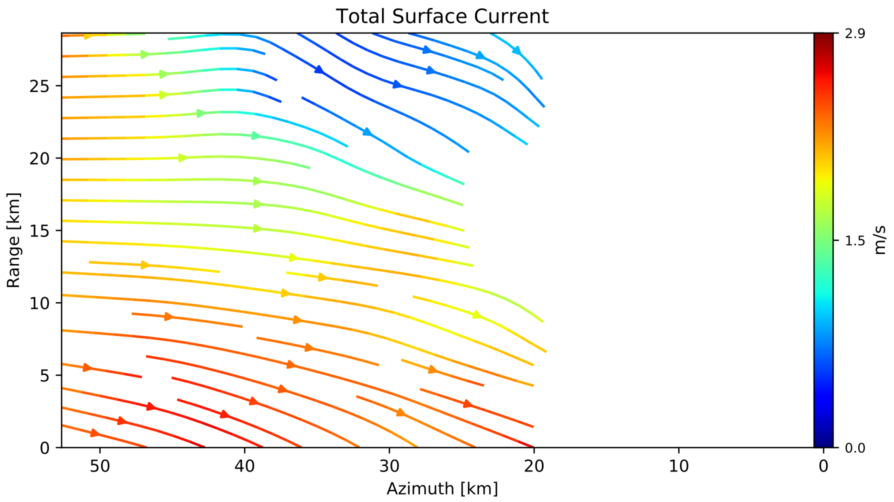

Figure 6.8: Total Surface Current Velocity Field of Tromsø. Across-track TSCV is on the average 44.6% of the total ATI Doppler velocity and the along-track component of TSCV is on the average 60.0% of the total observed ATI Doppler. Vectors are pointing at the coast (white mask). ATI Doppler along-track component may be overestimated as a result of phase calibration errors. High vector magnitudes below the diagonal suggest remaining non-current biases in the ATI Doppler.

6.2. Retrieval results of Novaya Zemlya

Results are presented and analyzed of the Novaya Zemlya acquisition of August 22th 2013 in a similar fashion as for the Tromsø acquisitions. Additionally it is attempted to retrieve a wind field from the bidirectional Doppler radial velocity to check the Doppler model validity.

Figure 6.9 shows the corrected NRCS and phase. Especially for the aft beam inland areas are slightly above zero due to errors in the DEM. The glacier at the bottom was not included to the calibration procedure. The phase has been additionally flattened and calibration was successful as the mean and mode of phase offset values are close. NRCS is corrected by adding a constant of 7 dB, as was previously done for the Tromsø acquisition. This is 1 dB more than for Tromsø . As the offset is between 6 and 7 dB and the Kirchhoff Approximation is known to overestimate wind, it is better to use a higher constant value in this case.

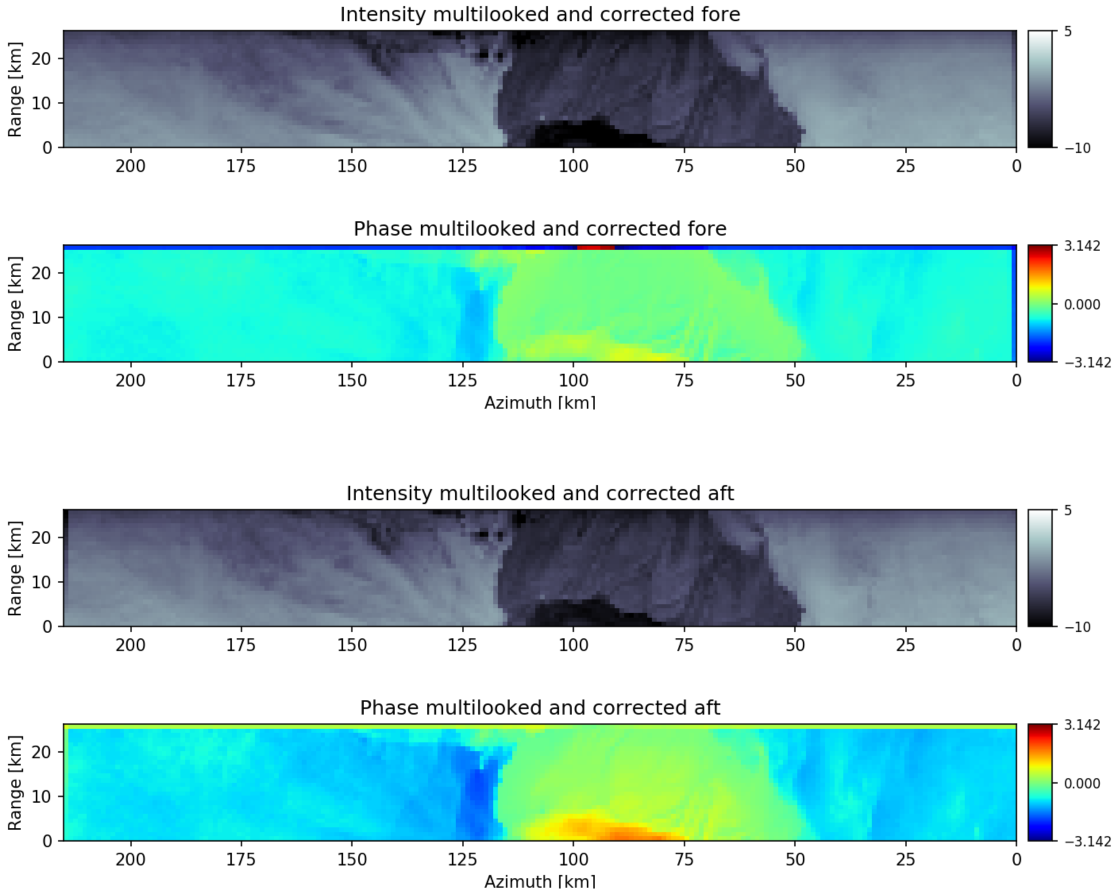

Figure 6.9: Corrected and multilooked NRCS and phase. The intensity is expressed in NRCS in dB (m^2/m^2). Resolution is 1059 m in azimuth and 973 m in range. NRCS is corrected with the addition of a constant value of 7 dB. Phase is flattened and calibrated. A glacier is located at the anomalous area in the phase image on land.

6.2.1. Doppler velocity

Again from the corrected L-2 products a Doppler field is retrieved. Figure 6.10 shows a very smooth Doppler field, that seems highly influenced by the wind as the stream lines go through the coast. The image shows some high magnitudes left of the land area, while on the right of the land there is an area with very low Doppler velocity.

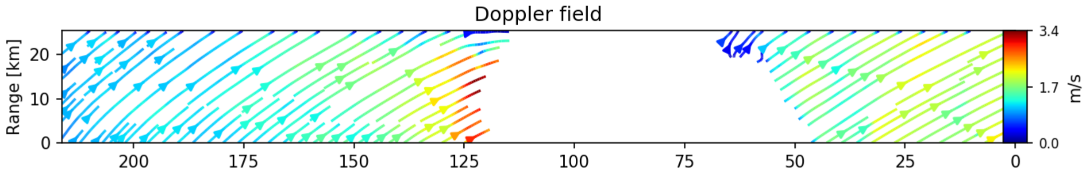

Figure 6.10: Doppler field with again arrows that go straight through the coast, suggesting a high wind bias. Some high magnitudes are seen left of the land area.

6.2.2. Wind

Interpolated ECMWF wind field shows (figure 6.11) a similar smoothness as the Doppler field, suggesting a high correlation between wind and Doppler.

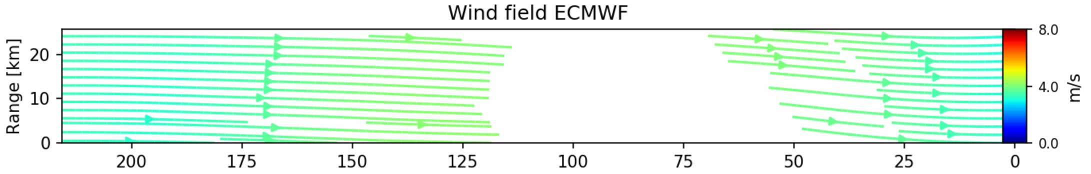

Figure 6.11: ECMWF ERA-5 wind vectors 10 m above the sea surface. Interpolated to the multilooked SAR grid as described in section 3.2. Wind field shows a similar smoothness as the Doppler field in 6.10.

For wind retrieval the Kirchhoff Approximation model is used, as the incidence angle is out of range for XMOD2 in large part of the image. Good agreement is found between wind direction of ECMWF and the retrieval results (figure 6.12). However the mean wind speed mangitude is 1.6 m/s higher for the retrieval results. It seems probable that the Kirchhoff approximation underestimates NRCS. This overestimation of wind vector magnitude will lead to an overestimation of wave geophysical bias.
The local high velocities seen left of the land in the Doppler field are not seen in the inverted wind field. What could be the cause of this geophysical signal is still undetermined.

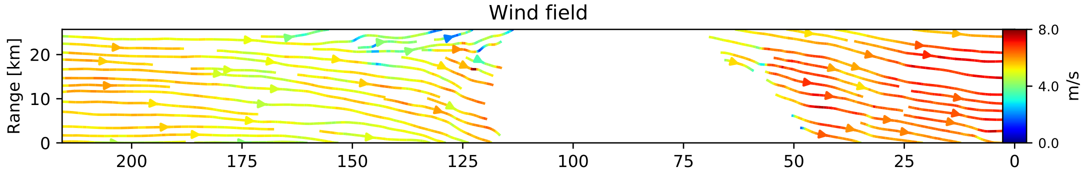

Figure 6.12: Retrieved wind field Novaya Zemlya. The wind field shows more local features than ECMWF wind field in figure 6.11 and on the average the wind direction of both data sets closely agrees. Wind speed is 1.6 m/s higher than wind speed in ECMWF wind field.

ATI Doppler data in beam Line of Sight can be used as an input for the same retrieval algorithm. Retrieving a wind vector from the Doppler data implies that we are assuming all measured Doppler is a consequence of wind, which is against the idea of this thesis. However, the algorithm is tested on the Doppler data. Regarding the linear relationship between wind vector and Doppler velocity, it does not come as a surprise that the wind field retrieved from Doppler is a scaled version of the Doppler field (figure 6.13 and 6.10).

Since the wind field is a scaling of the Doppler field, it can be confirmed that the Doppler model lies in the same range as the model values. The direction of the wind field retrieved from Doppler is 45 degrees different from ECMWF in figure 6.11. The discrepancy between directions indicates that there is a significant geophysical bias other than wind seen in the Doppler field. Figure 6.13 shows a histogram of the wind speed magnitude as retrieved from NRCS and Dopper and the ECMWF wind speed magnitudes. Large spread of Doppler wind speed magnitudes is another indication that there are geophysical biases other than wind contained in the ATI phase. ECMWF wind and winds retrieved from NRCS give a more similar distribution. However, the higher values of retrieved winds may indicate an underestimation of NRCS by the Kirchhoff Approximation model.

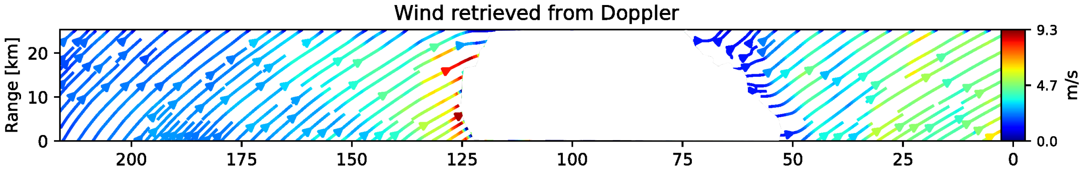

Figure 6.13: Retrieved wind field using Doppler data. Wind field is a scaled version of the Doppler field it was retrieved from seen in figure 6.10.

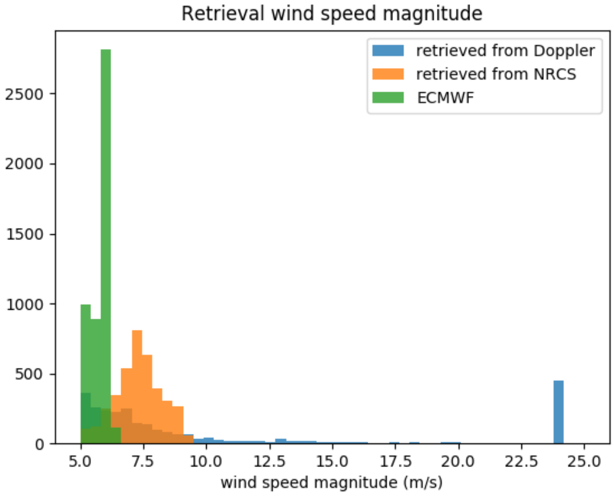

Figure 6.14: Histogram of estimated wind speed magnitude for Novaya Zemlya, using NRCS data, using Doppler data and ECMWF wind vectors. All three data sets lie in the same range, except for the anomalous peak in Doppler at 24 m/s.

6.2.3. Total Surface Current Vector

Total surface current is retrieved by subtracting the wave geophysical bias from the Doppler field (figure 6.10). From the similarity in homogeneity of the wind field and Doppler field it can be seen that the Doppler field is wind dominated. However, the wind vector seems to be overestimated in section 6.2.2.

By subtracting an overestimated wave geophysical bias, the TSCV will direct in opposite direction of the wind, which is not necessarily true. What one then observes are the errors that have arisen from errors in the radiometric calibrations and in the GMF rather than a current. Once the radiometric calibration issue is solved results will be much more accurate and by trying a selection of models one could minimize the errors from the GMF. The high velocities seen in section 6.2.1 in the Doppler field are not seen in the inverted wind field in section 6.2.2, therefore it translates to a very high TSCV.

Tidal currents are the dominant currents in the area and the Barents Sea has a weak northward component, whereas the Kara sea has a very weak current in August[11]. The currents seen in 6.15 have a velocity that is in the order of magnitude of a tidal current.

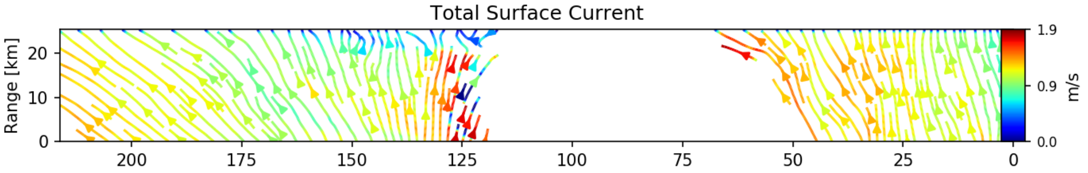

Figure 6.15: Total Surface Current Velocity field. Stream lines run along the coast, which is a characteristic of a current. Extremely high TSCV values can be a consequence of tides and/or other geophysical processes that were not included to the model, such as stokes drift.

From the pre-processed data (chapter 3) Doppler fields for Tromsø and Novaya Zemlya have been retrieved. Using the calibrated intensity products and interpolated ECMWF wind vector product at 10 m above sea level as a contraint for inversion, wind vector retrieval was performed. Tromsø shows good results for wind retrieval with XMOD2, but the Kirchhoff Approximation overestimates the wind compared with ECMWF data. A good vector field of TSCV is obtained from data of Novaya Zemlya. The next chapter concludes on the results and discusses other possibilities.

7

Conclusions

In this master's thesis work a method was proposed to retrieve the wind vector from TanDEM-X bidirectional along-track interferometric data. The work consists of the development of a wind retrieval algorithm, error analysis of the wind retrieval algorithm on simulations and a necessary radiometric calibration of TanDEM-X BiDi NRCS data. Finally, results were presented of the wind vector field and TSCV inverted from acquisitions over Tromsø and Nova Zamlaya. These results were validated with available data.

7.1. Conclusion

The purpose of the main research question was to develop a method for the retrieval of the Total Surface Current Vector from the experimental bidirectional ATI TanDEM-X data sets. The question was formulated as:

How do we separate the Total Surface Current Velocity from wave geophysical bias in TanDEM-X Bidirectional Along-Track Interferometric data?

To separate the wave geophysical bias contained in the 2D Doppler velocity from the motion of the surface as a consequence of other processes, the 2D wind vector at 10 m above the ocean's surface had to be estimated additionally to the Doppler velocity vector. This led to a problem where we had four unknowns. If observations were sufficiently diverse we could solve for the four unknowns, using the two NRCS observables for wind retrieval.

The proposed wind retrieval algorithm uses a look-up table of geophysical model functions (XMOD2 or Ifremer's electromagnetic asymptotic model, defined as 'Kirchhoff Approximation' in this report) at a range of angles of incidence to find a solution by means of minimizing a cost function of the squared differences to the observations, for the angle of incidence at the range line. The output of the wind retrieval algorithm is the wind vector in polar coordinates. The choice of a geophysical model function is based on the angle of incidence, as the XMOD2 GMF is only valid between angles of 18°and 40 °, the Kirchhoff Approximation was used in the Novaya Zemlya case (angle of incidence: 15.6°- 18.6 °).

Wind retrieval on simulated data showed to give biased results for the wind vector, as shown in the simulation results. It is seen that the diversity in NRCS between fore- and aft beam cannot be larger than the NESZ of approximately -17 dB, leading to a biased result for the wind direction and consequently greater errors in the estimate of the wind speed magnitude.

By constraining the solution for wind direction with an external data source, i.e. adding an extra obvervable to the regression scheme, this could be corrected for. Wind direction has less spatial variability than wind speed. This enabled us to use lower resolution ECMWF ERA-5 wind data and interpolate the data to the SAR grid. The external data term was given little weight (approximately $7 \cdot 10^{-6}$) in the algorithm to allow the model to be sensitive to local wind direction variability. After implementation of the contraint no more wind direction ambiguities are seen in the wind retrieval results.

The last step to computing a wave geophysical bias involves computing the Doppler velocity vector assosciated with the instantaneous motion of the surface generated by wind. This was accomplished by using a forward geophysical model, which is the same Kirchhoff Approximation model, but then for the Doppler Centroid. A simple subtraction of the wave geophysical bias from the Doppler velocity vector gave us a measure of Total Surface Current.

By applying the proposed method to acquired TanDEM-X BiDi ATI data of the area of Tromsø and then to a data take over Novaya Zemlya wind fields and TSCV were retrieved. Analysis of the results gave an indication on the quality of wind vector and TSCV retrieval. With that, the second research question can be answered:

How well do we separate between Total Surface Current Vector and the wave geophysical bias in the Doppler velocity field?

For analysis the errors have been separated into three categories: Errors arising from the GMF, errors in the data and errors from the retrieval algorithm. This categorization aims at indicating the origin of the errors and to subsequently find suitable recommendations.

Largest uncertainty was seen in the Kirchhoff approximation GMF. For Tromsø, where less steep incidence angles allow the use of both models, wind retrieval with XMOD2 estimated a 2.2 m/s lower wind speed than estimation with the Kirchhoff approximation. A similar indication of underestimation of NRCS by the Kirchhoff approximation is seen in the retrieval process of Novaya Zemlya, where mean wind speed magnitude resulting from wind retrieval is 1.6 m/s higher than that of ECMWF. The overestimation of the Kirchhoff Approximation indicates that the GMF is neither reliable for the estimation of a wave bias. For Novaya Zemlya the GMF uncertainty is the largest source of uncertainty.

Phase data errors are the largest source of error to the Total Surface Current Vector in the case of Tromsø, as a consequence of phase ambiguities on the land areas together with layover effects. In the estimation of a Doppler vector field for Tromsø it is seen that an erroneous calibration of the phase leads to large errors in ATI doppler. The estimated error bar of the along-track component is 10 m/s. This can explain the high values of along-track Doppler velocity seen for Tromsø. For Novaya Zemlya calibration of the phase shows to be more succesful, where the ATI phase has no ambiguities and the area has less topography.

NRCS data inaccuracy is another large error source, due to a persisting calibration error in the processor. The impact of this error on retrieval results is dependent on the wind speed magnitude and therefore differs per data set. The NRCS for BiDi was 6-7 dB higher than for data of the same area as observed with a nominal TanDEM-X acquisition at similar angles of incidence. To further retrieve the wind vector, a constant value between 6 and 7 dB had to be added to correct the NRCS observations, but this correction comes with a large uncertainty of 1 dB.

Propagation of a 1 dB error in NRCS to the wind vector and wave geophysical bias estimation lead to larger errors for Tromsø than for Novaya Zemlya. Errors on wind speed magnitude and wind direction are 0.7 m/s and 2°respectively for Tromsø. The wind vector estimation errors propagate to an error bar on wave geophysical bias along-track component of 2.9 m/s. Propagation of radiometric calibration errors to the wave geophysical bias along-track component for Novaya Zemlya are only 0.5 m/s. The reason for more robust retrieval in Novaya Zemlya are the higher wind speeds that lead to a higher NRCS and consequently higher SNR w.r.t. Tromsø.

Errors from te retrieval algorithm are seen where winds are weak. It was demonstrated in the simulations that weaker winds have a higher RMS. For Tromsø this has influenced the wind retrieval results.

ECMWF ERA-5 reanalysis model wind data is the reference data used in this study. Comparing these data with the wind retrieval results gives an idea of the quality. The reference wind data is from model simulations at 3 hours time intervals and a spatial resolution of 30 km. On the local scale ECMWF and wind retrieval results cannot be compared, as local wind gusts are captured by ECMWF spatially nor temporally.

Tromsø wind retrieval results compare well with the ECMWF data on the global scale. Mean wind speed and direction of the retrieved winds is 2.9 m/s and 78° with an error of 0.7 m/s induced by errors in the data, whereas ECMWF has a mean wind speed of 2.1 m/s and a direction of 89° with errors of 0.4 m/s and 33° respectively. On the local scale a patch of strong winds, possibly a wind gust, is seen in the retrieval results that also increases the global scale retrieved wind speed, therefore explaining the higher value of retrieved wind speed.

The wind retrieval result of Novaya Zemlya gives a higher estimation of the wind speed than seen in the model data. This overestimation was already linked to GMF uncertainty of the Kirchhoff Approximation.

The direction of the Doppler field are highly similar to the direction of the ECMWF model data. This indicates that there is a large wave bias contained in the Doppler field, that was corrected for in the TSCV. To check the TSCV however, no reference data of instantaneous surface currents is available. In section 2.3.1 it was pointed out that tidal surface currents have velocities up to 5 m/s in extreme cases. The TSCV results all lie well below that value and therefore all results can possibly represent a surface current.

For Tromsø however it is unlikely that the retrieved TSCV represents a surface current, because the estimation of along-track Doppler has too large an error. As a consequence the TSCV flows through the coast and this is not consistent with a current.

For Novaya Zemlya it can be concluded that the retrieved TSCV may possibly represent a surface current, since it is seen that the resulting flow pattern goes around the coast and has reasonable values. The Kirchhoff Approximation GMF gives very high uncertainty in wind retrieval as well as the computation of a wave bias. There is a small possibility that errors compensated each other and the results are correct or that the models are more correct than was concluded in the error analysis. This is possible because the ECMWF ERA-5 data, the comparison was based on, does not give real ground truth data. It has an own inaccuracy. If winds were higher than ECMWF estimated, the Kirchhoff Approximation may result to be more certain.

Since the TSCV results of Novaya Zemlya show a pattern that could possibly represent a current, it can be concluded that the method is promising. However, the large uncertainties that were pointed out in this study need to be reduced. Section 7.3 elaborates on the next steps to follow to reduce uncertainty of TSCV estimation and how to validate the results with instantaneous surface currents.

7.2. Discussion

In this section points of discussion encountered throughout the process of this thesis are brought to attention.

One point is considered with the initial assumption that wind retrieval is possible from the NRCS in BiDi geometry. The case is that wind retrieval from NRCS measurements with only a squint of 13 ° on ground may not show much diversity. In uncalibrated preliminary TanDEM-X BiDi ATI amplitudes it was seen that the difference between the beams was around 0.4 dB, as can be seen in appendix figure A.10. This seems to be sufficient for the retrieval of a wind vector, however, the amplitudes were uncalibrated and its accuracy was then unknown. With calibrated amplitudes the wind retrieval process appeared ambiguous.

Three other methods were considered for solving the ambiguity problem, but remained unused. One of these methods is to retrieve wind directions is to detect wind streaks [13]. This algorithm exploits linearly aligned structures at scales above 100 m. Difficulties will arise when no wind streaks are present, therefore the method of using ECMWF only as a constraint is more favourable.

It can be discussed that a simultanous retrieval of wind and current vector can lead to less wind direction ambiguity. A definition of the cost function used in this scheme can be found in appendix B.2 .The idea of using this retrieval scheme instead is to utlize the the Doppler velocity observable as a way to constrain the solution for wind direction. However, this will give us a look-up table with 4 dimensions $m\ x\ n\ x\ l\ x\ l$. Where m is the number of wind speed grid points, n wind direction and l TSCV. Computing wind speed at an accuracy of 0.1 m/s, wind direction at 5° and TSCV at 0.1 m/s gives us a look-up table of size 159120 along which to minimize the cost function. For reason of long computation time and because this method does not guarantee retrieval independence of an external data source, it was decided to not implement the alternative algorithm, but should be interesting to further investigate.

The last idea to solve the wind direction ambiguity problem was the use of wave directions inferred from the bidirectional cross-spectrum. The resulting 3-D histogram of this spectrum is shown in appendix figure A.2. A peak in the 2-D spectrum corresponds with a dominant wavenumber in the amplitude image. The direction of the peak can indicate a dominant wave direction. An appropriate size for resolution cells needs to be chosen to observe the shorter wind waves. Since wind waves are often shorter than the resolution it is complicated to separate them from noise. Also the effect of azimuth smearing will introduce errors in this process. It was therefore decided to not continue this study.

In the error analysis another part of discussion is that apart from the uncertainty from errors in data, GMF's and the retrieval algorithm, phase and NRCS do not always display exactly the same geophysical signals. There is a signature of geophysical origin seen in the along-track component of the Doppler field of Tromsø, which is not as well defined in the NRCS. This signature may be another reason for high values of the Doppler along-track component. In Novaya Zemlya there is also a patch of very high phase values, not recognized in the NRCS image. Comparison to atmospheric data can determine the origin of the geophysical signature.

7.3. Recommendations

This study provided an analysis of the quality of the Total Surface Current retrieval algorithm. For validation of the estimated TSCV instantaneous surface current data is needed. This data may be obtained from tidal models. The optimal tidal model is one as presented in [39], however such a model is unavailable for the region of the Barents Sea. The tides presented in [8] give an old estimation of the tides at the Barents sea. For the Tromsø area the tidal model data can be found through the Se havnivå , the Norwegian Hydrographic service.

It is recommended that for future use of the retrieval algorithm a correction is made to the experimental SAR processor. The 6-7 dB offset in NRCS is likely to have arisen from the antenna pattern correction.

The phase calibration issue in Tromsø can possibly be solved by reconstruction of the phase of layover areas. Then it is needed to use only areas that are far enough from the coast line for calibration to avoid ambiguities.

Several more data sets in BiDi ATI mode have been acquired with TanDEM-X of Tromsø and of Novaya Zemlya. For a larger sample size for validation and to better understand the surface currents in the region it is recommended to process a selection of them.

The recommended data set of Novaya Zemlya was acquired at the 11th of August 2013. It is sea ice free and does therefore provide good conditions for the retrieval of TSCV. The recommended Tromsø data set is acquired on 25th of January 2014. This data set has much coverage over sea. Three other acquisitions of Tromsø are available that have less sea coverage, it is therefore discutable if these data will give any good results, since near shore currents from this method may be influenced by phase ambiguities.

To get a better understanding of the model uncertainty it is suggested that oceanSAR, the Weighted Curvature Approximation and possibly other models are tested and evaluated with the proposed retrieval algorithm. The Weighted Curvature Approximation is known to perform better in the estimation of a Doppler Centroid and NRCS from wind than the Kirchhoff Approximation[27]. Further comparison with reference data will tell if significant improvements are made using a different GMF. For bidirectional ATI data other than presented data sets, that have larger incidence angles, it is specifically recommended to use one of the suggested GMF's for the estimation of wave bias.

After the improvements on calibration and the evaluation of different GMF's with the proposed method, the method can be valuable to use in future SAR missions that exploit intensity and Doppler or ATI phase measurements at squinted angles for the monitoring of surface currents.

A

Figures and tables

A.1. Statistics

Figure A.1: NRCS histograms for Novaya Zemlya acquisition of August 22th 2013 with calibration as currently implemented in TAXI.

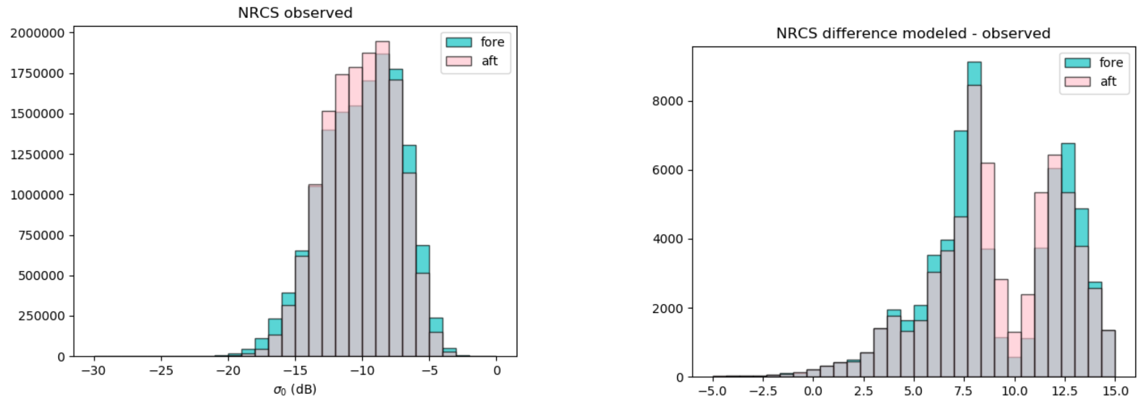

(a) NRCS distribution with current state of radiometric calibration for Novaya Zemlya.

(b) Difference with modeled values using XMOD2

Figure A.2: Bidirectional amplitude cross-spectrum. Attempt to retrieve wave direction. A signature is seen. the peak in the 2-D spectrum corresponds with a dominant wavenumber in the amplitude image. The direction of the peak can indicate a dominant wave direction. An appropriate size for resolution cells needs to be chosen to observe the shorter wind waves. Since wind waves are often shorter than the resolution it is complicated to separated from noise. Also the effect of azimuth smearing will introduce errors in this process. It was therefore decided to not continue this study.

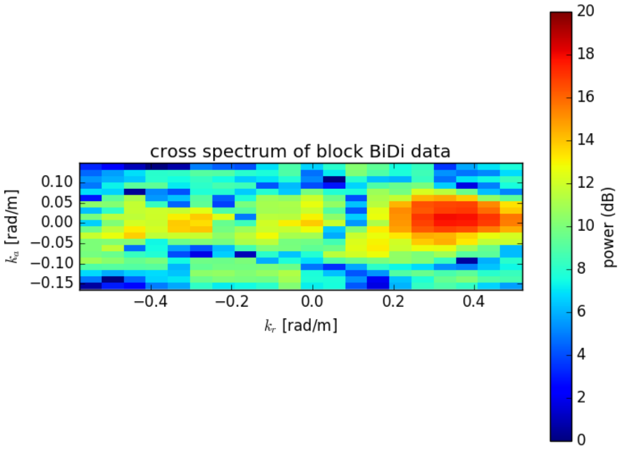

A.2. Maps

Figure A.3: Ocean surface currents from reanalysis model. Currents are at 0.97 m depth interpolated from CMEMS global physics reanalysis model monthly product. These current products cannot be compared with the inverted TSCV, due to the presence of tides in single ATI SAR images.

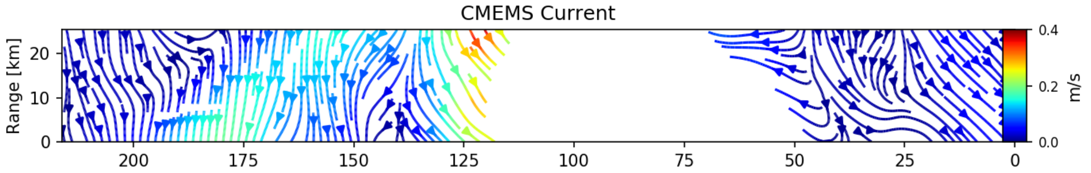

(a) Novaya Zemlya

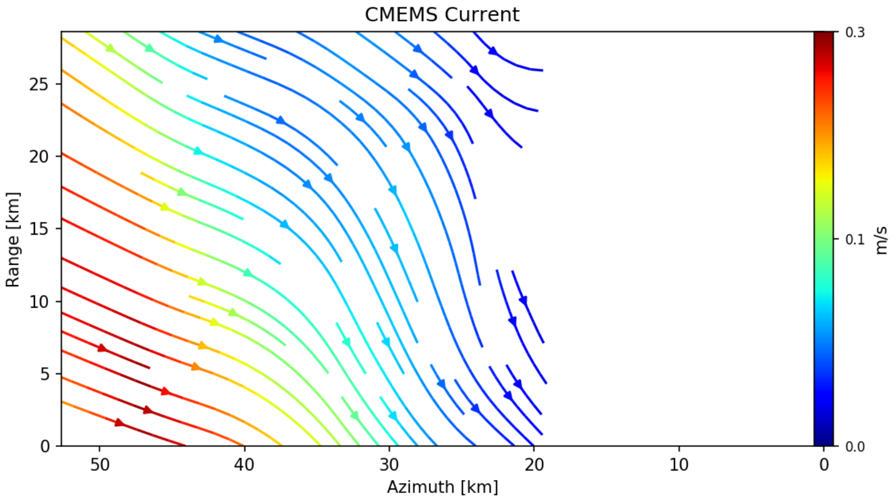

(b) Tromsø

Figure A.4: A map of the differences in NRCS (dB) between values modeled with ECMWF wind vectors and XMOD2 of the Tromso acquisition. Half the image is masked, as ECMWF wind speed is lower than 2 m/s, which is below model range.

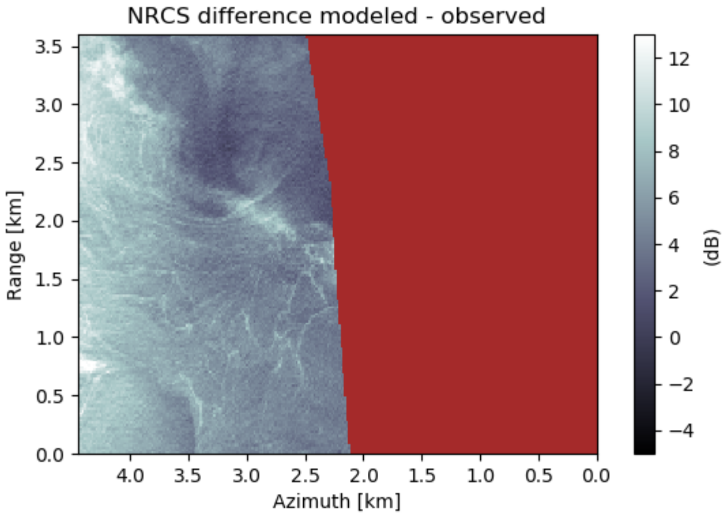

Figure A.5: A map of the differences in NRCS (dB) between values modeled with ECMWF wind vectors and XMOD2 of the Novaya Zemlya acquisition strip. Same data as the distribution in A.1a.

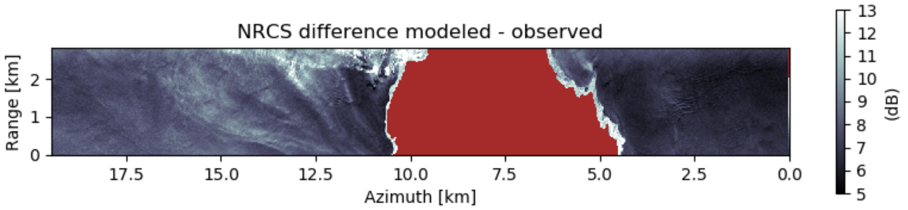

Figure A.6: Doppler across-track and along-track velocity of Novaya Zemlya.

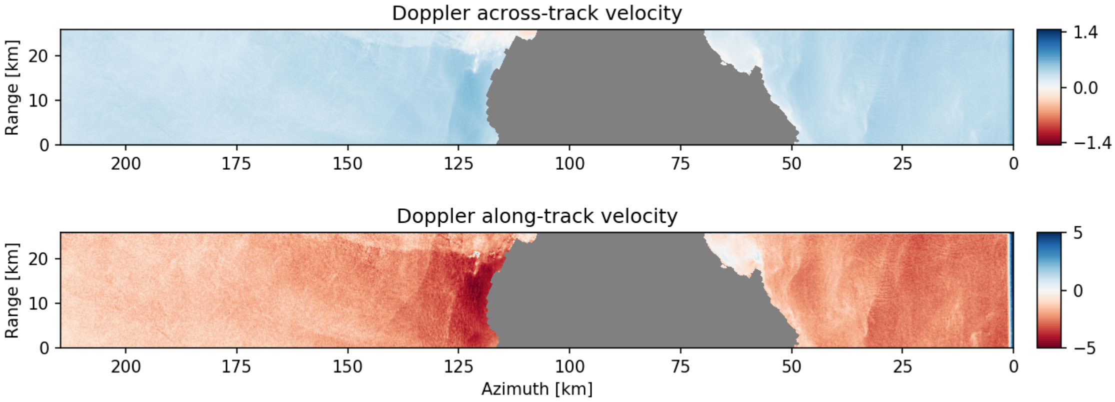

Figure A.7: The wind vector displayed in images. It can be seen that the wind direction estimation has improved much with smoothing, noise from estimation ambiguities is eliminated.

(a) Retrieved speed magnitude, smoothed with a Hamming window of 3 sample spacings long.

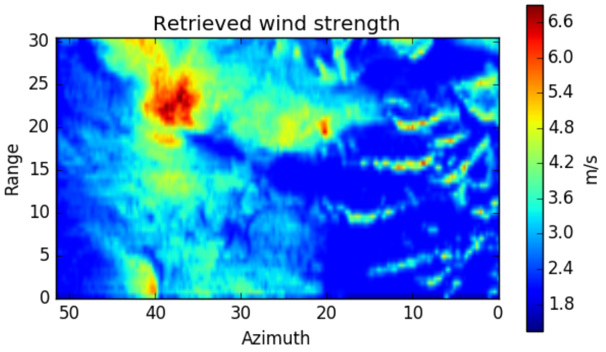

(b) Retrieved wind direction, smoothed with a Hamming window of 7 sample spacings long.

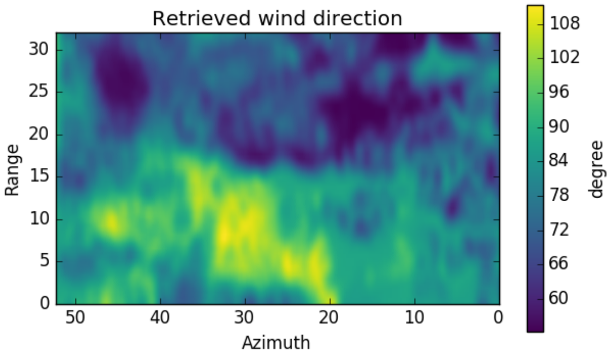

Figure A.8: Effect of constraint on wind direction estimation

(a) Retrieved wind direction without using a constraint. The wind direction alternates between positive and negative. This is due to ambiguous retrieval as was expected regarding the simulations results.

(b) Retrieved wind direction using the interpolated ECMWF wind direction as a constraint.

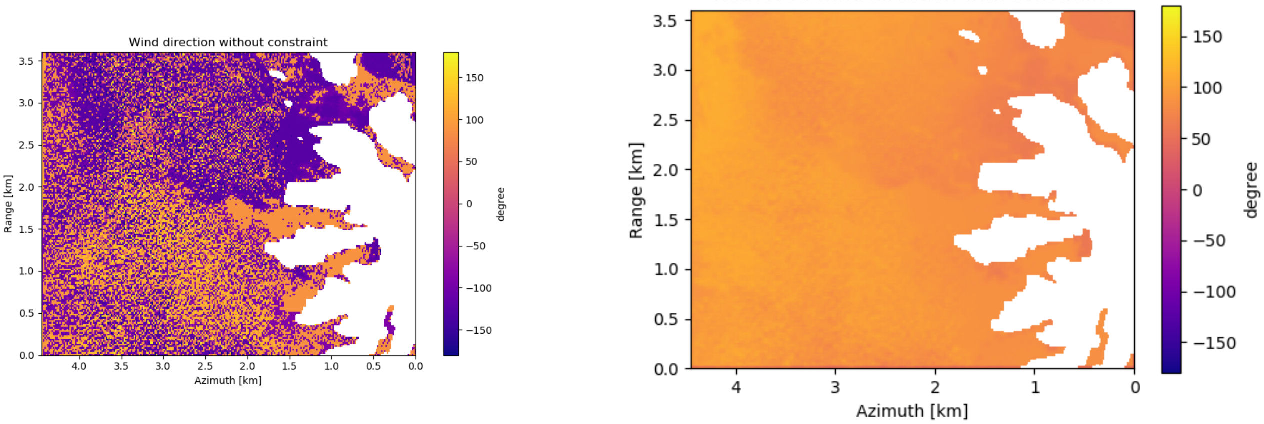

Figure A.9: Along-track and across-track component of the Doppler velocity vector over Tromso. The negative along-track component shows a strong coast-ward movement as inferred from the NRCS data. This is in agreement with the ATI Doppler field seen in figure 6.3.

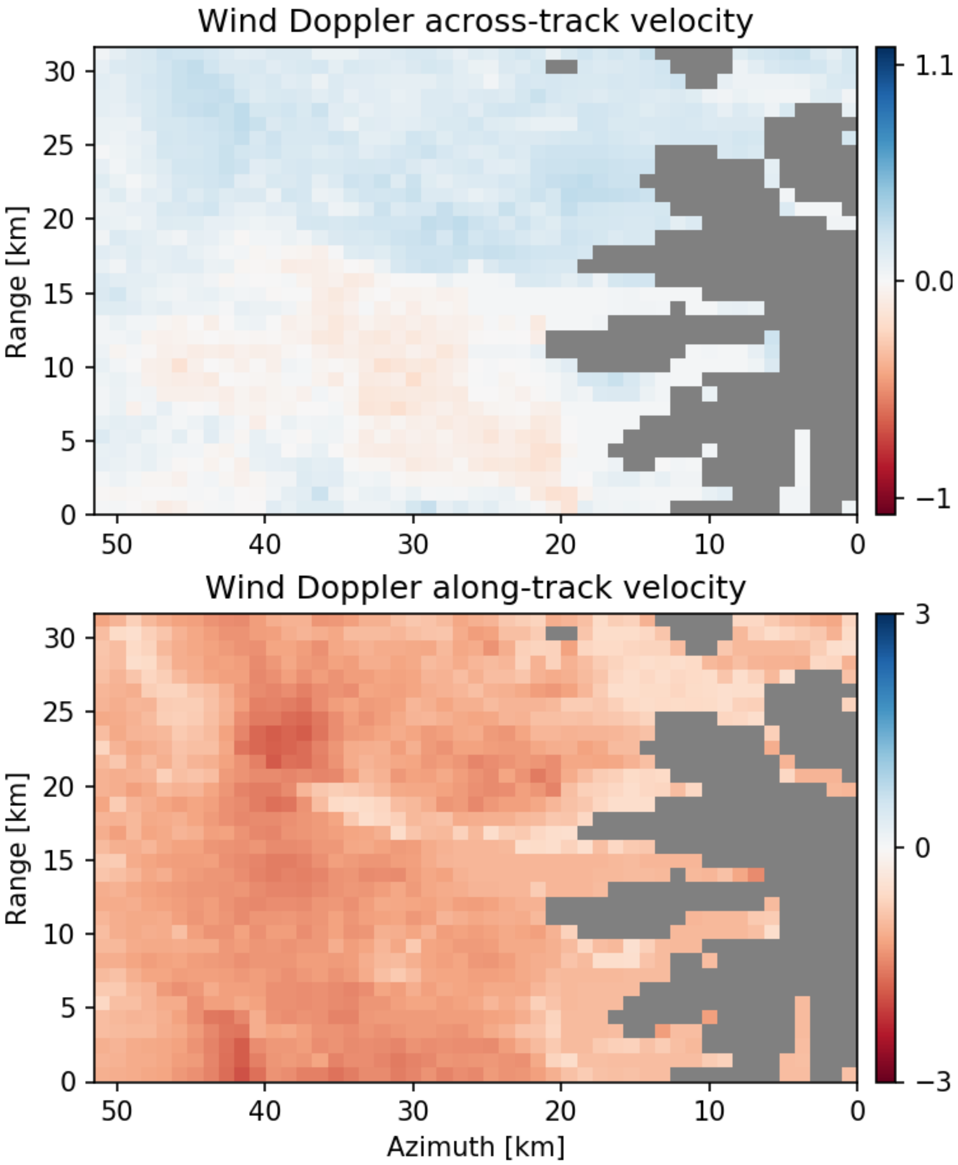

Figure A.10: Moving average filtered series of the difference in amplitude between fore- and aft beam. A 2D moving average filter was applied to the amplitude images after a conversion to dB, then the difference between fore- and aft image was taken to produce these series. The land structure right of the middle of the image and other artifacts at sea become clearer, but at filter width 9 the spectrum of amplitudes becomes too small. It can be seen in the image with filter width 5, that the ocean surface has approximately a 0.4 dB higher amplitude difference than the land, which is approximately 0.

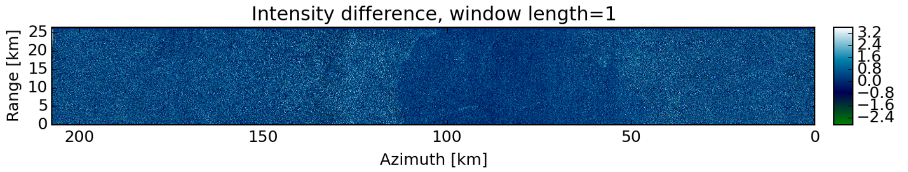

(a)

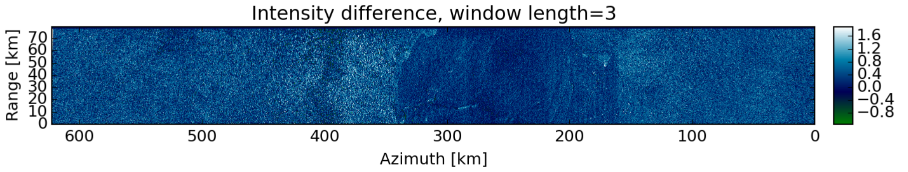

(b)

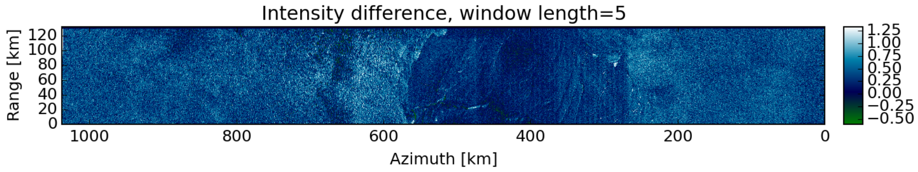

(c)

Figure A.11: Moving average filtered series of the difference in amplitude between fore- and aft beam.

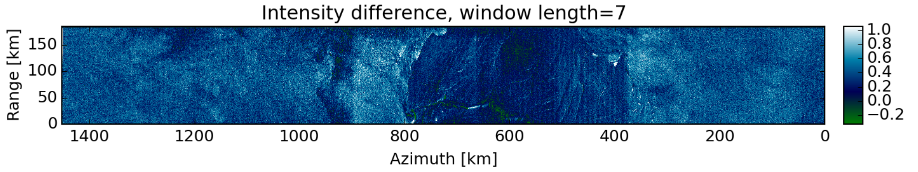

(a)

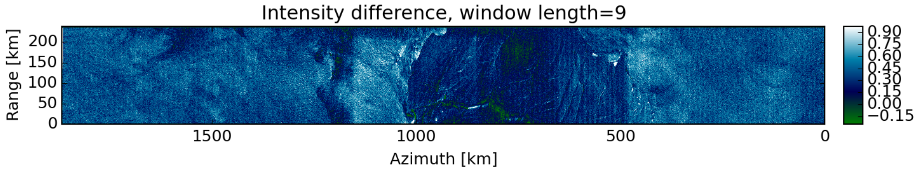

(b)

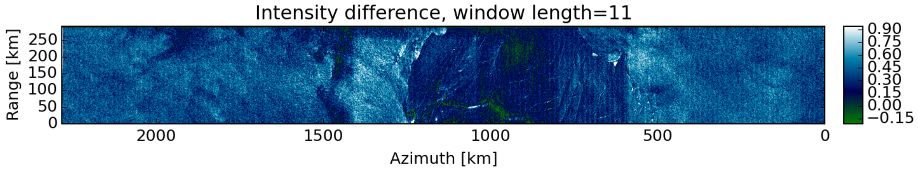

(c)

Figure A.12: L-2 products of an acquisition over the Nara strait Greenland taken March 27th 2014. This data set was expected to have large flat areas of ice for calibration purposes, but as can be seen in the amplitude there is plenty of layover and topography on the ice. Perhaps (current) movements of the water/ice could be observed in the strait.

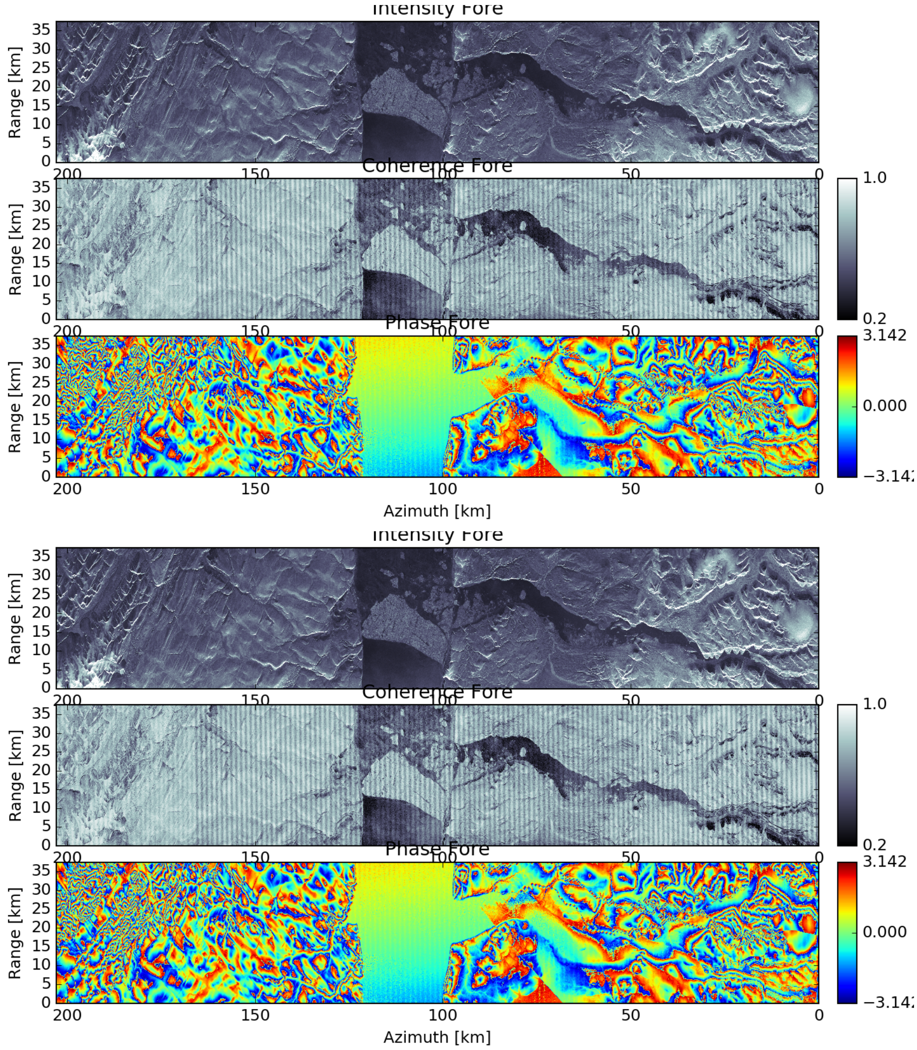

Figure A.13: L-2 products of an acquisition over Novaya Zemlya taken February 14th 2014. This is how the area looks like if it is not summer, plenty of sea ice. Not many waves are seen at sea, therefore the image is not useful for our algorithm. However if one could classify the ice, phase offsets due to radar noise can be studied over the flat non moving ice areas to improve phase calibration.

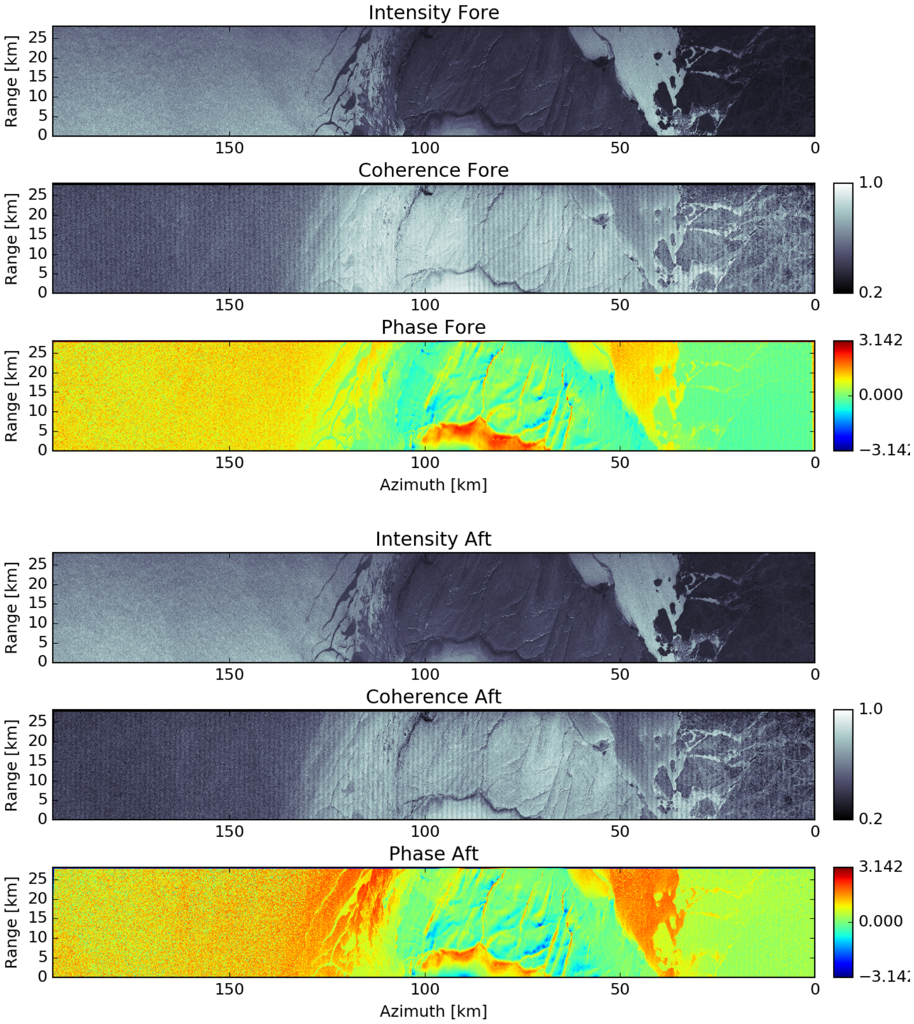

A.3. Plots

Figure A.14: CMOD5 C-band empirical GMF for NRCS and the similar XMOD2 tuned on X-band radar data. The models are evaluated for an angle of incidence of 17°. At this angle of incidence CMOD5 is valid, whereas XMOD2 was tuned on data with an angle of incidence of 18°up.

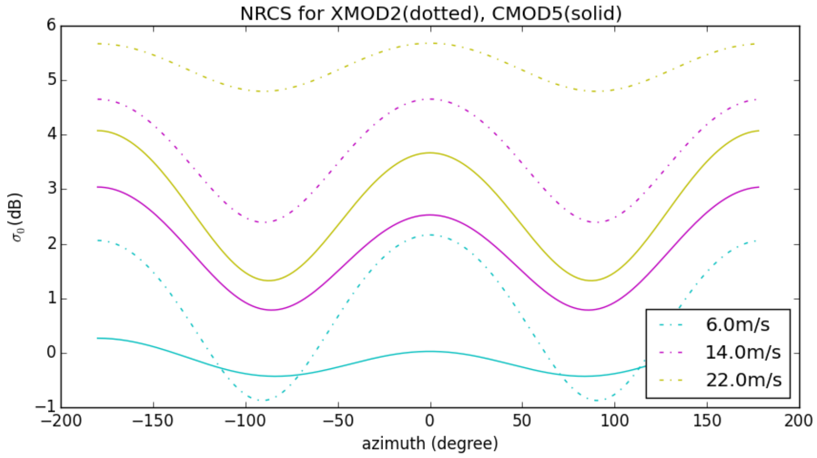

Figure A.15: Kirchhoff Approximation semi-analytical electromagnetic model for Doppler Centroid for X-band as a function of azimuth and the empirical GMF CDOP for C-band radar.

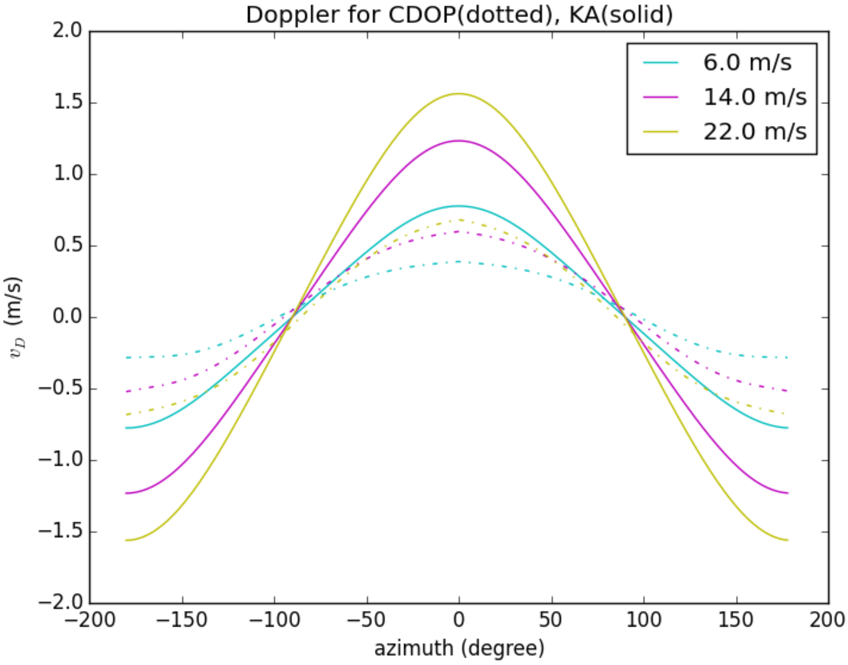

Figure A.16: Kirchhoff Approximation semi-analytical electromagnetic model for Doppler Centroid for X-band as a function of wind direction and the empirical GMF CDOP for C-band radar. It looks as if the Kirchhoff Approximation is simply a scaling of CDOP.

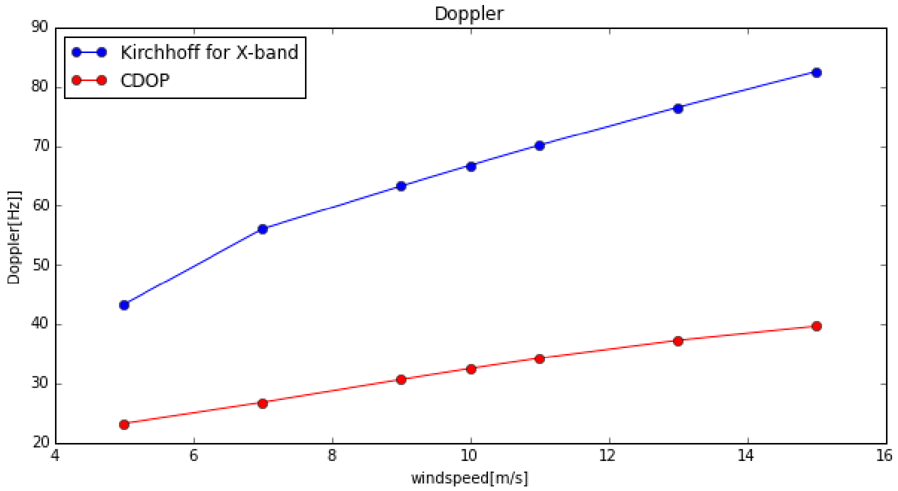

Figure A.17: This figure shows the estimation for the wind direction parameter if no constraint is used. It clearly illustrates ambiguous behaviour of the solution. Simulation scheme is similar to the scheme presented in chapter 5. The full possible range of wind directions is used as input to the simulation.

The colourful dots show wind direction estimations. The blue line represents the real wind direction and the green line is the mean. The mean looks as an error of wind direction estimation, which is close to zero in up-wind ((-)180°) and down-wind(0°) and highest for cross-wind.

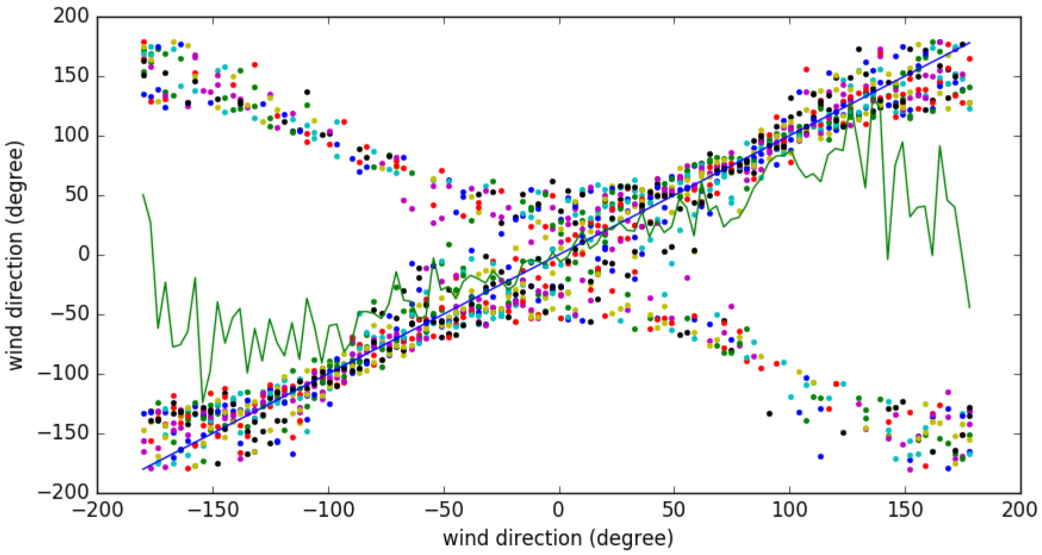

A.4. Tables

Table A.1: Description of input parameters for the wind retrival algorithm. The inputs illustrate that the function is based on the observations, geometry and the chosen geophysical model function. Output is the wind vector in polar coordinates.
One can use the same retrieval algorithm (with a slightly modified function) to retrieve the wind vector from ATI Doppler. The input for observations should then be `vr`, which is a matrix with dimensions similar to `sigma0`, containing the ATI doppler observations in Line of Sight. Wind retrieval from ATI doppler observations will use the Kirchhoff approximation as a model for Doppler Centroid in this algorithm.

input	description
`sigma0`	m x n x 2 matrix of NRCS observations. m is the number of azimuth samples, n range samples and the last dimension is fore- and aft beam in that order;
`geom`	dictionary containing an m x n matrix of incidence angles `'theta_i_fore'`, squint angle scalars `'squint_fore'`, `'squint_aft'` and `'d_az'` azimuth resolution;
`du10`	wind speed magnitude accuracy (m/s);
`dazi`	wind direction accuracy (degree);
`dtheta`	incidence angle accuracy (degree);
`externalData`	(optional) m x n matrix of wind direction data from an external source (degree), relative to the nominal radar look;
`forceXMOD2`	set to `True` to use XMOD2 model for wind retrieval;
`forceNKIR`	set to `True` to use Kirchhoff approximation model for wind retrieval;
`res`	smoothing resolution (m).

B

Formula's

B.1. Derivation of squint angle on ground with Earth's curvature

In this appendix section the geometrical derivation of beam squint on ground is presented. To compute the squint angle on ground one needs to know the orbit height H, radius of the Earth R_E, nominal radar look angle $\theta_{look\perp}$, radar squint angles ψ_{fore} and ψ_{aft}.
The sine rule gives the nominal (⊥) slant range as follows:

$$\frac{SR_\perp}{sin(\delta\theta_\perp)} = \frac{R_E}{sin(\theta_{look\perp})} \tag{B.1}$$

$$SR_\perp = \frac{R_E \cdot sin(\delta\theta_\perp)}{sin(\theta_{look\perp})} \tag{B.2}$$

where $\delta\theta = \theta_{inc} - \theta_{look}$ and θ_{inc} follows from the look angle, again using the sine rule.

$$\theta_{inc} = arcsin\left(\frac{sin(\theta_{look}) \cdot (R_E + H)}{R_E}\right) \tag{B.3}$$

The distance D between nominal radar look and beam on ground with squint angle ψ_s from the nominal look:

$$D_s = SR_\perp \cdot tan(\psi_s) \tag{B.4}$$

The ground range for a squinted beam is derived using the sine rule.

$$\frac{GR_s}{sin(\delta\theta_s)} = \frac{R_E}{sin\left(\frac{180-\delta\theta_s}{2}\right)} \tag{B.5}$$

$sin\frac{180-\delta\theta_s}{2}$ is very close to 1, that leaves us with:

$$GR_s = R_E sin(\delta\theta_s) \tag{B.6}$$

and for each beam $\theta_{look,s}$ follows from:

$$\theta_{look,s} = arccos\frac{cos(\theta_{look\perp})}{cos(\psi_s)} \tag{B.7}$$

Evaluating equation B.3 with $\theta_{look,s}$ gives the incidence angle for the squinted beam and then $\delta\theta_s$ follows from the difference between incidence angle and look angle.
With known distance and ground range of the beam, squint angle on ground α_s then becomes the following:

$$\alpha_s = arcsin\left(\frac{D_s}{GR}\right) \tag{B.8}$$

Equation B.4 to B.8 are repeated to compute the ground squint angle for each beam.

B.2. Cost function for simultaneous regression of wind vector and TSCV

This is a methid alternative to the cost function shown in 4.1:

$$J_i(U,\phi,TSCV_{fore},TSCV_{aft}) = \frac{(\sigma_{0,fore,i}-\bar{X}(U,\phi-\Delta\phi))^2}{Var(\sigma_{0,fore})} +$$

$$\frac{(\sigma_{0,aft,i}-\bar{X}(U,\phi+\Delta\phi))^2}{Var(\sigma_{0,aft})} + \frac{(v_{fore,i}-TSCV_{fore}-\bar{V}(U,\phi-\Delta\phi))^2}{Var(v_{fore})} +$$

$$\frac{(v_{aft,i}-TSCV_{aft}-\bar{V}(U,\phi+\Delta\phi))^2}{Var(v_{aft})}$$

where U_{10} is the wind speed parameter (m/s), ϕ the wind direction parameter relative to across-track look (degree), $TSCV_{fore}$ the Total surface current velocity component in the fore beam as a range of values between -1. and 1. (m/s), $TSCV_{aft}$ the Total surface current velocity component in the aft beam as a range of values between -1. and 1. (m/s), σ_0 the normalized radar cross section observations (-), $\bar{X}$ the XMOD2 look-up table (-), $\Delta\phi$ the squint angle of the beams on ground and $\bar{V}$ Doppler Velocity look-up table (m/s).

The look-up tables are 4 dimensional and will be very large. It is suggested to use sparse matrices along the 3rd and 4th dimension.

C

Code

Code is available on `https://github.com/NinaCaldarella/TDX_BiDi_ATI`.

Bibliography

[1] W. Alpers and C. Bruening. On the relative importance of motion-related contributions to the sar imaging mechanism of ocean surface waves. *IEEE Transactions on Geoscience and Remote Sensing*, GE-24(6), November 1986.

[2] R. Bamler and P. Hartl. Synthetic aperture radar interferometry. *Inverse Problems*, 14, 01 1998.

[3] B. Chapron. Direct measurements of ocean surface velocity from space: Interpretation and validation. *Journal of Geophysical Research*, 110, 2005.

[4] K. Dohan. Monitoring ocean currents with satellite sensors. *Oceanography*, 23(4), December 2010.

[5] T. Elfouhaily and C. Guerin. A critical survey of approximate scattering wave theories from random rough surfaces. *Waves in random media*, 14, 2004.

[6] T. Elfouhaily, B. Chapron, and K. Katsaros. A unified directional spectrum for long and short wind-driven waves. *Journal of Geophysical Research*, 102(C7):15,781–15,796, July 1997.

[7] L. Fu, D. Alsdorf, E. Rodriguez, R. Morrow, N. Mognard, J. Lambin, P. Vaze, and T. Lafon. The swot (surface water and ocean topography) mission: Spaceborne radar interferometry for oceanographic and hydrological applications. In *Proceedings of OceanObs'09*, 2009.

[8] B. Gjevik and T.Straume E.Nøst. Model simulations of the tides in the barents sea. *Journal of Geophysical Research*, 99(C2):3337–3350, February 1994.

[9] R.M. Goldstein. Interferometric radar measurement of ocean surface currents. *Nature*, 328:707–709, August 1987.

[10] R.F. Hanssen. *Radar Interferometry: Data Interpretation and Error Analysis.* PhD thesis, TU Delft, 2001.

[11] I. Harms and M. Karcher. Modeling the seasonal variability od hydrography and ciculation in the kara sea. *Journal of Geophysical Research*, 104(C6), June 1999.

[12] H. Hersbach. Cmod5 an improved geophysical model function for ers c-band scatterometry. Technical report, European Centre for Medium-Range Weather Forecasts, 2003.

[13] J. Horstmann and W. Koch. Measurement of ocean surface winds usingsynthetic aperture radars. *IEEE Journal of Oceanic Engineering*, 30(3), July 2005.

[14] *Radiometric Calibration of TerraSAR-X Data.* Infoterra, 88039 Friedrichshafen, Germany, 2008.

[15] J.E.Stiansen, O. Korneev, O.V. Titov, P. Arneberg, A. Filin, J.R. Hansen, A.S. Høines, and S. Marasev. Report on the barents sea ecosystem. Technical report, Joint Norwegian-Russian Environmental Status 2008, 2009.

[16] B. Kinsman. *Wind waves: Their Generation and Propagation on the Ocean Surface.* Unabridged Dover, New York, 1984.

[17] P. Klein. The oceanic vertical pump induced by mesoscale and submesoscale turbulence. *Marine Science*, 2009.

[18] W. Krauss. The north atlantic current. *Journal of Geophysical Research*, 91:5061–5074, April 1986.

[19] G. Krieger, A. Moreira, H. Fiedler, I. Hajnsek, M. Werner, M. Younis, and M. Zink. Tandem-x: A satellite formation for high-resolution sar interferometry. *IEEE Transactions on Geoscience and Remote Sensing*, 45(11):3317–3341, Nov 2007. ISSN 0196-2892. doi: 10.1109/TGRS.2007.900693.

[20] V. Kudryavtsev. A semiempirical model of the normalized radar cross-section of the sea surface. *Journal of Geophysical Research*, 108(C3, 8054), January 2003.

[21] S. Lehner. Validation of coastal wind and wave fields by high resolution satellite data. In *12th International Workshop on Wave Hindcasting and Forecasting*, Kohala Coast, Hawai'i, 2011.

[22] P. Lopez-Dekker, M. Rodriguez-Cassola, P. Prats, F. De Zan, T. Kraus, S. Sauer, and J. Mittermayer. Experimental bidirectional sar ati acquisitions of the ocean surface with tandem-x. In *EUSAR 2014; 10th European Conference on Synthetic Aperture Radar*, pages 1–4, June 2014.

[23] M. Lévy. Impact of sub-mesoscale physics on production and subduction of phytoplankton in an oligotrophic regime. *Journal of Marine Research*, 59(4), July 2001. possible application.

[24] J. Mittermayer, S. Wollstadt, P. Prats-Iraola, P. Lopez-Dekker, G. Krieger, and A. Moreira. Bidirectional sar imaging mode. *IEEE Transactions on Geoscience and Remote Sensing*, 51(1):601–614, Jan 2013. ISSN 0196-2892. doi: 10.1109/TGRS.2012.2202669.

[25] A. Mouche. Predicted doppler shifts induced by ocean surface wave displacements using asymptotic electromagnetic wave scattering theories. *Waves in Random and Complex Media*, 18(1):185–196, February 2008.

[26] F. Nirichio and S. Venafra. Xmod2 - an improved geophysical model function to retrieve sea surface wind fields from cosmo-skymed x-band data. *European Journal of Remote Sensing*, 46, 2013.

[27] F. Nouguier. Analytical techniques for the doppler signature of sea surfaces in the microwave regime—i: Linear surfaces. *IEEE Transactions on Geoscience and Remote Sensing*, 49(12), December 2011.

[28] O.M. Phillips. Spectral and statistical properties of the equilibrium range in wind-generated gravity waves. *Journal of Fluid Mechanics*, 156:505–531, 1985.

[29] E. Rodriguez. Two-dimensional surface currents using vector along-track interferometry. In Proc. PIERS'95, editor, -, Seattle, 1995.

[30] R. Romeiser and W. Alpers. An improved composite surface model for the radar backscattering cross section of the ocean surface: 1. theory of the model and optimization/validation by scatterometer data. *Journal of Geophysical Research: Oceans*, 102(C11):25237–25250, 1997. doi: 10.1029/97JC00190.

[31] R. Romeiser, H. Breit, M. Eineder, and H. Runge. Demonstration of current measurements from space by along-track sar interferometry with srtm data. In *IEEE International Geoscience and Remote Sensing Symposium*, volume 1, pages 158–160 vol.1, 2002. doi: 10.1109/IGARSS.2002.1024973.

[32] A. J. Camps S. J. Frasier. Dual-beam interferometry for ocean surface current vector mapping. *IEEE Transactions on Geoscience and Remote Sensing*, 39(2):401–414, Feb 2001. ISSN 0196-2892. doi: 10.1109/36.905248.

[33] R. Sætre and R. Ljøen. The norwegian coastal current. Technical report, Institute of Marine Research Norway, 1972.

[34] F. Saïd, H. Johnsen, B. Chapron, and G. Engen. An ocean wind doppler model based on the generalized curvature ocean surface scattering model. *IEEE Transactions on Geoscience and Remote Sensing*, 53(12): 6632–6638, Dec 2015. ISSN 0196-2892. doi: 10.1109/TGRS.2015.2445057.

[35] R. Stewart. Introduction to physical oceanography. -, 1997-2000.

[36] W. Tang, W. Liu, and B. Stiles. Evaluation of high-resolution ocean surface vector winds measured by quikscat scatterometer in coastal regions. *IEEE Transactions on Geoscience and Remote Sensing*, 42(8): 1762–1769, Aug 2004. ISSN 0196-2892. doi: 10.1109/TGRS.2004.831685.

[37] J.V. Toporkov, D. Perkovic, G. Farquharson, M. Sletten, and S. Frasier. Sea surface velocity vector retrieval using dual-beam interferometry: First demonstration. *IEEE Transactions on Geoscience and Remote Sensing*, 43(11), November 2005.

[38] S. Wollstadt, P. López-Dekker, F. De Zan, and M. Younis. Design principles and considerations for spaceborne ati sar-based observations of ocean surface velocity vectors. *IEEE Transactions on Geoscience and Remote Sensing*, 55(8):4500–4519, Aug 2017. ISSN 0196-2892. doi: 10.1109/TGRS.2017.2692880.

[39] Firmijn Zijl, Martin Verlaan, and Herman Gerritsen. Improved water-level forecasting for the northwest european shelf and north sea through direct modelling of tide, surge and non-linear interaction. *Ocean Dynamics*, 63(7):823–847, Jul 2013. ISSN 1616-7228. doi: 10.1007/s10236-013-0624-2. URL `https://doi.org/10.1007/s10236-013-0624-2`.